U.PORTO

FEUP FACULDADE DE ENGENHARIA
UNIVERSIDADE DO PORTO

Modelling of Damage and Failure of Thermoplastic Matrix Composite Laminates

Guilherme Leal Martinho da Rocha Coelho

FEUP Supervisor:
Prof. José Joaquim da Mota Machado, PhD

FEUP Co-Supervisor:
Prof. Marco Paulo Lages Parente, PhD

ISAE-SUPAERO Supervisor:
Prof. Frédéric Lachaud, PhD

Dissertation developed in the context of a research internship at the Department of Mechanics, Structures and Materials of ISAE-SUPAERO and submitted to Universidade do Porto - Faculdade de Engenharia in partial fulfillment of the requirements for the degree of Master in Mechanical Engineering

Porto, October 6, 2023

Abstract

The use of fiber reinforced polymer composites in the aeronautical industry has seen a significant increase in the past years. Lighter and more efficient structures made possible by the use of these materials have become pivotal in its journey to reducing fuel consumption and achieving sustainability goals when faced with increasingly demanding regulation regarding emissions and waste. Despite the structural innovations that composites bring forward, there are important concerns regarding their capability to sustain impact without significant property degradation, especially in the case of low-velocity impact which leaves barely visible damage that might pass unnoticed under inspection. Furthermore, the life-cycle of the standard thermoset based composites is unsustainable, posing environmental concerns due to their non-recyclability.

Hence, the industry is slowing shifting towards the use of thermoplastic matrix composites, which are a promising alternative that is on track to have higher production rates, better behaviour under low velocity impact and increased sustainability due to their recyclable and repairable nature. As part of this trend, Airbus Atlantic is developing a cockpit project using a novel thermoplastic matrix composite. Therefore, under the effort of certification and given that compliance to the special regulatory conditions for composites can be demonstrated not only by experimental testing but by numerical simulations as well, this work aims at developing a numerical model for the intraply behaviour of thermoplastic composites. To this effect, diffuse damage, pseudo-plasticity, fiber rotation, as well as failure criteria and post-failure damage evolution are implemented under the frame of continuum damage mechanics. Its application in a computational framework was done in conjunction with the finite element solver Abaqus via the user material and vectorized user material subroutines and validation was completed in a representative volume element, as well as standard test specimens, creating the base for its implementation in other stereotypical load scenarios and larger scale structures.

The user material subroutine was successfully validated, presenting close resemblance to experimental results while the vectorize user material subroutine was only partially validated, requiring future adjustments to the plasticity module. Some key areas that would benefit from future efforts at improving the model and its corresponding subroutines are the integration of the interlaminar behaviour by the use of cohesive elements and the incorporation of strain rate dependent formulation, in order to properly simulate dynamic behaviour, which is the next stage of the project.

Keywords: ABAQUS, aeronautic, composite, damage, subroutine, thermoplastic

Resumo

O uso de compósitos poliméricos reforçados com fibras na indústria aeronáutica tem registado um aumento significativo nos últimos anos. A utilização destes materiais tornou possível a construção de estruturas mais leves e eficientes, fundamentais para a redução do consumo de combustível e alcançar objetivos de sustentabilidade, face a medidas regulatórias cada vez mais exigentes relativamente à questão de emissões e poluentes. Apesar das inovações estruturais possibilitadas pelos materiais compósitos, existem preocupações quanto à sua capacidade de suportar impacto sem sofrerem degradação significativa das suas propriedades, especialmente no caso de impactos de baixa velocidade, que deixam danos de difícil observação que podem passar despercebidos durante a inspeção. Além disso, o ciclo de vida dos compósitos à base de resinas termoendurecidas é insustentável, suscitando preocupações ambientais devido não poderem ser reciclados.

Por conseguinte, a indústria está a passar por uma lenta conversão para a utilização de compósitos de matriz termoplástica, uma alternativa promissora que promete ter taxas de produção mais elevadas, melhor comportamento sob impacto de baixa velocidade e maior sustentabilidade devido à sua natureza reciclável e reparável. Parte desta tendência, a Airbus Atlantic está a desenvolver um projeto de *cockpit* que utiliza um novo compósito de matriz termoplástica. Assim, no âmbito do processo de certificação e dado que a conformidade com as condições regulamentares especiais de compósitos pode ser demonstrada não só através de ensaios experimentais como por simulações numéricas, este trabalho tem como objetivo desenvolver um modelo numérico para o comportamento de compósitos termoplásticos. Sendo assim, dano difuso, pseudo-plasticidade, rotação das fibras, bem como critérios de falha e evolução do dano pós-falha são implementados. A sua aplicação num contexto computacional foi feita através do *software* de elementos finitos Abaqus mediante sub-rotinas UMAT e VUMAT, e a sua validação foi realizada num elemento de volume representativo, bem como em provetes de ensaio padrão, fundamentando a sua implementação noutros cenários de carga típicos.

A sub-rotina UMAT foi validada com sucesso, tendo grande semelhança com os resultados experimentais, enquanto que sub-rotina VUMAT foi apenas parcialmente validada, sendo que necessita de ajustes ao módulo de plasticidade. Algumas áreas chave em que esforços futuros se devem concentrar, de modo a melhorar o modelo, passam pela integração do comportamento interlaminar, através da utilização de elementos coesivos, e a adaptação da formulação de modo a incluir os efeitos da taxa de deformação, para simular eficazmente o comportamento dinâmico, que se enquadra na próxima fase do projeto.

Palavras-chave: Abaqus, aeronáutica, compósitos, dano, sub-rotina, termoplástico

Acknowledgments

First and foremost, I would like to express my sincere gratitude to Prof. Dr. José Machado, for the unwavering support and confidence he had in me through all the stages of this project, and for the invaluable advice he has provided, not only in the context of this dissertation, but throughout my academic journey.

I would also like to extend special thanks to Prof. Dr. Frédéric Lachaud who, through his guidance and expertise in the field of composites, was of immeasurable help to the development of this dissertation, and for creating a truly positive and collaborative work environment during the internship at ISAE-SUPAERO.

Furthermore, I want to thank Prof. Dr. Marco Parente for helping me validate key aspects of the work and providing key technical insights that improved its quality, aided in its completion and that might lead into future work plans.

I also want to extend special appreciation to my internship and fellow master thesis colleague Rui, who accompanied and supported me throughout this dissertation and the whole mobility period, which made the whole process much more enjoyable.

To my dearest close circle of friends, I express heartfelt appreciation for accompanying me during this work and for all these years, through the highs, the lows and everything in between, I am truly grateful for you to have been a part of my journey and to have been a part of yours.

Finally, I would like to express my deepest gratitude to my family, who has unconditionally supported and encouraged me in the most difficult times, without whom none of this would be possible.

Contents

List of Figures

List of Tables

Nomenclature

Acronyms

AFP	*Automatic fiber placement*
ATL	*Automatic tape-laying*
BS	*Bird strike*
BVID	*Barely visible impact damage*
CAMC	*Carbon matrix composite*
CDM	*Continuum Damage Mechanics*
CFRP	*Carbon fiber reinforced polymer*
CLT	*Classical lamination theory*
CMC	*Ceramic matrix composite*
CZM	*Cohesive zone modelling*
FRP	*Fiber reinforced polymer*
FRTP	*Fiber reinforced thermoplastic*
GFRP	*Glass fiber reinforced polymer*
ISC	*In situ consolidation*
LMPAEK	*Low-melt Polyaryletherketone*
MD	*Multidirectional*
MMC	*Metal matrix composite*
OEM	*Original equipment manufacturer*
PEEK	*Polyetheretherketone*
PEKK	*Polyetherketoneketone*
PMC	*Polymer matrix composite*
PPS	*Polyphenylene sulfide*
PRA	*Particular risk analysis*
RVE	*Representative volume element*

TPC	*Thermoplastic composite*
UD	*Unidirectional*
UMAT	*User material subroutine*
VUMAT	*Vectorized user material subroutine*

Symbols

$\boldsymbol{C}$	Stiffness matrix
$\boldsymbol{C}_d$	Damaged stiffness matrix
d_d	Diffuse damage parameter
d_f	Failure damage parameter
G_C	Fracture toughness
F_{ft}	Fiber tensile strength
F_{mt}	Matrix tensile strength
X_T	Longitudinal tensile strength
X_C	Longitudinal compressive strength
Y_T	Transverse tensile strength
Y_C	Transverse compressive strength
S_L	Longitudinal shear strength
S_T	Transverse shear strength
V_f	Fiber volume
V_m	Matrix volume
$\boldsymbol{\sigma}$	Stress tensor
$\boldsymbol{\varepsilon}$	Strain tensor
σ_f	Fiber stress
σ_m	Matrix stress
ε^u_{ft}	Ultimate fiber tensile strain
ε^u_{mt}	Ultimate matrix tensile strain
E_i	Stifness modulus along the i direction of the laminate
G_{12}	Shear modulus along the ij direction of the laminate
ν_{ij}	Poisson ratio in the ij direction of the laminate

Part I

Introduction

Chapter 1

Industry Context

The aeronautical industry bases itself on achieving the best performance at the lowest possible cost, be that in weight, capital, safety or, more recently, environmental impact. This is an adage that is present at every step of the development process of aircraft. Hence, due to their remarkable specific properties and increasingly competitive prices, composites are one of the best material options for use in these applications.

The presence of composites in aircraft dates back to the early days of the aeronautical industry. Strictly speaking, it was in the 1930s that the first composites were used for this purpose. One of the most famous examples of this is the Hughes H-4 Hercules, *Spruce Goose*, which was constructed using *Duramold*, a composite made of birch wood imbued with phenolic resin, laminated and then subjected to elevated heat and pressure [1], in what is a remarkably similar process to that of modern composite manufacturing and curing. *Duramold*, along with *Haskelite* and other composites, played a significant role in the 1940s war effort by replacing aluminium alloys and steel in some aircraft parts, as these were scarce and in high demand for other industries [2].

The 1930s also saw the birth of the fibre reinforced polymer industry, when Owens Corning introduced *fibreglass* [3], with it being most prominently used in aircraft *radomes* given its radio frequency transparency, an application that continues to this day. However, it was only in the 1970s that the composites industry started to properly mature and the properties of these materials began to truly contend with their metal counterparts. This sparked the beginning of a trend in the increased use of composite materials. At first limited to the development of auxiliary and secondary parts, composites are now present in primary structures and fully-fledged assemblies of the latest aircraft, with the latest commercial jets having composite materials be responsible for about half of their structural weight, as verified in Figure 1.1.

Nevertheless, impact resistance and the residual strength of the panel is a relevant weak aspect of these materials, especially when the impact is of low velocity, resulting in barely visible impact damage (BVID), which may be overlooked or not detectable at all and may pose risks to the structural integrity of the aircraft in future flights.

The certification process of composite structures is therefore extremely conservative, both due to the complexity of the composite damage mechanisms and the lack of maturity in their use in aircraft. Currently, it is based on a building block approach, as verified in

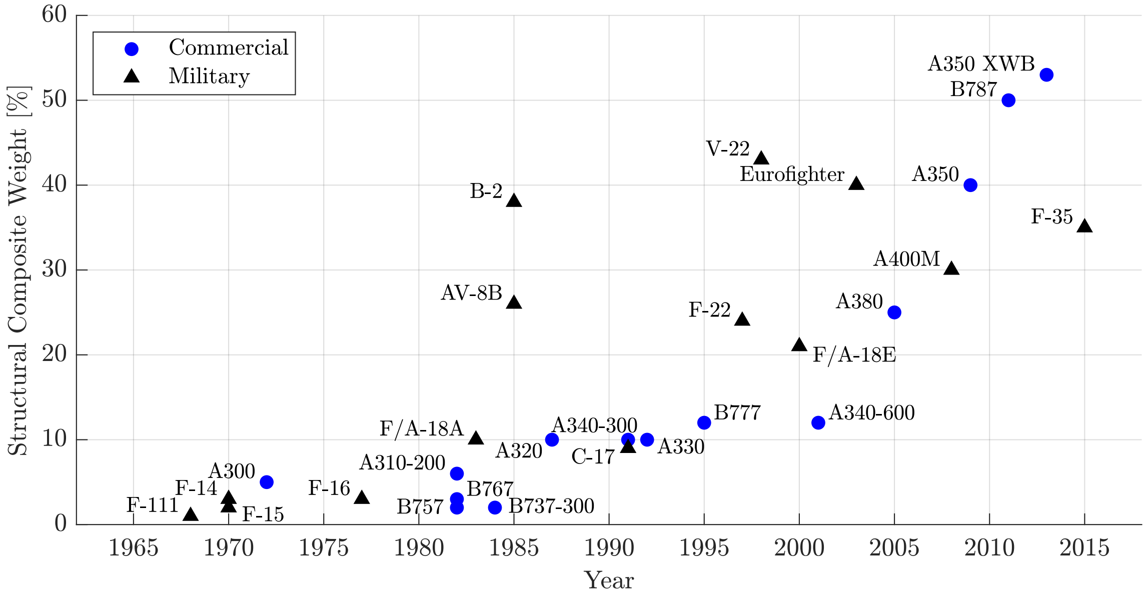

Figure 1.1: Evolution of the presence of composites in aircraft applications across the last decades (adapted from [4, 5, 6]).

Figure 1.2, from thousands of tests in the lower levels to few and quite expensive ones at the component testing level. It is due to this that structural computational simulation using the finite element method started to become imperative in the certification process, allowing for significant reductions in costs and time.

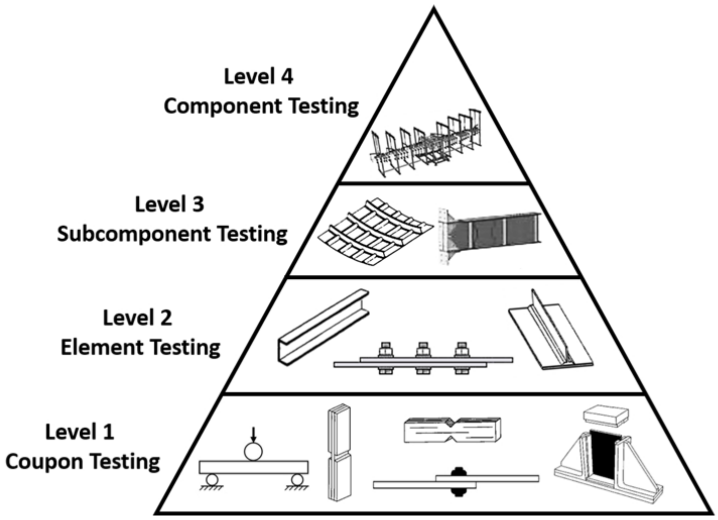

Figure 1.2: Building block approach for composite structures [7].

1.1 Thermoplastic Matrix Composites

In the late 1960s up until the 1990s, thermoplastic tapes were used to manufacture a wide range of parts, particularly in military and defence applications. Good processability, quick and easy out-of-autoclave consolidation, as well as good mechanical properties and easy to meet storage requirements were highly attractive characteristics of these materials. However, research slowed significantly in the 1990s due to lower spending budgets. This, combined with a higher focus on the development of the already well-established thermoset composites, lead to thermoplastic composites being relegated to the background of composites' R&D. Nevertheless, thermoplastics have been flying on aircraft since the 1990s, being used to make smaller parts and non-critical substructures.

Currently, with the ever-increasing use of composites in aircraft design, and production rates of the Airbus A320 and Boeing 737 workhorses projected to reach all-time highs, optimizing the production processes to achieve lower cycle times is of paramount importance for the original equipment manufacturers (OEMs). This high demand is not compatible with the production of thermosets, which require long periods of time curing in an autoclave. Thermoplastics have lower cycle times, achieved through two-stage or, optimally, one-stage manufacturing by in-situ consolidation. Favourable material storage, higher toughness and the possibility of recycling also make them highly suitable candidates for replacing thermoset composites, especially in the context of the Clean Sky 2 initiative, under which the Multi Functional Fuselage Demonstrator [8] and a one-shot thermoplastic composite wingbox cover (Figure 1.3) were produced.

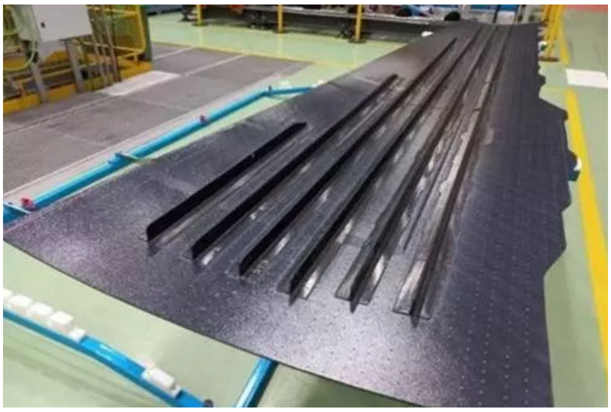

Figure 1.3: PEEK thermoplastic wingbox cover produced by the OUTCOME project under the Clean Sky 2 initiative [9].

The main aspect that must be solved before thermoplastic composites are used extensively in commercial airframes is their viability and maturity of use in highly-loaded structures. If they cannot be used in primary and secondary structures, this greatly reduces the scope of their employment in aircraft and usefulness for OEMs. However, their usability is becoming more and more apparent given that, since 2010, they have been employed in primary structures - tail planes and wings - of smaller aircraft such as business jets (the Gulfstream G650 has a carbon fiber/polyphenylene sulfide (PPS) rudder and elevator [10]).

Chapter 2

Dissertation Context

2.1 Hosting Institution

This dissertation's underlying work was carried out in the Département Mécanique des Structures et Matériaux of the Institut Supérieur de l'Aéronautique et de l'Espace, one of the leading institutions in the French aerospace research and development domain.

Most commonly referred to as ISAE-SUPAERO, the Institut Supérieur de l'Aéronautique et de l'Espace (Figure 2.1) is one of the top aerospace engineering schools in the world. Its pivotal location in Toulouse, the centre of the French aerospace scene, allows for high cooperation with the industry and contact with the latest technological breakthroughs.

Formed in 2007 from the merger of ENSAE[1] and ENSICA[2] with the purpose of synergizing the faculty and experimental means of those institutions, ISAE-SUPAERO is overseen by the French Ministry of Defence and the French Government Defence Procurement and Technology Agency. It hosts around 1900 students and 500 permanent staff, distributed through six teaching and research departments:

- Département Aérodynamique, Énergétique et Propulsion (DAEP)
- Département Conception et Conduite des Véhicules Aérospatiaux (DCAS)
- Département Mécanique des Structures et Matériaux (DMSM)
- Département Ingénierie des Systèmes Complexes (DISC)
- Département Electronique, Optronique et traitement du Signal (DEOS)
- Département Langues Arts Culture et Société (LACS)

More specifically, the internship pertaining to this dissertation took place in the Department of Mechanics, Structures and Materials, described in the following section.

2.1.1 Département Mécanique des Structures et Matériaux

The Département Mécanique des Structures et Matériaux (DMSM) supervises all teaching activities related to solid mechanics and conducts fundamental and applied research on aerospace related materials and structures.

---

[1] École Nationale Supérieure de l'Aéronautique et de l'Espace or SUPAERO

[2] École Nationale Supérieure d'Ingénieurs de Constructions Aéronautiques

Figure 2.1: ISAE-SUPAERO campus [11].

With around 60 permanent staff, it is divided into three teams. The scientific team carries out teaching and research activities, the testing and analysis team focuses on experimental material and structure testing and analysis, and the manufacturing team manages the workshop, carrying out the design and production of metallic and composite parts. This cooperation allows for the DMSM to investigate three key scientific topics:

- Durability & damage tolerance of composite and metallic materials.
- Modelling & qualification of aerospace structures under static or dynamics loadings.
- Multiphysics requirements-driven simulation and design.

Besides that, the DMSM is involved with the Institut Clément Ader in the areas of structures, impact, modelling, and machining (SIMU), and materials, properties and processes (MAPP).

A multidisciplinary team, allied with a wide range of manufacturing and testing equipment allows the DMSM to conduct advanced research activities and develop tools and methods for the design of aerospace structures that meet the needs of the industry.

2.2 Project Details

The Airbus Atlantic Research & Technology department is developing a new cockpit project aimed at proposing a design with lower mass, reduced costs of manufacturing, assembly, and integration, and optimized industrialization processes. For this, and given its promising material properties, the use of a novel thermoplastic matrix carbon fibre composite is being evaluated.

One of the PRA (particular risk analysis) critical load cases for certification of this primary structure is the bird-strike (BS) event. In this scenario, in order to have accurate virtual testing data, it is imperative that the material is properly characterized in both the static and dynamic behaviour domains. Hence, the primary overall objectives of the project are to:

1. Establish an appropriate experimental campaign and protocol to identify and characterize composite damage mechanisms, and obtain the necessary material properties for implementation in the numerical model.
2. Realize the static and dynamic material characterization tests.
3. Identify the constitutive laws responsible for the behaviour observed during the tests, develop an according material model and implement it in the commercial finite element solver Abaqus either as an user-material subroutine (UMAT) or a vectorised user-material subroutine (VUMAT).

Dissertation objectives: This work will thus specifically focus on the development of a methodology for the identification and modeling of the behaviour of thermoplastic matrix carbon fibre composite material systems.

2.3 Methodology

The development phases of the dissertation will be described in this section, noting the initially planned stages and the adjustments that had to be made to redirect the scope of the work, due to unplanned setbacks.

Initial Approach In the beginning of the internship, the planned approach was to work on the project in accordance with the objectives specified in the Airbus Atlantic proposal, while conducting parallel studies to prepare for further stages. This process is specified in the following sequence and illustrated in the Gantt chart provided in Figure 2.2.

1. Literature review of the behaviour of thermoplastic matrix composites under various loading scenarios and test conditions, and identification of typical damage and failure mechanisms, while studying the elaboration of user material subroutines in Abaqus and the programming language FORTRAN.
2. Proposal of a testing campaign that allows for the procurement of the necessary material properties and behaviours. Design and sizing of the specimens for each experiment and submission of the resulting technical drawings to Airbus Atlantic.
3. Start of development of the material model based on the behaviour of similar composites observed in the literature.
4. Once the laminate arrives from the manufacturer, cut the plates in accordance with the drawings in order to obtain the specimens and start the testing campaign.
5. Material behaviour analysis and adaptation of the constitutive model accordingly.
6. Numerical implementation of the material model in the finite element solver starting with a static approach through a UMAT subroutine, and then a dynamic one through a VUMAT subroutine.
7. Writing of the project report and dissertation.

However it was not possible to do any of the expected experimental procedures with the novel material (explained in Annex A) due to unforeseen circumstances having to

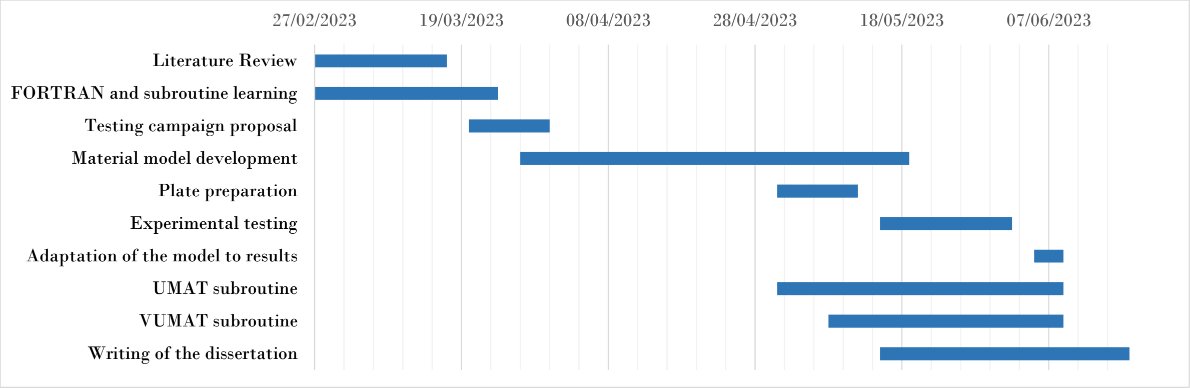

Figure 2.2: Expected project timeline.

do with the manufacturing of the composite laminate plates (displayed in Annex B). Therefore, the scope of the work changed from characterizing the material at hand, to a more generalized approach which based itself on experimental data of similar materials found in the literature. This will hopefully result in an appropriate numerical behaviour once the material ends up running through the planned experimental campaign.

Final Approach In the end, a more complex material model ended up being developed given the extension of the duration of the dissertation, adding details which would have been impossible otherwise, with the final work sequence being displayed in Figure 2.3.

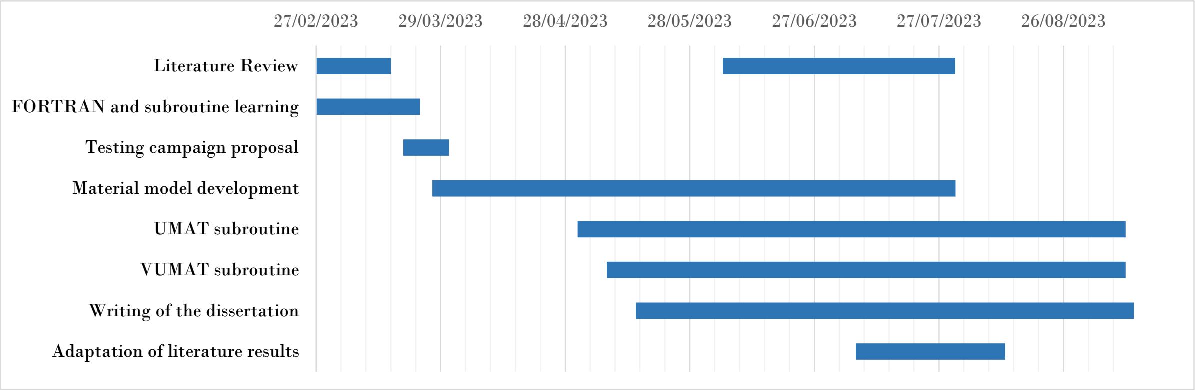

Figure 2.3: Project timeline.

2.4 Structure of the Dissertation

This dissertation has been divided into five parts and eight chapters.

Part I is the introduction of the project, which covers the industrial context behind the use of thermoplastic composites (Chapter 1) and the context in which the dissertation was developed (Chapter 2).

Part II relates to the literature review of the subjects that the dissertation covers, starting with general concepts about composites and their damage mechanisms (Chapter 3), the theory behind expressing composite material response through a mathematical formulation, i.e. its elastic behaviour, the criteria by which failure is evaluated, the concept of damage applied in a continuum and governed by mathematical laws and the fundamentals of the theory of plasticity (Chapter 4).

Part III develops the intraply constitutive model based on and extending the previously introduced literature, through the implementation of diffuse damage, plasticity, fiber rotation, failure criteria, *in situ* effect and failure damage (Chapter 5).

Part IV consists of the application of the material model in a computational framework, through the development of subroutines (Chapter 6) and the validation of the formulation by means of simulations where the behaviour is checked to verify if it corresponds to what was intended and if it matches experimental results (Chapter 7).

Part V covers the conclusions and key takeaways from the development of the project and presents suggestions for future work to further improve it (Chapter 8).

Besides this, two appendices which contain a proposed experimental testing campaign for the procurement of material properties necessary for the model (Appendix A) and the composite plate drawings designed for that same campaign (Appendix B) were included.

Part II

Literature Review

Chapter 3

Composite Materials

Produced from two or more distinct materials, composites take advantage of a synergistic effect to have mechanical properties superior to those of their individual constituents. In the case of structural composites, these usually contain a stiffer, stronger and more brittle phase - *reinforcement* - and a less stiff, weaker and more ductile phase - *matrix*.

Composites can usually be identified by the type, geometry and orientation of their reinforcing phase. There are three major categories, as illustrated in Figure 3.1, which can be described by mathematical material models. For the *particulate* type of composites, the ample distribution of their constituents results in a quasi-homogeneous material nature. *Discontinuous* or *short-fiber* composites are characterized by their anisotropy – in case the fibers are oriented along one direction, or quasi-isotropy – when they are randomly oriented. *Continuous fiber* composites are considered the most efficient due to the possibility of arranging them in unidirectional, perpendicular (right angles to each other e.g., cross-ply or woven fabric) or multidirectional arrangements, in which case they can be characterised as quasi-isotropic [12].

Besides that, fiber reinforced polymers can usually be identified by the type of material constituting their matrix. There are four primary categories: polymer matrix composites which can be either thermosets or thermoplastics, metal matrix composites, ceramic matrix composites and carbon matrix composites [13].

3.1 Laminae and Laminates

Fiber reinforced polymers are employed in structures in the form of laminates of diverse composition. Figure 3.2 illustrates the different scales by which fiber reinforced composites might be analysed, and their constituents. A *lamina* or *ply* is an orthotropic unidirectional layer of composite material, with its longitudinal axis aligned with the direction of the fibers, transverse axis normal to the fiber direction but in the plane of the lamina, and out-of-plane axis corresponding to the direction normal to the plane of the ply. These are the principal axis of the individual laminae and are designated 1, 2 and 3, respectively.

As for the *laminate*, it is composed of two or more laminae which can be stacked at the same or different orientations. The multiple possible orientations of these laminae allows

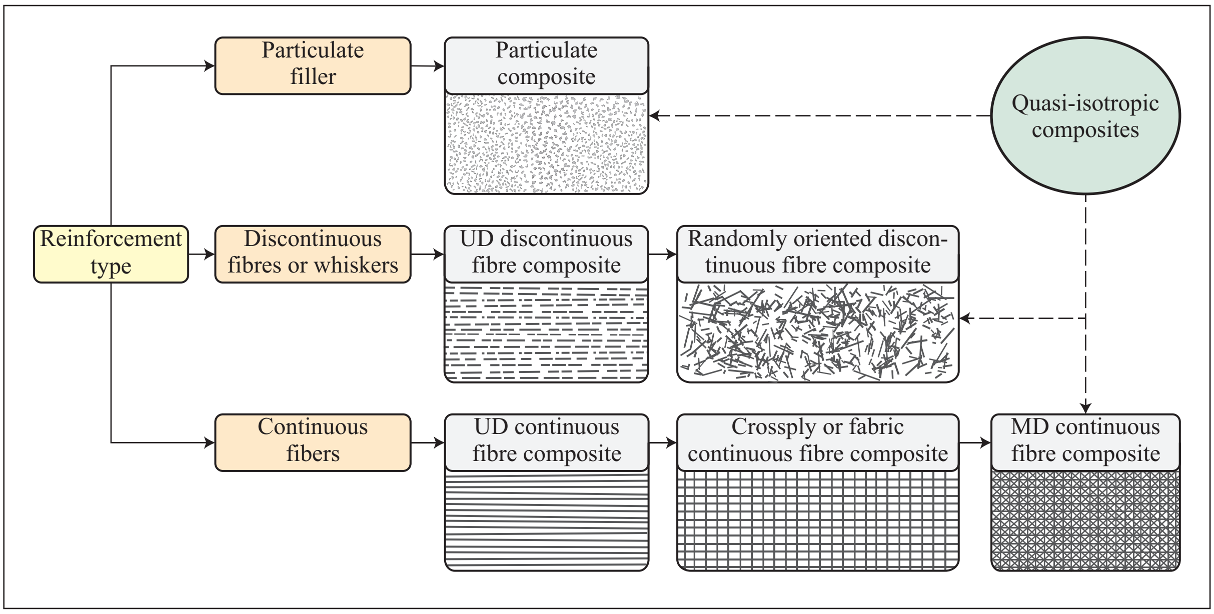

Figure 3.1: Composite material designation according to their reinforcement type (adapted from [12]).

for a custom layup solution for the specific stress-state that the structure is required to handle. Since the orientation of the laminate may not always correspond to the orientation of the individual plies that compose it, as in the case of a multidirectional laminate, the system of coordinates by which it is analysed is the classical fixed system (x,y,z).

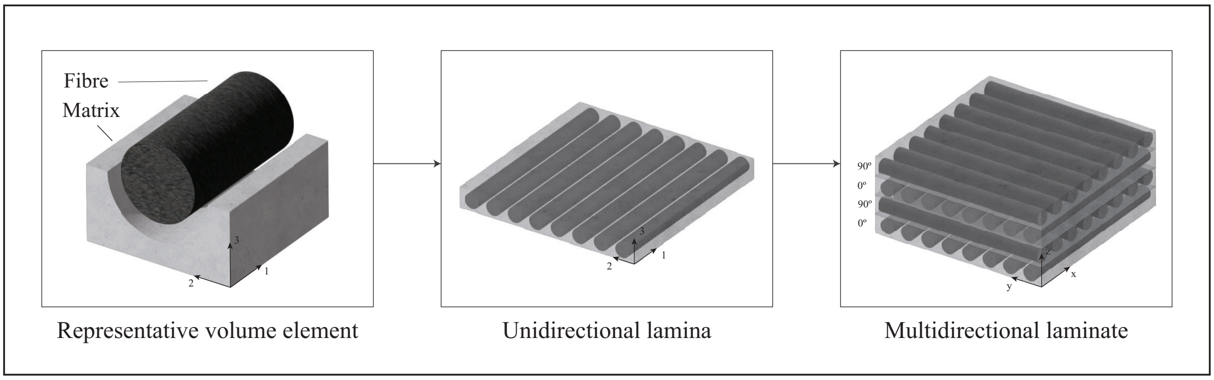

Figure 3.2: Schematic representation of the several scales of fiber reinforced composites, where $(1, 2, 3)$ corresponds to the ply's local coordinate system and (x, y, z) to the laminate's global coordinate system.

3.2 Thermoplastic Matrix Reinforced Composites

Unlike thermoset polymers which cross-link during curing, thereby forming irreversible chemical bonds (Figure 3.3), thermoplastics are fully polymerized polymers that can usually be repeatedly softened by heating and hardened by cooling. This has the heightened advantage of allowing recycling the composites with this type of matrix, reducing their overall environmental impact.

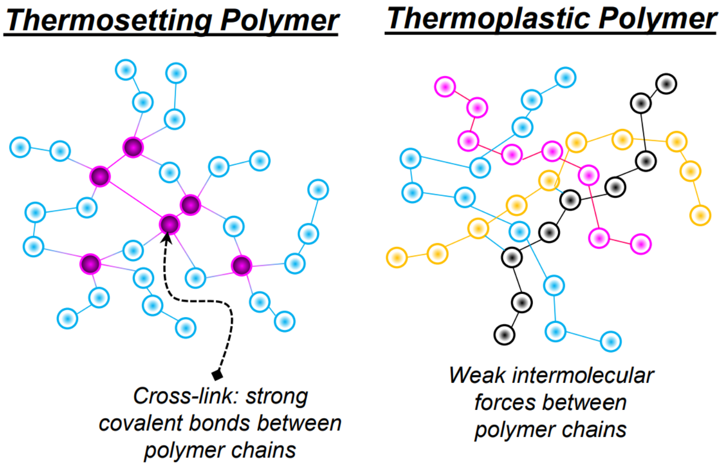

Figure 3.3: Molecular arrangement of thermosetting and thermoplastic polymers [14].

Besides that, thermoplastic composites have advantages in relation to thermosets in what concerns high strain to failure, high fracture toughness and damage tolerance, longer shelf life and the ability to reshape and reuse. However, this comes with certain disadvantages such as reduced performance to cost ratio and manufacturing difficulties. Moreover, given that thermoplastic resins have high viscosities at processing temperatures, inadequate impregnation might occur, leading to large void content.

Nevertheless, thermoplastics with welded interfaces may allow the significant reduction of the need for mechanical fasteners, decreasing stress concentration phenomena in the areas where they are present. However, anti-peeling fasteners or chicken rivets should still be installed at all critical stringer run-out areas.

The use of these composites allows for the *in situ* consolidation (ISC) of parts. ISC via automatic tape-laying (ATL) or automatic fiber placement (AFP) consists of heating prepegged thermoplastic tapes or tows in the tape head up to their melt temperature, place them on the tool, where they are immediately consolidated by the end-effector. Although an additional high-pressure consolidation step is currently required to achieve porosity targets this process is ultimately expected to provide 100% consolidation in a single step. Despite lacking maturity, this manufacturing process could prove to be revolutionary regarding the time and costs of composite production [15].

Expanding upon this notion, some relevant aspects of thermoplastic composite manufacturing are that:

1. Curing is not necessary.
2. Residual stresses are related to the basic material properties and processing temperatures, which are usually higher for thermoplastics.
3. They have reduced tendency for delamination.
4. Fiber movement occurs during thermoforming and welding.
5. They have increased tendency for resin rich areas.
6. Variation in the crystalline morphology might occur due to the difference in the cooling rate within the components, leading to changes in the mechanical properties.

3.3 Damage Mechanisms in Unidirectional Laminae

The heterogeneous and anisotropic nature of composites leads to rather distinct failure modes when compared to more conventional materials. This is due to the complex interactions between the reinforcement and matrix constituents resulting from different material properties, also influencing the fiber-matrix interface. It is thus of no surprise that a plethora of different damage mechanisms arises from this coupled nature.

3.3.1 Longitudinal Tension

When composites are loaded in tension, failure will typically occur in the constituent with the lowest ultimate strain. For a longitudinal loading scenario, the composite will fail when the ultimate tensile strain of the fiber is reached. Assuming a homogenized, uniform value for the fiber's properties, the composite strength can be given by the following equation, as a direct result of the Rule of Mixtures [12], where a distinction is made between the case where the ultimate fiber tensile strain ε_{ft}^{u} is lower than the ultimate matrix tensile strain ε_{mt}^{u} and vice-versa:

$$\begin{cases} X_T = F_{ft}V_f + \sigma_m V_m & \text{when } \varepsilon_{ft}^{u} < \varepsilon_{mt}^{u} \\ X_T = F_{mt}V_m + \sigma_f V_f & \text{when } \varepsilon_{mt}^{u} < \varepsilon_{ft}^{u} \end{cases} \tag{3.1}$$

where X_T, F_{ft} and F_{mt} are the longitudinal, fiber and matrix tensile strengths, σ_f and σ_m are the average longitudinal fiber and matrix stress when the ultimate strain is reached, and V_f and V_m are the fiber and matrix volumes, respectively.

However, this approach does not take into consideration the variation of fiber and matrix properties across the laminate. In fact, the strength of the fibers will have a statistical distribution, varying across their length and between themselves. Furthermore, once the weakest fiber fails, a non-uniform stress state is formed around it, leading to stress redistribution governed by the fiber-matrix interface which transfers the stress back to the fiber after a certain distance. As such, the fiber breakage process is inherently of a statistical nature [16].

In the case of a relatively ductile matrix and strong interface, such as what is verified in the thermoplastic matrix composites, fiber breakage leads to a failure mechanism in the form of conical shear fractures in the matrix. With increased loading, more and singlets are formed, eventually coalescing and spreading across the span of the laminate, which ultimately leads to catastrophic failure.

3.3.2 Longitudinal Compression

Compressive failure on composites can occur due to various mechanisms, identified by Budiansky and Fleck [17] and illustrated in Figure 3.4, where:

(a) **Elastic micro-buckling** is a shear buckling instability.

(b) **Fiber kinking** is a plastic shear instability due to significant shearing of the matrix. Also referred to as plastic micro-buckling.

(c) **Fiber crushing** consists of the fiber failure prior to the matrix.

(d) **Shear band formation** precedes in-phase micro-buckling at high values of V_f and for well aligned fibers. Failure occurs in a band oriented at around 45° in relation to the loading axis due to shear-driven failure of the fibers.

(e) **Matrix cracking** is similar to the longitudinal tensile failure of the matrix.

(f) **Buckle delamination** relates to an out-of-plane buckling where the whole ply delaminates due to insufficient bonding.

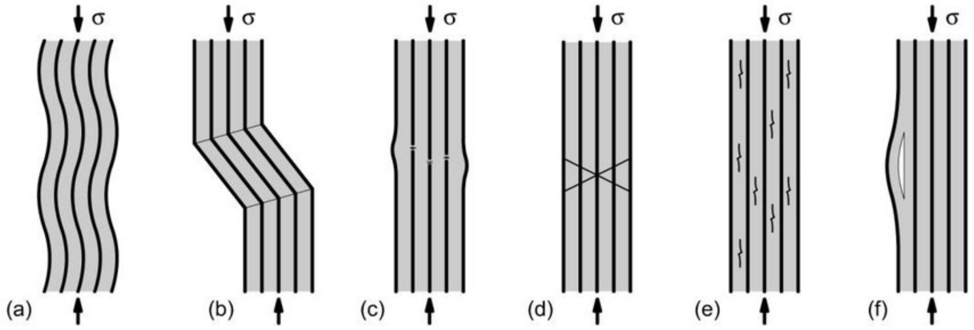

Figure 3.4: Failure modes in composites under compressive loading. (a) elastic micro-buckling (b) fiber kinking (c) fiber crushing (d) shear band formation (e) matrix cracking (f) buckle delamination [18].

Of these, fiber kinking proves to be the dominant failure mode in unidirectional composites, and specifically in the thermoplastic matrix composite AS4/PEEK, as can be observed in the compressive failure map in Figure 3.5.

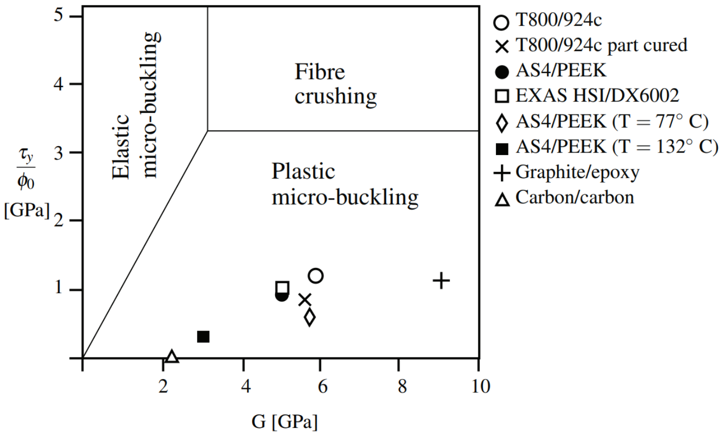

Figure 3.5: Compressive failure map highlighting three modes of failure [17, 19].

According to Rosen [20], there are two idealized patterns of micro-buckling deformation (Figure 3.6). For low fiber volume (V_f) ratios, the extensional or out-of-phase mode is predicted. Conversely, the shear or in-phase mode is anticipated for higher V_f values.

In-phase micro-buckling might lead to high flexural stresses and large shearing of the matrix, causing plastic micro-buckling or kink band formation. Depending on the nature of the fibers, severe deformation or fracture can occur, as illustrated in Figure 3.7a. A real-life example of kink band formation in a thermoplastic matrix composite can be found in Figure 3.7b.

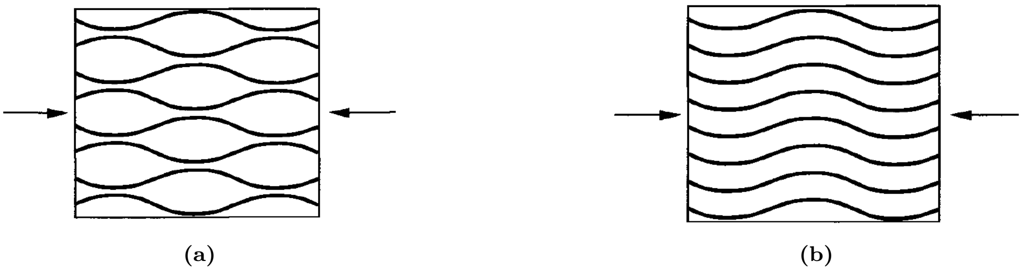

Figure 3.6: Micro-buckling modes in unidirectional lamina under longitudinal compression: (a) out-of-phase or extensional and (b) in-phase or shear modes [12].

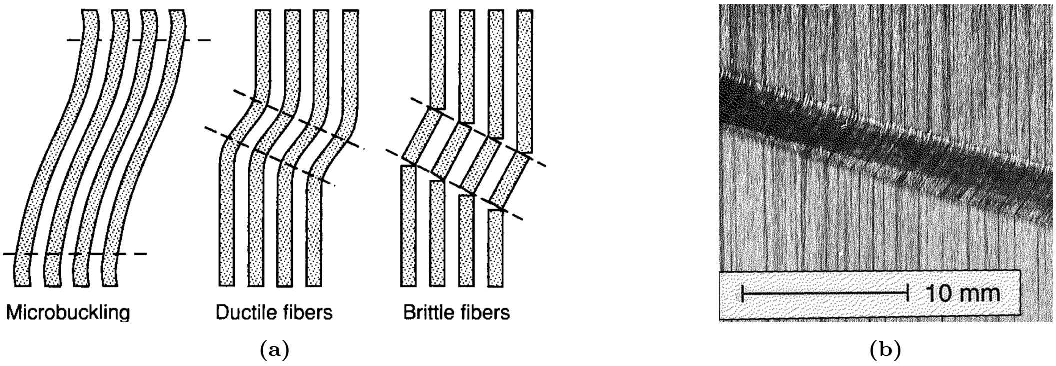

Figure 3.7: (a) micro-buckling leading to the formation of kink bands with high deformation, or even fracture planes [12] and (b) kink band formation in the AS4/PEEK composite [18].

3.3.3 Transverse Tension

Failure under this type of loading emerges from high stress and strain concentrations in the matrix and in the fiber-matrix interface, where progressive fracture occurs until a catastrophic crack emerges. It is possible to observe in Figure 3.8 a micrograph of the occurrence of this crack coalescence phenomenon, from where it can be verified that the first phase of failure comprises fiber-matrix debonding, which then leads to the combination of those isolated crack into a unified one. Besides the loading state, this failure mechanism is also influenced by curing and hygrothermal stresses, derived from the manufacturing of the composite and the ambient conditions where it is situated, respectively [12].

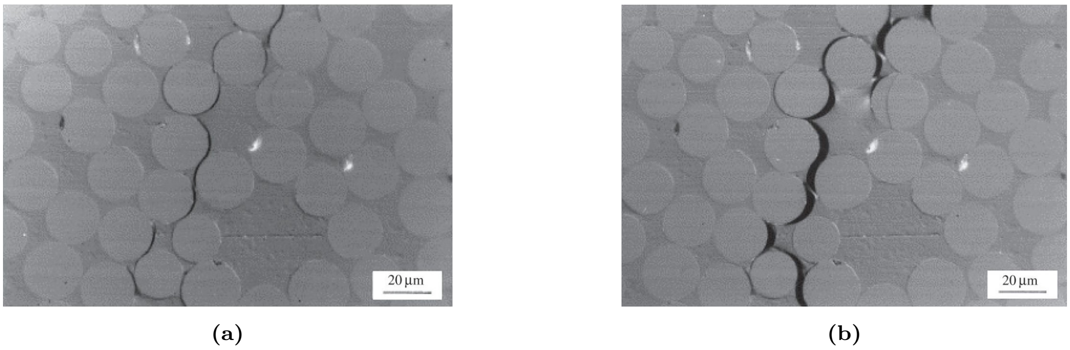

Figure 3.8: Crack formation mechanism under transverse loading where (a) initial fiber-matrix debonding occurs and (b) the micro-cracks propagate, creating a unified transverse fissure [21].

3.3.4 Transverse Compression

This type of loading may lead to two fundamental failure mechanisms according to Daniel and Ishai [12]. On the one hand, high compressive stress may lead to compressive or shear failure of the matrix, or fiber crushing, on the other, high interfacial shear stresses may lead to matrix shear failure or fiber matrix debonding. This shear dominated failure modes are corroborated by observations of Agarwal et al. [22], that show inclined planes in relation to the loading direction, as can be verified in Figure 3.9.

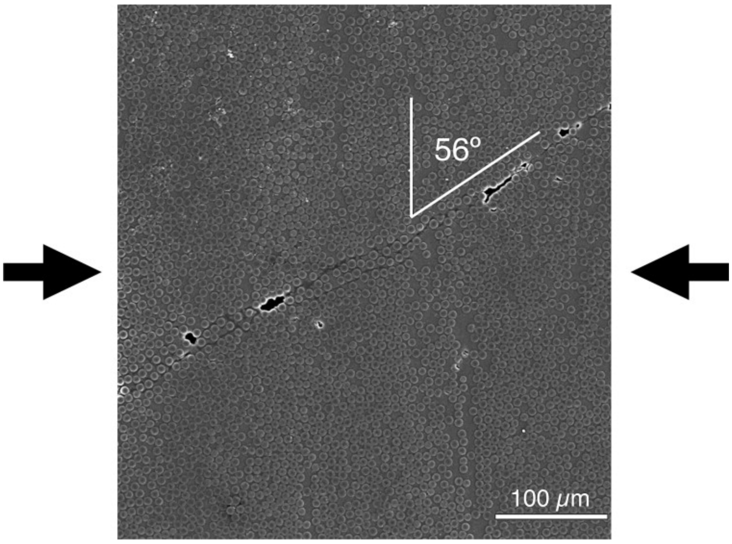

Figure 3.9: Micrograph of the lateral surface of AS4/Epoxy specimen under transverse compression, where the formation of a fracture plane is visible [23].

3.3.5 In-plane Shear

In this load scenario, high shear stresses develop at the fiber matrix interface, leading to the development of microcracks in the matrix, oriented along the fiber direction, as can be observed in Figure 3.10

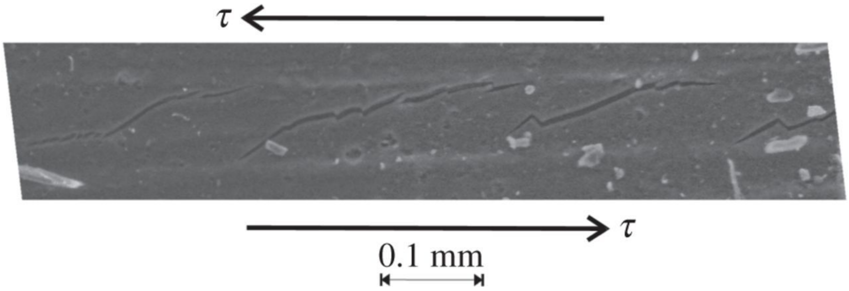

Figure 3.10: Micrograph of crack formation under in-plane shear stress, shown as τ [24].

Chapter 4

Mathematical Model

It is necessary to consider several different mechanisms of composite behaviour in order to express its response through mathematical laws. The elastic behaviour of composites, appropriate failure criteria, continuum damage mechanics and the occurrence of plasticity will be introduced in this chapter.

4.1 Elastic Behaviour

Given that an orthotropic material has at least two orthogonal planes of symmetry, as is the case with fiber reinforced laminates, only nine elastic constants are necessary for the establishment of its constitutive model, as opposed to 21 for an anisotropic material [12].

Therefore, the stiffness matrix for composites, derived from the inverse of the compliance matrix established by Hooke's Law [25], is given by:

$$\begin{bmatrix} \sigma_{xx} \\ \sigma_{yy} \\ \sigma_{zz} \\ \sigma_{yz} \\ \sigma_{zx} \\ \sigma_{xy} \end{bmatrix} = \begin{bmatrix} \frac{1-\nu_{yz}\nu_{zy}}{E_y E_z \Delta} & \frac{\nu_{yx}+\nu_{zx}\nu_{yz}}{E_y E_z \Delta} & \frac{\nu_{zx}+\nu_{yx}\nu_{zy}}{E_y E_z \Delta} & 0 & 0 & 0 \\ \frac{\nu_{xy}+\nu_{xz}\nu_{zy}}{E_z E_x \Delta} & \frac{1-\nu_{zx}\nu_{xz}}{E_z E_x \Delta} & \frac{\nu_{zy}+\nu_{zx}\nu_{xy}}{E_z E_x \Delta} & 0 & 0 & 0 \\ \frac{\nu_{xz}+\nu_{xy}\nu_{yz}}{E_x E_y \Delta} & \frac{\nu_{yz}+\nu_{xz}\nu_{yx}}{E_x E_y \Delta} & \frac{1-\nu_{xy}\nu_{yx}}{E_x E_y \Delta} & 0 & 0 & 0 \\ 0 & 0 & 0 & 2G_{yz} & 0 & 0 \\ 0 & 0 & 0 & 0 & 2G_{zx} & 0 \\ 0 & 0 & 0 & 0 & 0 & 2G_{xy} \end{bmatrix} \begin{bmatrix} \varepsilon_{xx} \\ \varepsilon_{yy} \\ \varepsilon_{zz} \\ \varepsilon_{yz} \\ \varepsilon_{zx} \\ \varepsilon_{xy} \end{bmatrix} \tag{4.1}$$

where E_{ij} and G_{ij} are the stiffness and shear modulus and ν_{ij} the Poisson ratio in the principal laminate directions ij and,

$$\Delta = \frac{1 - \nu_{xy}\nu_{yx} - \nu_{yz}\nu_{zy} - \nu_{zx}\nu_{xz} - 2\nu_{xy}\nu_{yz}\nu_{zx}}{E_x E_y E_z} \tag{4.2}$$

Since the stiffness matrix is symmetric, the following statements must be obeyed:

$$\begin{cases} \frac{\upsilon_{yx}+\upsilon_{zx}\upsilon_{yz}}{E_y E_z \Delta} = \frac{\upsilon_{xy}+\upsilon_{xz}\upsilon_{zx}}{E_z E_x \Delta} \\ \frac{\upsilon_{zy}+\upsilon_{zx}\upsilon_{xy}}{E_z E_x \Delta} = \frac{\upsilon_{zy}+\upsilon_{xz}\upsilon_{yz}}{E_x E_y \Delta} \\ \frac{\upsilon_{zx}+\upsilon_{yx}\upsilon_{zy}}{E_y E_z \Delta} = \frac{\upsilon_{xz}+\upsilon_{xy}\upsilon_{yz}}{E_x E_y \Delta} \end{cases} \tag{4.3}$$

4.2 Failure Theory

In order to construct effective structures, it is necessary to use materials that can handle the forces which they are required to sustain. Once the stress or strain field imposed upon the material surpasses that which it can handle, local fracture occurs, which can lead to catastrophic failure of the part. Failure theory is used to establish the stress or strain domain to which the material can safely be subjected. This study of failure can be undertaken in different manners and with different levels of detail, depending on the type of material (homogeneous, orthotropic, transversely isotropic, monoclinic, to name a few), expected stress fields (3D stress state, plane stress, plane strain, among other) and how critical the component at hand is (primary versus secondary structures in aircraft, for example).

The first failure theories developed for composites were proposed by taking failure criteria initially developed for homogeneous and isotropic materials and extending them to account for the anisotropy in the stiffness and strength of the laminae. These non-phenomenological formulations are usually less demanding of computational power and some even take into account stress interaction, depending on the availability of experimental data [26]. Overall, the failure theories can be distinguished into three groups: limit, interactive and phenomenological criteria.

Formulations that fall under these types will be compared and their failure envelopes displayed under certain fundamental stress scenarios. Unless otherwise specified, the material used is the IM7/8552 composite, whose properties are shown in Table 4.1.

Table 4.1: IM7/8552 material properties used in the calculation of the failure envelopes shown in this Chapter. Values sourced from Gan et al. [27], Camanho and Lambert [28], Catalanotti et al. [29], Koerber et al. [30] and Camanho et al. [31].

E_1 [MPa]	161000 [27]	ν_{23}	0.435 [27]	S_L [MPa]	89.5 [30]
E_2 [MPa]	11400 [27]	X_T [MPa]	2323.5 [29]	S_T [MPa]	75 [29]
. G_{12} [MPa]	5290 [28]	X_C [MPa]	1017.5 [29]	α_0	55.3 [29]
G_{23} [MPa]	3980 [27]	Y_T [MPa]	160.2 [29]	β	2.12E-8 [31]
ν_{12}	0.32 [27]	Y_C [MPa]	255 [30]		

4.2.1 Limit Failure Criteria

These criteria assess failure by directly comparing the value of the primary stress or strain components with the limit values obtained in experimental results of tests done in those directions. They have the great advantage of being extremely simple to implement and, likewise, having small computational cost.

4.2.1.1 Maximum Stress Criterion

One of the most fundamental failure theories, the maximum stress criterion, initially developed by Rankine [32], states that failure occurs when a stress component in a principal direction is higher than the material's strength in that direction. It doesn't account for stress interaction and distinguishes between longitudinal and transverse tension and compression, and shear stress failure modes. Failure occurs when the failure index F_{ij} is equal to one, according to the following formulation:

$$\text{Longitudinal:} \begin{cases} F_{1t}^{\sigma} = \frac{\sigma_{11}}{X_T} & \text{, for } \sigma_{11} > 0 \\ F_{1c}^{\sigma} = \frac{|\sigma_{11}|}{X_C} & \text{, for } \sigma_{11} < 0 \end{cases} \tag{4.4}$$

$$\text{Transverse:} \begin{cases} F_{2t}^{\sigma} = \frac{\sigma_{22}}{Y_T} & \text{, for } \sigma_{22} > 0 \\ F_{2c}^{\sigma} = \frac{|\sigma_{22}|}{Y_C} & \text{, for } \sigma_{22} < 0 \end{cases} \tag{4.5}$$

$$\text{Shear: } F_{12}^{\sigma} = \frac{|\tau_{12}|}{S_L} \tag{4.6}$$

where X_T and X_C are the longitudinal tensile and compressive strengths, Y_T and Y_C are the transverse tensile and compressive strengths, and S_L is the in-plane shear strength.

Failure Envelope: The failure envelopes resulting from the application of the maximum stress criteria to the σ_{11}-σ_{22} and σ_{22}-σ_{12} stress spaces are illustrated in Figure 4.1.

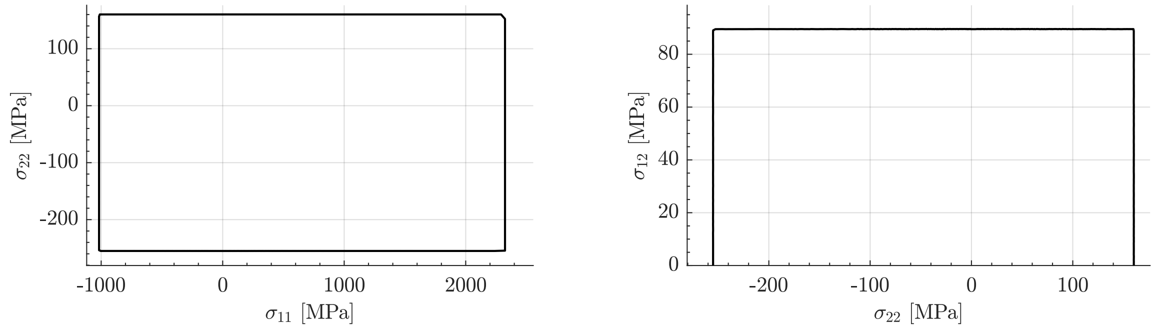

(a) (b)

Figure 4.1: Maximum stress criterion for (a) σ_{11}-σ_{22} and (b) σ_{22}-σ_{12} failure envelopes.

4.2.1.2 Maximum Strain Criterion

In a similar fashion to the maximum stress criterion, the maximum strain criterion relies on comparing the strain state to the principal uniaxial failure strains in order to determine the occurrence of failure. Poisson's effect allows for some interaction between the stress components, as can be verified in Equations 4.10 and 4.11.

$$\text{Longitudinal:} \begin{cases} F_{1t}^{\varepsilon} = \frac{\varepsilon_{11}}{\varepsilon_{1t}^{f}} & \text{, for } \varepsilon_{11} > 0 \\ F_{1c}^{\varepsilon} = \frac{|\varepsilon_{11}|}{\varepsilon_{1c}^{f}} & \text{, for } \varepsilon_{11} < 0 \end{cases} \tag{4.7}$$

$$\text{Transverse: } \begin{cases} F^{\varepsilon}_{2t} = \frac{\varepsilon_{22}}{\varepsilon^{f}_{2t}} & \text{, for } \varepsilon_{22} > 0 \\ F^{\varepsilon}_{2c} = \frac{|\varepsilon_{22}|}{\varepsilon^{f}_{2c}} & \text{, for } \varepsilon_{22} < 0 \end{cases} \tag{4.8}$$

$$\text{Shear: } F^{\varepsilon}_{12} = \frac{|\varepsilon_{12}|}{\varepsilon^{f}_{12}} = \frac{|\gamma_{12}|}{\gamma^{f}_{12}} \tag{4.9}$$

The expression of this criterion in terms of stresses is given by the following equation, with failure occurring when the equivalent stress is equal to or greater than the maximum strength in that direction [12].

$$\text{Longitudinal: } \sigma_{11} - \nu_{12}\sigma_{22} - \nu_{13}\sigma_{33} = \begin{cases} X_T & \text{, for } \varepsilon_{11} > 0 \\ X_C & \text{, for } \varepsilon_{11} < 0 \end{cases} \tag{4.10}$$

$$\text{Transverse: } \sigma_{22} - \nu_{21}\sigma_{11} - \nu_{23}\sigma_{33} = \begin{cases} Y_T & \text{, for } \varepsilon_{22} > 0 \\ Y_C & \text{, for } \varepsilon_{22} < 0 \end{cases} \tag{4.11}$$

$$\text{Shear: } |\tau_{12}| = S_L \tag{4.12}$$

Failure Envelope: While the failure envelope of the maximum strain criteria under the strain-based formulation given by Equations 4.7, 4.8 and 4.9 presents a similar nature to that of the maximum stress criterion, when it is expressed in relation to the stresses, Poisson's effect has a visible impact in the σ_{11}-σ_{22} envelope, resulting in sloped boundaries, visible in Figure 4.2a. Not affected by this phenomenon, the shear failure envelope σ_{22}-σ_{12} remains as it was under the maximum stress criterion, as it can be verified by comparing Figures 4.1b and 4.2b.

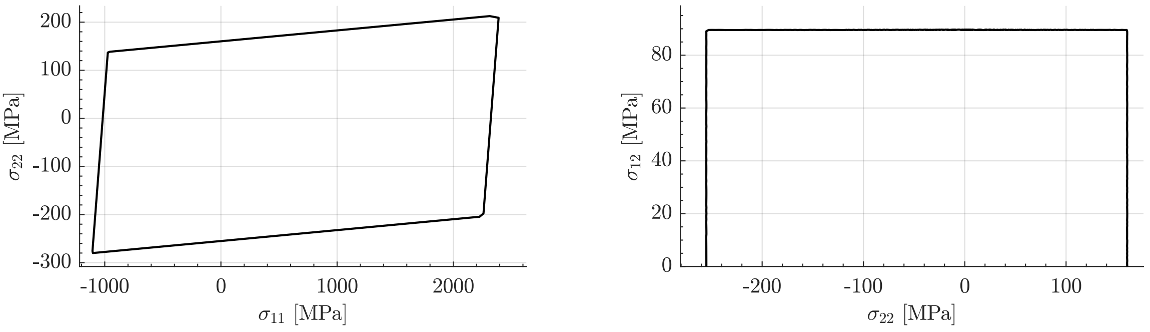

(a) **(b)**

Figure 4.2: Maximum strain criterion expressed in terms of stress. (a) σ_{11}-σ_{22} and (b) σ_{22}-σ_{12} failure envelopes.

4.2.2 Interactive Failure Criteria

This kind of criteria has better consideration for the interaction of stress components by considering bi-axial testing data which provides a more accurate failure envelope. Although criteria of this type consider all stress components in one expression, which allows them to also be referred to as polynomial criteria [33], they do not identify the particular mode by which failure occurred.

4.2.2.1 Tsai-Hill Criterion

Based on the deviatoric strain energy concept, the Tsai-Hill approach stems from a modification of the von Mises yield criterion for the case of anisotropic ductile metals by Hill [34] and further adaptation to transversely isotropic unidirectional composite laminae by Azzi and Tsai [35]. In a two-dimensional stress state, the Tsai-Hill criterion is given as:

$$\frac{{\sigma_{11}}^2}{{F_1}^2}+\frac{{\sigma_{22}}^2}{{F_2}^2}+\frac{{\sigma_{12}}^2}{{F_6}^2}-\frac{\sigma_{11}\sigma_{22}}{{F_1}^2}=1 \tag{4.13}$$

where $F_6 = S_L$ and, since this theory does not consider any distinction between tensile and compressive strengths, the F_1 and F_2 components are adapted to the stress state:

$$F_1=\begin{cases} X_T & \text{, for } \sigma_{11}>0 \\ X_C & \text{, for } \sigma_{11}<0 \end{cases} \tag{4.14}$$

$$F_2=\begin{cases} Y_T & \text{, for } \sigma_{22}>0 \\ Y_C & \text{, for } \sigma_{22}<0 \end{cases} \tag{4.15}$$

Failure Envelope: The failure envelopes resulting from the application of this formulation to the σ_{11}-σ_{22}, σ_{11}-σ_{12} and σ_{22}-σ_{12} are shown in Figure 4.3. It is possible to verify that, on pure stress scenarios, e.g. only σ_{11}, failure still occurs at the maximum strength of the material. However, in between those states, the given point of failure is much more nuanced than the previous limit type criteria, due to the greater interaction between the different stress components.

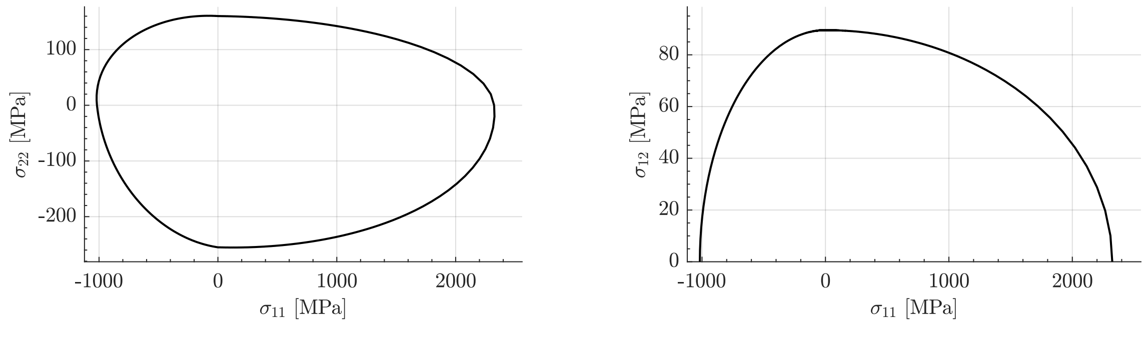

(a) **(b)**

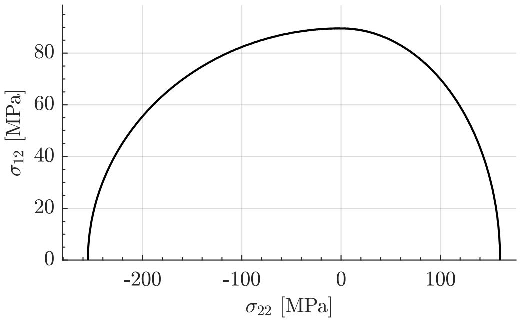

(c)

Figure 4.3: Tsai-Hill criteria for (a) σ_{11}-σ_{22}, (b) σ_{11}-σ_{12} and (c) σ_{22}-σ_{12} failure envelopes.

4.2.2.2 Tsai-Wu Criterion

Tsai and Wu [26] proposed a modified tensor polynomial theory by assuming the existence of a failure surface in the stress space. Developed for use in orthotropic or transversely isotropic laminae, requiring only simple modifications for isotropic and plane stress cases, this criterion allows for distinction between tensile and compressive strengths and interaction between the normal stresses, with the possibility of determining the interaction coefficients experimentally.

Like the Tsai-Hill criterion, it is expressed as a single criterion which is operationally simple and easily implemented in a computational scenario. Its formulation for a three-dimensional stress state is established as:

$$\begin{aligned} &f_1\sigma_1 + f_2(\sigma_2+\sigma_3) + f_{11}{\sigma_1}^2 + f_{22}({\sigma_2}^2+{\sigma_3}^2) + f_{44}{\tau_4}^2 \\ &+ f_{66}({\tau_5}^2+{\tau_6}^2) + 2f_{12}(\sigma_1\sigma_2+\sigma_1\sigma_3) + 2f_{23}\sigma_2\sigma_3 = 1 \end{aligned} \tag{4.16}$$

and in a plane stress state (σ_1, σ_2, σ_6) as:

$$f_1\sigma_1 + f_2\sigma_2 + f_{11}{\sigma_1}^2 + f_{22}{\sigma_2}^2 + f_{66}{\tau_6}^2 + 2f_{12}\sigma_1\sigma_2 = 1 \tag{4.17}$$

where the coefficients are obtained by applying elementary loads to the laminae. For example, in the case of longitudinal tension where $\sigma_1 = X_T$ and the rest of the stress components are null, the following relation is true: $f_1X_T + f_{11}{X_T}^2 = 1$. Combining this expression with the one obtained for longitudinal compression: $-f_1X_C + f_{11}{X_C}^2 = 1$ allows solving for f_1 and f_{11}.

Failure Envelope: Figure 4.4 thus presents the failure envelopes resulting from the application of the Tsai-Wu criteria on the σ_{11}-σ_{22}, σ_{11}-σ_{12} and σ_{22}-σ_{12} stress states.

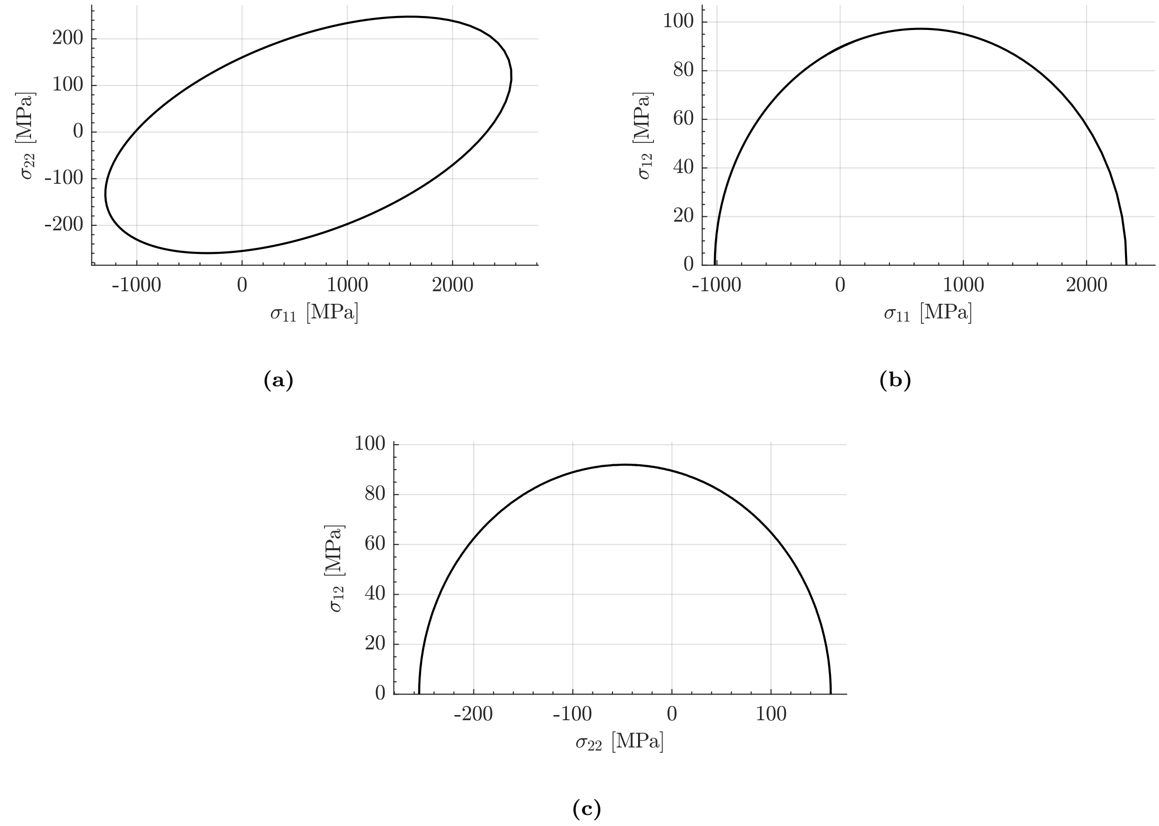

(a)

(b)

(c)

Figure 4.4: Tsai-Wu criteria for (a) σ_{11}-σ_{22} (b) σ_{11}-σ_{12} and (c) σ_{22}-σ_{12} failure envelopes.

4.2.3 Phenomenological Failure Criteria

Criteria of this type have a physical based formulation, not only taking into account the directionality of failure but its nature and the phenomena that lead to it. Given that failure stems from the accumulation of micro-mechanical damage mechanisms, understanding them and expressing that behaviour in a mathematical formulation leads to more accurate results. Nevertheless, in some cases, this approach might not be optimal due to the increased complexity and larger computational effort that is required to implement it.

4.2.3.1 Linde Failure Criteria

Based on a meso-level approach which considers the laminate layer as an homogeneous material with orthotropic constitutive parameters, the failure criteria developed by Linde et al. [36] encompasses the fiber fracture and matrix cracking failure modes.

It has a strain-based continuum damage mechanics formulation, with different conditions for fiber and matrix failures. Matrix failure is evaluated through the following formulation:

$$f_m = \sqrt{\frac{\varepsilon_{22}^t}{\varepsilon_{22}^c}(\varepsilon_{22})^2 + \left(\varepsilon_{22}^t - \frac{(\varepsilon_{22}^t)^2}{\varepsilon_{22}^c}\right)\varepsilon_{22} + \left(\frac{\varepsilon_{22}^t}{\varepsilon_{12}^s}\right)^2 (\varepsilon_{12})^2} \tag{4.18}$$

where ε_{22}^t and ε_{22}^c are the transverse failure strains under tension and compression, respectively, and ε_{12}^s is the shear failure strain. Failure occurs if f_m reaches the value of ε_{22}^t. Regarding fiber fracture, the criterion is given by:

$$f_f = \sqrt{\frac{\varepsilon_{11}^t}{\varepsilon_{11}^c}(\varepsilon_{11})^2 + \left(\varepsilon_{11}^t - \frac{(\varepsilon_{11}^t)^2}{\varepsilon_{11}^c}\right)\varepsilon_{11}} \tag{4.19}$$

where ε_{11}^t and ε_{11}^c are the failure strains for fiber direction tension and compression. In this case, failure occurs when f_f reaches ε_{11}^t.

Failure Envelope: The failure envelopes under the Linde formulation are given in Figure 4.5 for the strain states ε_{11}-ε_{22} and ε_{22}-ε_{12}. Interestingly, the ε_{11}-ε_{22} failure envelope presents a nature similar to that of the maximum strain criteria.

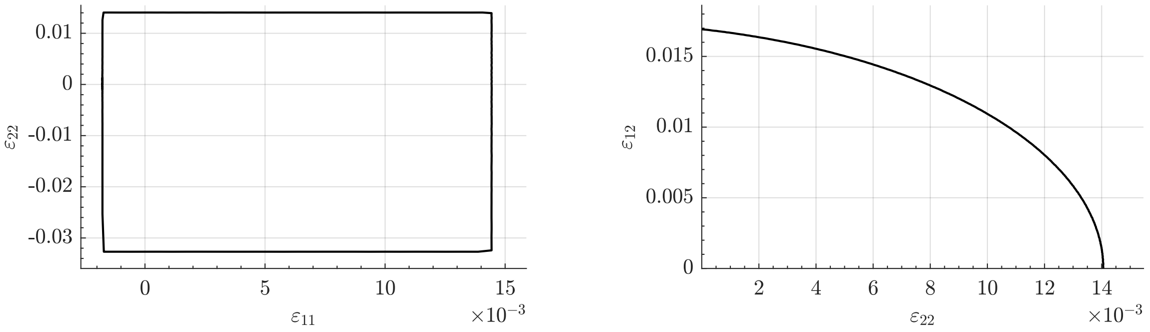

(a) **(b)**

Figure 4.5: Linde criteria for (a) ε_{11}-ε_{22} and (b) ε_{22}-ε_{12} failure envelopes.

4.2.3.2 Hashin Failure Criteria

Given the noticeable differences between the behaviour of composites in fiber and transverse directions, in both tension and compression, Hashin proposed a set of interactive criteria that consider failure modes in these directions, in both planar and three-dimensional stress states [37].

Tensile Fiber Mode: $\sigma_{11} > 0$

$$\left(\frac{\sigma_{11}}{X_T}\right)^2 + \frac{{\sigma_{12}}^2 + {\sigma_{13}}^2}{{S_L}^2} = 1 \quad \text{or} \quad \sigma_{11} = X_T \tag{4.20}$$

Compressive Fiber Mode: $\sigma_{11} < 0$

$$\sigma_{11} = -X_C \tag{4.21}$$

Hashin does not consider the effect of fiber kinking in this failure mode, relying on the maximum stress criterion to evaluate failure until that mechanism is better understood and thorough experimental investigation is conducted.

Tensile Matrix Mode: $\sigma_{22} + \sigma_{33} > 0$

$$\left(\frac{\sigma_{22} + \sigma_{33}}{Y_T}\right)^2 + \frac{{\sigma_{23}}^2 - \sigma_{22}\sigma_{33}}{{S_T}^2} + \frac{{\sigma_{12}}^2 + {\sigma_{13}}^2}{{S_L}^2} = 1 \tag{4.22}$$

where S_L is the in-plane shear strength and S_T is the transverse shear strength.

Compressive Matrix Mode: $\sigma_{22} + \sigma_{33} > 0$

$$\left[\left(\frac{Y_C}{2S_T}\right)^2 - 1\right]\left(\frac{\sigma_{22} + \sigma_{33}}{Y_C}\right) + \frac{(\sigma_{22} + \sigma_{33})^2}{4{S_T}^2} + \frac{({\sigma_{23}}^2 - \sigma_{23}\sigma_{33})}{{S_T}^2} + \frac{{\sigma_{12}}^2 + {\sigma_{13}}^2}{{S_L}^2} = 1 \tag{4.23}$$

Like the previous criteria, these are also quadratic polynomials of stresses but they are derived from the first four transversely isotropic stress invariants. Hashin assumes that the fracture plane for the matrix mode is the maximum transverse shear plane, however this may not be always true [38]. A more general approach based on the Mohr-Coulomb failure theory for matrix failure is considered to be more effective and was therefore considered by Puck and Schürmann in the development of their matrix failure criteria [39].

Failure Envelope: The failure envelopes resulting from the Hashin criteria are presented in Figure 4.6, where the σ_{11}-σ_{22}, σ_{11}-σ_{12}, σ_{22}-σ_{12}, σ_{22}-σ_{23}, σ_{12}-σ_{13} and σ_{12}-σ_{23} stress spaces are considered.

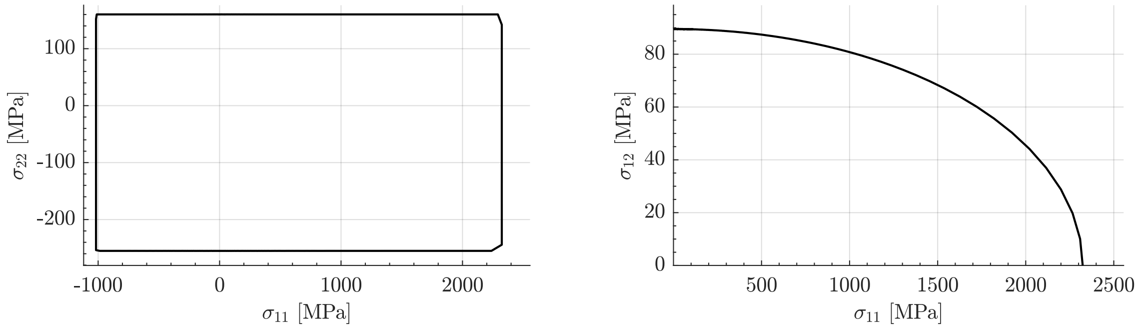

(a) **(b)**

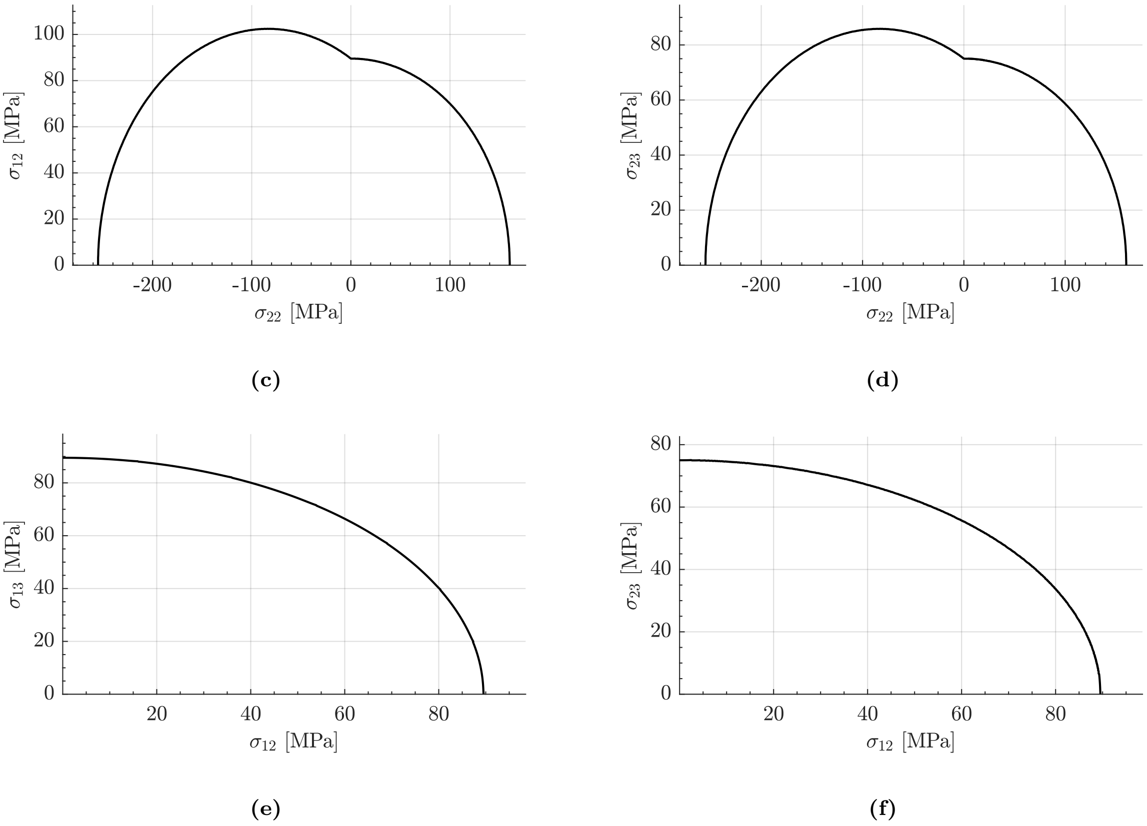

(c) **(d)**

(e) **(f)**

Figure 4.6: Hashin criteria for (a) σ_{11}-σ_{22}, (b) σ_{11}-σ_{12}, (c) σ_{22}-σ_{12}, (d) σ_{22}-σ_{23}, (e) σ_{12}-σ_{13} and (f) σ_{12}-σ_{23} failure envelopes.

4.2.3.3 Three-dimensional Failure Criteria:

Developed by Catalanotti et al. [29] with the purpose of predicting the onset of failure in complex, three dimensional stress states and provide information about the type of failure and the orientation of the fracture plane, this set of criteria can be subdivided in two classes: transverse and longitudinal failure criteria.

Transverse Failure: When a composite is subjected to a stress state such that matrix failure mechanisms arise, the formation of a fracture plane occurs. This surface can be characterized through α, the angle between the fracture plane and the through-thickness direction, as shown in Figure 4.7. The assessment of the matrix's failure index will then be done according to the stresses acting on the fracture plane, which are directly dependent on α.

The fracture plane stress components can be defined as:

$$t_N = \mathbf{t} \cdot \mathbf{n_2} = \sigma_{22}^{\alpha} \qquad t_L = \mathbf{t} \cdot \mathbf{n_1} = \sigma_{23}^{\alpha} \qquad t_T = \mathbf{t} \cdot (\mathbf{n_1} \times \mathbf{n_2}) = \sigma_{21}^{\alpha} \tag{4.24}$$

where $\mathbf{n_1}$ is a unit vector, $\mathbf{n_2}$ is the unit normal vector to the fracture plane and $\mathbf{t}$ is the

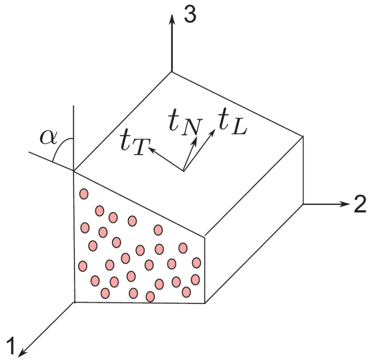

Figure 4.7: Fracture plane and its stress components [29].

stress acting on the fracture plane:

$$\mathbf{n_1} = \{1\ 0\ 0\}^T \qquad \mathbf{n_2} = \{0\ cos(\alpha)\ sin(\alpha)\}^T \qquad \mathbf{t} = \sigma \cdot \mathbf{n_2} \tag{4.25}$$

· **Transverse Tension:** $t_N > 0$

$$\phi_{MT} = \left(\frac{t_N}{S_T^{is}}\right)^2 + \left(\frac{t_N}{S_T^{is}}\right)^2 + \left(\frac{t_L}{S_L^{is}}\right)^2 + \lambda\left(\frac{t_N}{S_T^{is}}\right)\left(\frac{t_L}{S_L^{is}}\right)^2 + \kappa\left(\frac{t_N}{S_T^{is}}\right) \tag{4.26}$$

where ϕ_{MT} is the matrix tension failure index and S_L^{is} and S_T^{is} are the in-situ longitudinal and transverse shear strengths, respectively. The coefficients κ and λ are obtained by imposing $\phi_{MT} = 1$ when $t_N = Y_T^{is}$, being defined as:

$$\kappa = \frac{S_T^{is2} - Y_T^{is2}}{S_T^{is2} Y_T^{is2}} \qquad \lambda = 2\eta_L S_T^{is}/S_L^{is} - \kappa \tag{4.27}$$

· **Transverse Compression:** $t_N < 0$

In the case of transverse compression, Catalanotti et al. provide an extension of Puck's criterion in order to account for in-situ effects on the ply strength. The formulation is established as:

$$\phi_{MC} = \left(\frac{t_L}{S_L^{is} - \eta_L t_N}\right)^2 + \left(\frac{t_T}{S_T^{is} - \eta_T t_N}\right)^2 \tag{4.28}$$

where ϕ_{MC} is the matrix compression failure index and η_L and η_T are the longitudinal and transverse friction coefficients, respectively.

Longitudinal Failure: Longitudinally aligned loading leads to two extremes of complexity in terms of failure assessment. On the one hand, tensile failure is simply assessed by the previously introduced maximum strain criterion, on the other, the compressive stress state leads to complex failure mechanisms, as shown in Section 3.3.2, with Catalanotti's criteria considering the occurrence of fiber kinking failure mode.

· **Longitudinal Tension:** $\sigma_{11} > 0$

In this case, the maximum strain criterion is used:

$$\phi_{LT} = \frac{\varepsilon_{11}}{\varepsilon_{11}^{T}} \tag{4.29}$$

· **Longitudinal Compression:** $\sigma_{11} \leq 0$

This stress state leads to the emergence of fiber kinking which ultimately results in matrix failure in the fiber misalignment frame of reference. In this scenario, three coordinate systems, shown in Figure 4.8 will be at play:

1. 123 is the conventional material reference axis, with 1 being aligned with the fiber direction, 2 the transverse and 3 the out-of-plane directions.
2. $1^{\theta}2^{\theta}3^{\theta}$ is the coordinate system associated with the fiber kinking plane, defined by a rotation of 123 around the axis 1 by the angle θ.
3. $1^{\phi}2^{\phi}3^{\phi}$ is the frame of reference linked to the kink-bands' orientation, associated to a rotation of $1^{\theta}2^{\theta}3^{\theta}$ around the axis 3^{θ} by the ϕ.

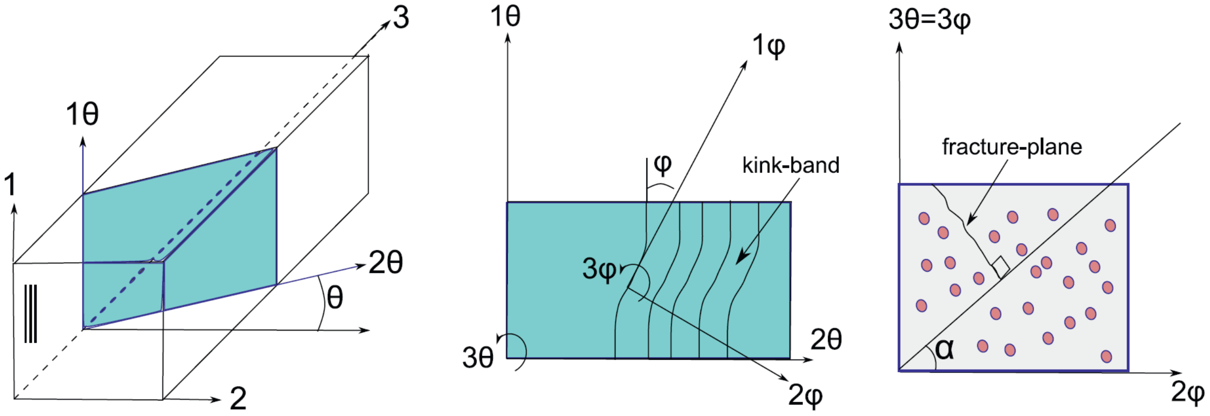

Figure 4.8: Coordinate systems associated with fiber kinking [29].

The fracture plane then forms with respect to the $1^{\phi}2^{\phi}3^{\phi}$ frame of reference, being identified by the angle α, in the same manner as the transverse failure scenario. The angle θ that defines the kinking plane can be obtained as:

$$\theta = \frac{1}{2}\arctan\left(\frac{\sigma_{23}}{\sigma_{22} - \sigma_{33}}\right) \tag{4.30}$$

and the rotation of the stress tensor to that coordinate system is done such that $\boldsymbol{\sigma}^{\theta} = \mathbf{T}^{\theta} \cdot \boldsymbol{\sigma}$ with the help of the 3D stress transformation tensor introduced by Lekhnitskiĭ [40], defined in Equation 4.31.

$$\mathbf{T}^{\theta} = \begin{bmatrix} 1 & 0 & 0 & 0 & 0 & 0 \\ 0 & \cos^2\theta & \sin^2\theta & 0 & 0 & 2\cos\theta\sin\theta \\ 0 & \sin^2\theta & \cos^2\theta & 0 & 0 & -2\cos\theta\sin\theta \\ 0 & 0 & 0 & \cos\theta & \sin\theta & 0 \\ 0 & 0 & 0 & -\sin\theta & \cos\theta & 0 \\ 0 & -\cos\theta\sin\theta & \cos\theta\sin\theta & 0 & 0 & \cos^2\theta - \sin^2\theta \end{bmatrix} \tag{4.31}$$

Likewise, the stress can then be rotated to the misalignment plane, characterized by the angle φ, where the stress tensor is defined as $\boldsymbol{\sigma}^{\varphi} = \mathbf{T}^{\varphi} \cdot \boldsymbol{\sigma}^{\theta}$ and $\mathbf{T}^{\varphi}$ is:

$$\mathbf{T}^{\varphi} = \begin{bmatrix} \cos^2\varphi & \sin^2\varphi & 0 & 2\cos\varphi\sin\varphi & 0 & 0 \\ \sin^2\varphi & \cos^2\varphi & 0 & -2\cos\varphi\sin\varphi & 0 & 0 \\ 0 & 0 & 1 & 0 & 0 & 0 \\ -\cos\varphi\sin\varphi & \cos\varphi\sin\varphi & 0 & \cos^2\varphi - \sin^2\varphi & 0 & 0 \\ 0 & 0 & 0 & 0 & \cos\varphi & -\sin\varphi \\ 0 & 0 & 0 & 0 & \sin\varphi & \cos\varphi \end{bmatrix} \tag{4.32}$$

where both of these tensors are used in conjunction with a stress tensor of the form:

$$\boldsymbol{\sigma} = \{\sigma_{11}, \sigma_{22}, \sigma_{33}, \sigma_{12}, \sigma_{13}, \sigma_{23}\}^T \tag{4.33}$$

Once the stress tensor in the misalignment frame is obtained, the same process as the one described for the occurrence of transverse failure takes place, albeit with the fracture plane stress components being defined in relation to the misalignment coordinate system. Thus, if $t_N^{\phi} < 0$:

$$\phi_{KMC} = \left(\frac{t_L^{\varphi}}{S_L^{is} - \eta_L t_N^{\varphi}}\right)^2 + \left(\frac{t_T^{\varphi}}{S_T^{is} - \eta_T t_N^{\varphi}}\right)^2 \tag{4.34}$$

and if $t_N^{\varphi} \geq 0$, the failure index is given by:

$$\phi_{KMT} = \left(\frac{t_N^{\varphi}}{S_T^{is}}\right)^2 + \left(\frac{t_N^{\varphi}}{S_T^{is}}\right)^2 + \left(\frac{t_L^{\varphi}}{S_L^{is}}\right)^2 + \lambda\left(\frac{t_N^{\varphi}}{S_T^{is}}\right)\left(\frac{t_L^{\varphi}}{S_L^{is}}\right)^2 + \kappa\left(\frac{t_N^{\varphi}}{S_T^{is}}\right) \tag{4.35}$$

Finally, the failure index for fiber kinking is defined as the maximum of the tensile and compressive fiber kinking indices: $\phi_K = \max(\max(\phi_{KMT}), \max(\phi_{KMC}))$

Failure Envelope: The limit stress configurations resulting from the application of the Catalanotti three-dimensional failure criteria are shown in Figure 4.9, which considers the σ_{11}-σ_{22}, σ_{11}-σ_{12}, σ_{11}-σ_{23}, σ_{22}-σ_{12}, σ_{22}-σ_{13}, σ_{22}-σ_{23}, σ_{12}-σ_{13} and σ_{12}-σ_{23} stress spaces.

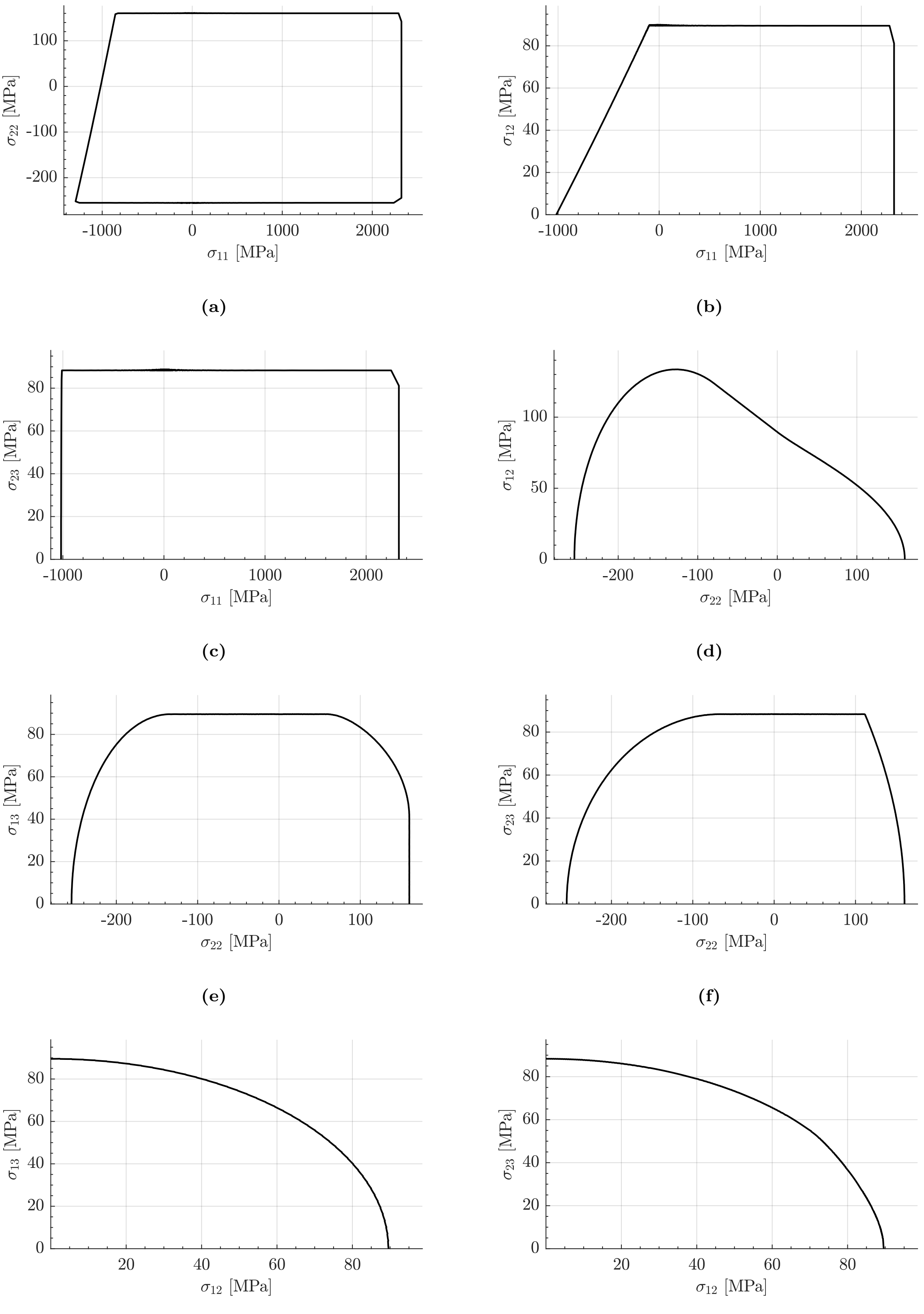

(a) **(b)**

(c) **(d)**

(e) **(f)**

(g) **(h)**

Figure 4.9: Catalanotti criteria for (a) σ_{11}-σ_{22} (b) σ_{11}-σ_{12} (c) σ_{11}-σ_{23} (d) σ_{22}-σ_{12} (e) σ_{22}-σ_{13} (f) σ_{22}-σ_{23} (g) σ_{12}-σ_{13} (h) σ_{12}-σ_{23} failure envelopes.

4.2.4 Comparison

After presenting some of the main formulations used in the literature to determine failure, it is relevant to analyse their effectiveness at conveying this state. Thus, experimental results were compared with the predictions made by the failure criteria for the AS4/55A and IM7/8552 carbon fiber composites in Figures 4.10 and 4.11, respectively.

Taking these (and other comparisons made in the literature which consider other materials [29]) into consideration, it is possible to determine that Catalanotti's three dimensional failure criteria presents the best correlation with what occurs experimentally.

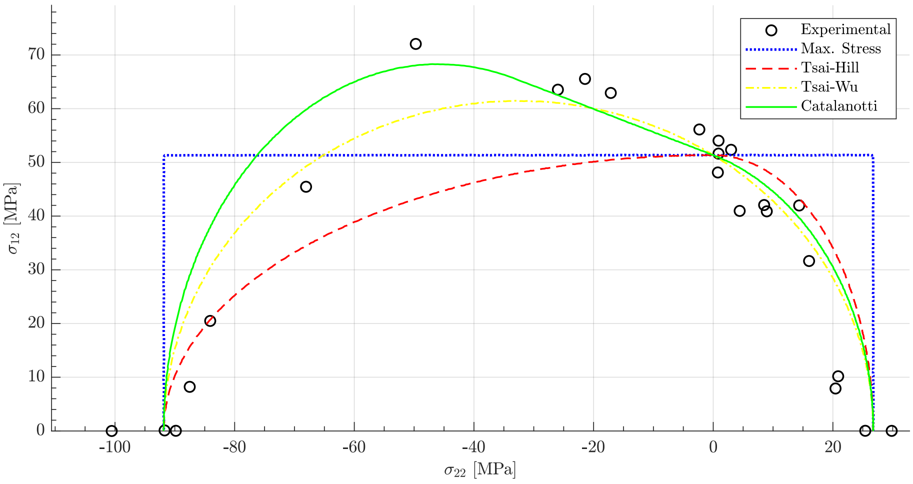

Figure 4.10: Failure envelopes of the AS4/55A UD carbon epoxy laminate obtained by various theories, with experimental results from Sun [41] and Swanson et al. [42]

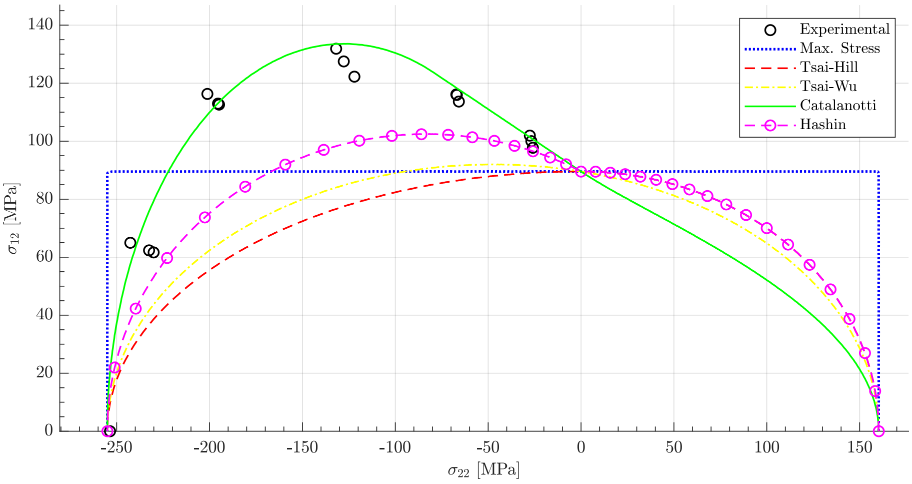

Figure 4.11: Failure envelopes of the IM7/8552 UD carbon epoxy laminate obtained by various theories, with experimental results from Koerber et al. [30]

4.3 Continuum Damage Mechanics

The continuum damage mechanics (CDM) approach, originally developed by Kachanov and Rabotnov [43, 44, 45] through the area reduction method, and later improved by Lemaitre and Chaboche [46, 47] considers the effect of cracks in the structure by degrading its properties, such as moduli and strength, homogenizing the effect of the localized damage in a continuum. A mesoscale approach, through the lens of CDM, differentiates between the plies of a composite material and the interface between those plies. The intraply behaviour of a unidirectional lamina is orthotropic and, in effect, the longitudinal axis corresponds to the fiber and the transverse axis corresponds to the matrix. Hence, any degradation of these constituents will influence the properties of the ply in that direction. Through CDM, by applying degradation laws to the constituents and orienting them in the correct disposition, it is possible to express the behaviour of the material in a realistic manner.

In order to account for the complex mechanical behaviour of composites brought about by the deterioration of each phase when subjected to loading, as well as the inter-phase interactions, it is necessary to establish damage models which account for the decay of the mechanical properties according to the stress state. The continuum damage mechanics approach represents the damage state of the material through damage variables d_i.

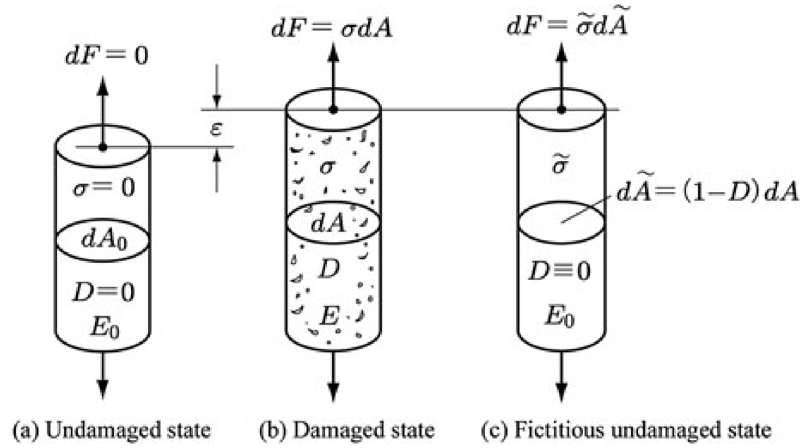

Figure 4.12: Deformation and damage of a bar under tensile load [48].

These damage variables are directly related to the accumulation of cracks in the material and the corresponding reduction of load carrying effective area [45]. Considering the example in Figure 4.12, the transition of the cross-sectional effective area from A_0 to $\tilde{A}$ as damage progresses leads to a proportional increase in effective stress $\tilde{\sigma}$, given by:

$$\tilde{\sigma} = \frac{dF}{d\tilde{A}} = \frac{\sigma}{1 - D} \tag{4.36}$$

Applying the elastic law under uniaxial loading and considering strain equivalence between the damaged and fictitious undamaged states of Figure 4.12:

$$\tilde{\sigma} = E_0 \varepsilon^e \leftrightarrow \sigma = E_0(1 - D)\varepsilon^e = E_d \varepsilon^e \tag{4.37}$$

where E_d is expressed as the damaged material modulus. Expanding this concept to the three-dimensional domain gives rise to the $\boldsymbol{d}$ damage tensor, acting on each stress component as:

$$\tilde{\boldsymbol{\sigma}} = \boldsymbol{\sigma} : \boldsymbol{d}^{-1} \tag{4.38}$$

leading to an elastic constitutive relation given through damaged compliance matrix in the form of:

$$\begin{Bmatrix} \varepsilon_{11} \\ \varepsilon_{22} \\ \varepsilon_{33} \\ \gamma_{12} \\ \gamma_{23} \\ \gamma_{13} \end{Bmatrix} = \begin{bmatrix} \frac{1}{E_1(1-d_1)} & -\frac{\nu_{21}}{E_2} & -\frac{\nu_{31}}{E_3} & 0 & 0 & 0 \\ -\frac{\nu_{12}}{E_1} & \frac{1}{E_2(1-d_2)} & -\frac{\nu_{32}}{E_3} & 0 & 0 & 0 \\ -\frac{\nu_{13}}{E_1} & -\frac{\nu_{23}}{E_2} & \frac{1}{E_3(1-d_3)} & 0 & 0 & 0 \\ 0 & 0 & 0 & \frac{1}{G_{12}(1-d_4)} & 0 & 0 \\ 0 & 0 & 0 & 0 & \frac{1}{G_{23}(1-d_5)} & 0 \\ 0 & 0 & 0 & 0 & 0 & \frac{1}{G_{13}(1-d_6)} \end{bmatrix} \begin{Bmatrix} \sigma_{11} \\ \sigma_{22} \\ \sigma_{33} \\ \sigma_{12} \\ \sigma_{23} \\ \sigma_{13} \end{Bmatrix} \tag{4.39}$$

where the non-diagonal components are independent of damage, given that the Poisson ratio ν_{ij} is considered to receive the same damage as the moduli E_i and G_{ij} [49], assuring a symmetrical compliance matrix.

$$\frac{\nu_{ij}\,(1-d_i)}{E_i\,(1-d_i)} = \frac{\nu_{ij}}{E_i} \quad (i, j = 1, 2, 3 \quad i \neq j) \tag{4.40}$$

4.4 Plasticity

Another phenomenon that can be observed in the material response of composite laminates is pseudo-plasticity, as illustrated in Figure 4.13, which is induced by the plasticity of the matrix and fiber matrix slippage [50]. Thermoplastic matrix composites have higher susceptibility to the occurrence of plastic and pseudo-plastic deformation phenomena, especially on transverse and shear load configurations. This is due to the more ductile nature of their matrix, when compared to thermoset based composites.

In more general terms, the theory of plasticity aims to characterize the plastic, i.e. permanent deformation of materials after they have been subjected to load configurations that cause the stress levels to surpass the elastic, or yield, limit of the material. It can be differentiated into rate-dependent and rate-independent plasticity. That is, whether or not the timescale and sequence of events influence the material behaviour. Only rate-independent plasticity will be discussed, being most suitable for the study of quasi-static loading regimes.

The fundamental aspect of plasticity is the existence of two domains, one elastic and another plastic, divided by the yield stress σ_y. Once the stress increases beyond that limit, plastic flow occurs whereby the increase of plastic strain ε^p takes place. Furthermore, an effect designated as hardening is commonly found accompanying plasticity. It is given as the evolution of the yield stress itself as a function of the plastic strain, which can be seen occurring in the shear stress strain curves of Figure 4.13.

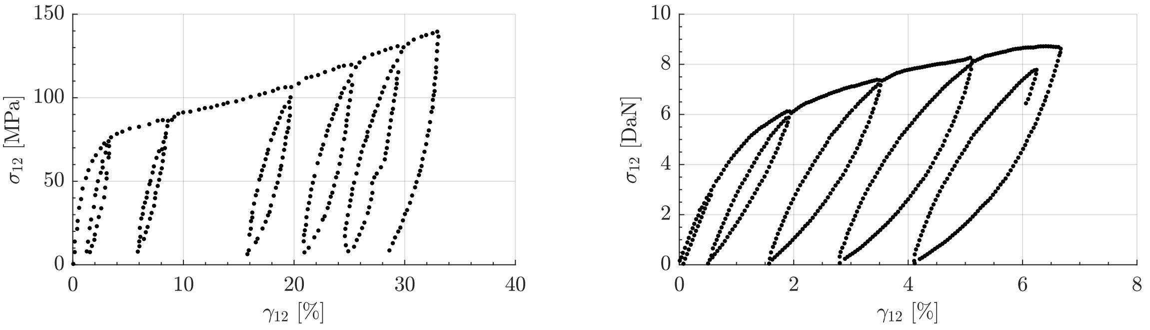

(a) **(b)**

Figure 4.13: Shear stress strain curves for (a) AS4/PEKK thermoplastic and (b) T300/914 thermoset matrix composites, with plastic deformation development. Adapted from [51] and [52], respectively.

In order to understand the fundamental principles and inner workings of the theory of plasticity, a simple one-dimensional elasto-plastic constitutive model, upon which the plasticity model implemented in this dissertation is based, will be described. The stress strain curve resultant from this model is illustrated in Figure 4.14.

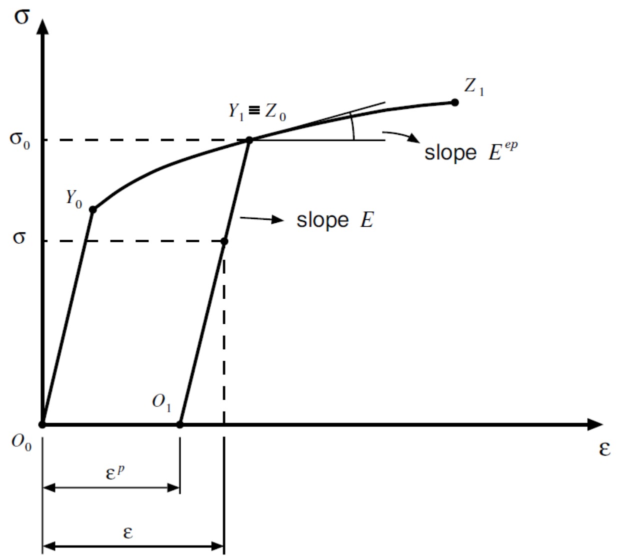

Figure 4.14: Model curve of uniaxial tension experiment with the occurrence of plasticity [53].

Elasto-plastic decompositon of the axial strain

$$\varepsilon = \varepsilon^e + \varepsilon^p \tag{4.41}$$

The presence of the elastic and plastic domains gives rise to their associated strains, one of which, ε^e, is fully reversible and the other, ε^p, is permanent. This is especially apparent by observing the point O_1 of Figure 4.14 which despite having no acting stress, presents deformation equal to that sustained in the plastic domain.

Elastic uniaxial constitutive law

$$\sigma = E\varepsilon^e \tag{4.42}$$

The stress is therefore defined, in the elastic domain, as function of the elastic modulus E and the elastic strain ε^e.

Yield function and criterion

$$F_p(\sigma, \sigma_y) = \sigma - \sigma_y \tag{4.43}$$

As stated before, the yield strength limits the elastic stress region. Therefore, the set of stresses σ that satisfy $F_p < 0$ are in that same domain. If, however, the stress level increases such that that condition is not verified, it must only lie in the yield limit, with no stress level being permitted to exceed σ_y. Hence, the yield function is such that:

$$F_p(\sigma, \sigma_y) \leq 0 \tag{4.44}$$

Plastic flow rule When $F_p = 0$, either loading continues, plastic deformation occurs, and the plastic strain rate $\dot{\varepsilon}^p$ is not null; or elastic unloading takes place, in which case $\dot{\varepsilon}^p = 0$. Considering the case of plastic straining:

$$\dot{\varepsilon}^p = \dot{\lambda}\frac{\partial F_p}{\partial \sigma} \tag{4.45}$$

where $\dot{\lambda}$ is the plastic multiplier, a non-negative scalar which also acts as a consistency parameter [54], and $\frac{\partial F_p}{\partial \sigma}$ is the plastic flow vector, stating the direction of flow in the strain space, as illustrated in Figure 4.15b. Given that the plastic rate is null in the elastic domain:

$$F_p < 0 \Rightarrow \dot{\lambda} = 0 \Rightarrow \dot{\varepsilon}^p \tag{4.46}$$

Hence, the Karush-Kuhn-Tucker conditions for the elasto-plastic model are defined as a consequence of Equations 4.44, 4.46 and the non-negativity of $\dot{\lambda}$:

$$F_p(\sigma, \sigma_y) \leq 0 \ \wedge \ \dot{\lambda} \geq 0 \ \wedge \ F_p\dot{\lambda} = 0 \tag{4.47}$$

Hardening The evolution of the yield stress as plastic strain increases is a clear indicator that hardening is occurring. It can be included in the mathematical model by stating that σ_y is defined as:

$$\sigma_y = \sigma_y(\tilde{\varepsilon}^p) \tag{4.48}$$

where $\tilde{\varepsilon}^p = \int_0^t |\dot{\varepsilon}^p| dt$ and σ_y is a function of the accumulated plastic strain $\tilde{\varepsilon}^p$.

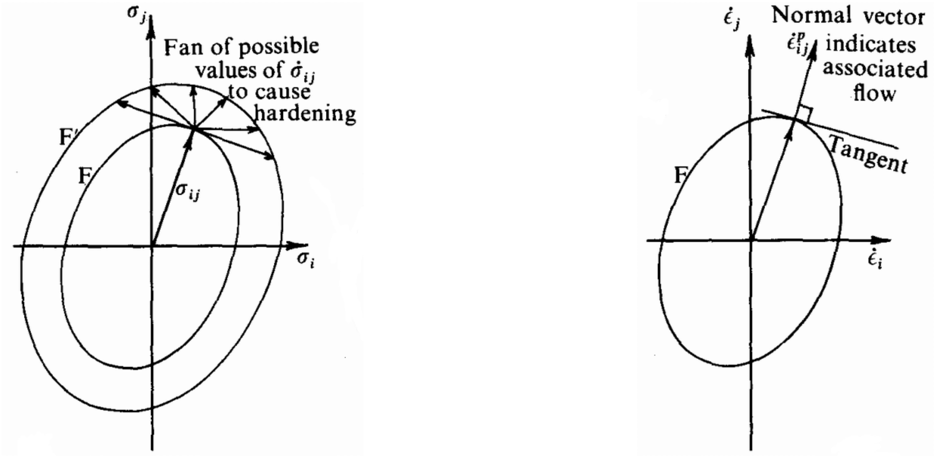

(a) (b)

Figure 4.15: (a) Isotropic hardening and (b) associated plastic flow [55].

Plastic multiplier Finally, the only parameter left unknown is the plastic multiplier $\dot\lambda$. Based on the expressions on 4.47 and given that during plastic yielding $F_p = 0$, it leads that $\dot F_p \dot\lambda = 0$. Hence, since $\dot\lambda \geq 0 \Rightarrow \dot F_p = 0$, given by the following expression:

$$\dot F_p = 0 \Rightarrow \frac{dF_p}{d\sigma}\dot\sigma - \frac{d\sigma_y}{d\tilde\varepsilon^p}\dot{\tilde\varepsilon}^p = 0 \Leftrightarrow \frac{dF_p}{d\sigma}E(\dot\varepsilon - \dot\varepsilon^p) - \frac{d\sigma_y}{d\tilde\varepsilon^p}\dot{\tilde\varepsilon}^p = 0 \tag{4.49}$$

Considering Equation 4.45 and that, from the definition of $\tilde\varepsilon^p$, $\dot{\tilde\varepsilon}^p = |\dot\varepsilon^p|$:

$$\frac{dF_p}{d\sigma}E\left(\dot\varepsilon - \frac{dF_p}{d\sigma}\dot\lambda\right) - \frac{d\sigma_y}{d\tilde\varepsilon^p}\left|\frac{dF_p}{d\sigma}\dot\lambda\right| = 0 \tag{4.50}$$

which, considering the non-negativity of $\dot\lambda$, results in its definition as:

$$\dot\lambda = \frac{\frac{dF_p}{d\sigma}E}{\frac{d\sigma_y}{d\tilde\varepsilon^p} + \left(\frac{dF_p}{d\sigma}\right)^2 E}|\dot\varepsilon| \tag{4.51}$$

Part III

Constitutive Model

Chapter 5

Ply Behaviour

This chapter focuses on establishing a material model for ply behaviour. A continuum damage mechanics framework is implemented via the damage model developed by Ladevèze and Le Dantec [52], introducing damage evolution laws that lead to the prediction of the transverse and shear non-linear response.

Pseudo-plasticity is taken into account by a coupled non-linear hardening formulation, in order to consider the residual deformation observed during transverse and, most notably, shear loading scenarios.

The occurrence of fiber, matrix and fiber kinking failure is determined by the three-dimensional failure criteria developed by Catalanotti et al. [29]. Post-failure behaviour is governed by the evolution of a failure damage parameter d_f such that the energy dissipated in this stage reflects the fracture energy of the failed constituent.

Phenomenae such as the *in situ* effect and fiber rotation are also considered in the described material model.

5.1 Diffuse Damage

The first stage of development of the model focused on appropriately characterizing the non-linear response occurring when composites are solicited in shear and transverse stress configurations, which can be observed in Figure 5.2a and Figure 5.2b, respectively.

For this effect, the introduction of a formulation developed by Hahn and Tsai [56] was first considered. The non-linearity of the shear behaviour is governed by the coefficient β, designated as the shear response factor, which is obtained from experimental data. Validated by Chang et al. [57], this formulation is given as:

$$\gamma_{12} = \frac{1}{G_{12}}\sigma_{12} + \beta\sigma_{12}^3 \Rightarrow \beta = \frac{\gamma_{12} - \frac{\sigma_{12}}{G_{12}}}{\sigma_{12}^3} \tag{5.1}$$

As can be verified in Figure 5.1, this method can be useful to describe the initial stages of the shear stress-strain response, where the operating envelope of most cross-ply laminates is. Accordingly, this approach will be used in Section 5.5 to obtain the *in-situ* properties of embedded plies.

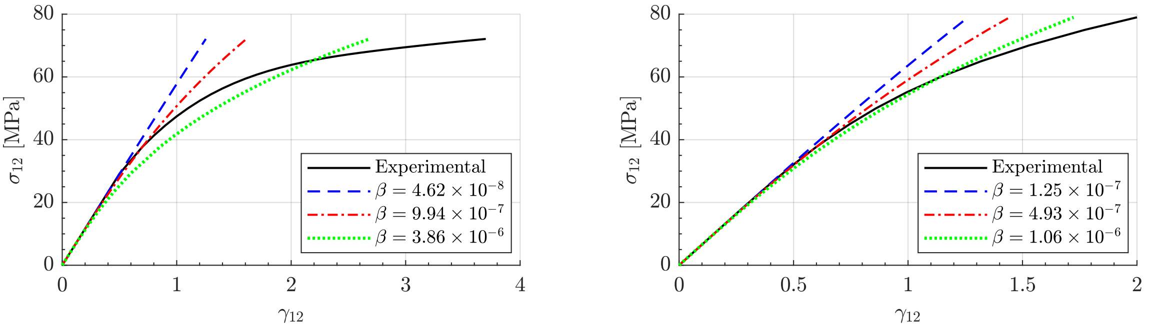

(a) **(b)**

Figure 5.1: Shear response factor approach to describe shear behaviour in (a) AS4/3501-6 and (b) E-Glass/LY556/HT907/DY063 epoxy composites. Experimental data obtained from Soden et al. [58].

However, this method does not assess the non-linear transverse behaviour and is also insufficient to describe the later stages of the shear response, relying on a rough curve fitting approximation that yields inconsistent results, instead of a physical damage-based framework. Therefore, a formulation based on the work of Ladevèze and Le Dantec [52] and Lachaud [59] was implemented.

In this approach, continuum damage mechanics are employed to describe matrix micro-cracking and fiber-matrix debonding damage modes, differentiating between tension and compression. A plane stress state is assumed in the original formulation [52]. The ply complementary free energy density is first characterized as:

$$E_D = \frac{1}{2}\left[\frac{\sigma_{11}^2}{E_1^0} - \frac{2\nu_{12}^0}{E_1^0}\sigma_{11}\sigma_{22} + \frac{\langle\sigma_{22}\rangle_+^2}{E_2^0(1-d_m)} + \frac{\langle\sigma_{22}\rangle_-^2}{E_2^0} + \frac{\sigma_{12}^2}{2G_{12}^0(1-d_{fm})}\right] \tag{5.2}$$

where d_{fm} and d_m are scalar damage variables for fiber-matrix debonding and matrix microcracking, respectively, and $\langle\bullet\rangle$ are the Macaulay brackets, indicating that, for any real number x, $\langle x\rangle_+ = (x+|x|)/2$ or $\langle x\rangle_- = (x-|x|)/2$ [54]. Crack closure under load reversal is taken into account by nullifying the transverse damage variable when under compressive stress. The shear damage variable is not considered to be affected by the crack closure effect since transverse cracks do not close under shear stresses [60]. Hence, the damaged elastic law is given by:

$$\boldsymbol{\varepsilon}^{\mathrm{e}} = \mathbf{K}^{-1}\boldsymbol{\sigma} \Leftrightarrow \begin{cases} \varepsilon_{11}^{\mathrm{e}} = \frac{\sigma_{11}}{E_1^0} - \frac{v_{12}}{E_1^0}\sigma_{22} \\ \varepsilon_{22}^{\mathrm{e}} = \frac{\langle\sigma_{22}\rangle_+}{E_2^0(1-d_{22})} + \frac{\langle\sigma_{22}\rangle_-}{E_2^0} - \frac{v_{12}^0}{E_1^0}\sigma_{11} \\ \varepsilon_{12}^{\mathrm{e}} = \frac{\sigma_{12}}{2G_{12}^0(1-d_{12})} \end{cases} \tag{5.3}$$

where the damage variables are defined through a damage development law defined as:

$$d = \frac{\langle\underline{Y} - Y_0\rangle_+}{Y_c} \tag{5.4}$$

The components Y_0 and Y_c are the initiation and critical values, respectively, for damage evolution and $\underline{Y}$ is defined as:

$$\underline{Y}(t) = \begin{cases} \sup_{\tau \leq t} \left(\sqrt{Y_{d_m}(\tau)} \right) & \text{, for matrix microcracking.} \\ \sup_{\tau \leq t} \left(\sqrt{Y_{d_{fm}}(\tau) + bY_{d_m}(\tau)} \right) & \text{, for fiber-matrix debonding.} \end{cases} \tag{5.5}$$

Y_d is a property analogous to the energy release rate, in the sense that it governs the development of damage [59]. This thermodynamic variable is linked with the damage variables d_{fm} and d_m through Eq. 5.6 and Eq. 5.7. Regarding b, it is a coupling coefficient between the transverse and shear damage. It corresponds to the ratio between the transverse traction modulus, E_{22}^t and the shear modulus, G_{12}. The term $sup_{\tau \leq t}$ represents the irreversibility of the damage process, whereby $\underline{Y}$ has the maximum value from any previous time τ up until the current time t.

$$\mathrm{Y_{d_m}} = \rho \left.\frac{\partial \varphi}{\partial \mathrm{d}_m}\right|_{\boldsymbol{\sigma}, \mathrm{d}_{fm}} = \left.\frac{\partial \mathrm{E_D}}{\partial \mathrm{d}_m}\right|_{\boldsymbol{\sigma}, \mathrm{d}_{fm}} = \frac{1}{2} \frac{\langle \sigma_{22} \rangle_+^2}{\mathrm{E}_{22}^0 \left(1 - \mathrm{d}_m\right)^2} \tag{5.6}$$

$$\mathrm{Y_{d_{fm}}} = \rho \left.\frac{\partial \varphi}{\partial \mathrm{d}_{fm}}\right|_{\boldsymbol{\sigma}, \mathrm{d}_m} = \left.\frac{\partial \mathrm{E_D}}{\partial \mathrm{d}_{fm}}\right|_{\boldsymbol{\sigma}, \mathrm{d}_m} = \frac{1}{2} \frac{\sigma_{12}^2}{\mathrm{G}_{12}^0 \left(1 - \mathrm{d}_{fm}\right)^2} \tag{5.7}$$

Since the current numerical model is developed for a three dimensional context, it is necessary to expand the ply complementary free energy density given in Equation 5.2 to the following relation:

$$\begin{aligned} E_D = \frac{1}{2} \Bigg[& \frac{\sigma_{11}^2}{E_1^0} + \frac{\langle \sigma_{22} \rangle_+^2}{E_2^0(1-d_m)} + \frac{\langle \sigma_{22} \rangle_-^2}{E_2^0} + \frac{\langle \sigma_{33} \rangle_+^2}{E_3^0(1-d_m)} + \frac{\langle \sigma_{33} \rangle_-^2}{E_3^0} - \\ & \frac{2\nu_{12}^0}{E_1^0}\sigma_{11}\sigma_{22} - \frac{2\nu_{13}^0}{E_1^0}\sigma_{11}\sigma_{33} - \frac{2\nu_{23}^0}{E_2^0}\sigma_{22}\sigma_{33} + \\ & \frac{{\sigma_{12}}^2}{2G_{12}^0(1-d_{fm})} + \frac{{\sigma_{13}}^2}{2G_{13}^0(1-d_{fm})} + \frac{{\sigma_{23}}^2}{2G_{23}^0(1-d_{fm})} \Bigg] \end{aligned} \tag{5.8}$$

with the diffuse damage incurred from matrix damage and fiber-matrix debonding affecting the out-of-plane directions of the laminate.

It is noteworthy to mention that, contrary to this approach, Wang et al. [54] does not include the extension of the damage components to the out-of-plane related directions, continuing to act solely on the transverse and in-plane shear components (Equation 5.9). Both methodologies will be implemented in the computational model, with the possibility of activating one or the other.

$$\begin{aligned} E_D = \frac{1}{2} \Bigg[& \frac{\sigma_{11}^2}{E_1^0} + \frac{\langle \sigma_{22} \rangle_+^2}{E_2^0(1-d_m)} + \frac{\langle \sigma_{22} \rangle_-^2}{E_2^0} + \frac{\sigma_{33}^2}{E_3^0} - \frac{2\nu_{12}^0}{E_1^0}\sigma_{11}\sigma_{22} - \frac{2\nu_{13}^0}{E_1^0}\sigma_{11}\sigma_{33} - \\ & \frac{2\nu_{23}^0}{E_2^0}\sigma_{22}\sigma_{33} + \frac{{\sigma_{12}}^2}{2G_{12}^0(1-d_{fm})} + \frac{{\sigma_{13}}^2}{2G_{13}^0} + \frac{{\sigma_{23}}^2}{2G_{23}^0} \Bigg] \end{aligned} \tag{5.9}$$

Application: In a more practical sense, the damage evolution laws must first be characterized with the help of experimental data. The following scenario exemplifies this procedure for the transverse and shear stress-strain response of the AS4/PEEK composite, obtained as a result of cyclic tensile tests conducted by Lachaud [59] on $(\pm 45)_{2S}$ and $(90)_{16}$ specimens, which can be observed in Figure 5.2.

The emergence and progression of damage can be verified by observing the degradation of the secant stiffness modulus for each loading and unloading cycle. Quantifying this evolution requires measuring it at each inflection point of the cyclic test (slope of the straight line that passes through the last point of cycle i and the first point of cycle $i+1$) and comparing it to the original modulus, measured before the beginning of the non-linear response, in accordance with ASTM D3518 [61].

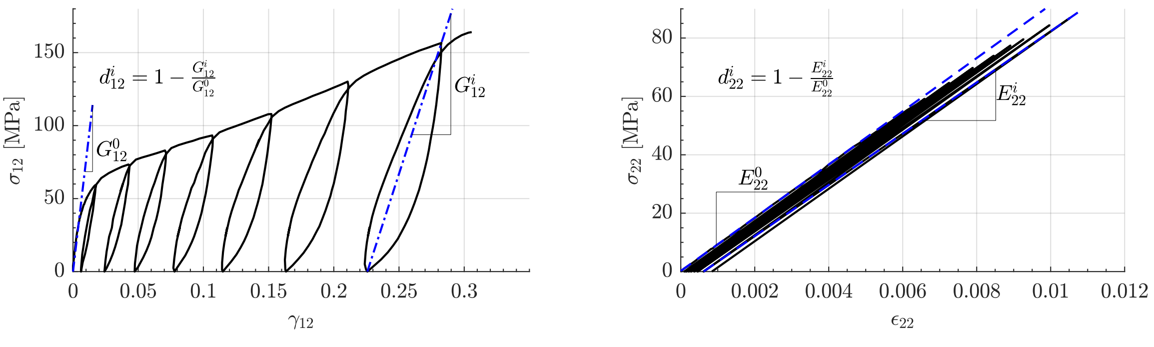

(a) (b)

Figure 5.2: Cyclic stress-strain curves for (a) shear and (b) transverse stress response of AS4/PEEK composite.

The damage parameters d^i_{12} and d^i_{22} can then be measured via the following expressions:

$$d^i_{12} = 1 - \frac{G^i_{12}}{G^0_{12}} \qquad d^i_{22} = 1 - \frac{E^i_{22}}{E^0_{22}} \tag{5.10}$$

Once the damage parameters are obtained, it is possible to plot them against $\underline{Y}$, previously specified in Equation 5.5, and obtain the damage evolution laws through a curve fitting procedure.

Lachaud [59] observed in $(+45)_{2S}$ tests that the transverse component Y_{d_m} is insignificant in relation to the shear component $Y_{d_{fm}}$: $\sigma_{22}^{+45} \approx 0.078\sigma_{12}^{+45}$. Thus, the expression of $\underline{Y}$ for fiber-matrix debonding can be simplified to:

$$\underline{Y}_{12}(d_{12}) = sup\left(\sqrt{\frac{1}{2} G^0_{12} {\gamma^e_{12}}^2}\right) \tag{5.11}$$

eliminating the need to establish the parameter b, present in Equation 5.5.

It is good practice to not limit this analysis to a single test (i.e. just a tensile test of a $(\pm 45)_{2S}$ specimen, for shear response) but also test other layup configurations ($(+45)_{2S}$ and $(\pm 67.5)_{2S}$, for example), since those will provide a corroboration of the results, better understanding of the transverse-shear coupling nature, and damage parameter values for different domains of $\underline{Y}$. In this scenario, as can be observed in Figure 5.3a, damage values resulting from the tensile test of a $(+45)_{2S}$ specimen resulted in better understanding of the early stages of damage, leading to a piecewise damage evolution law.

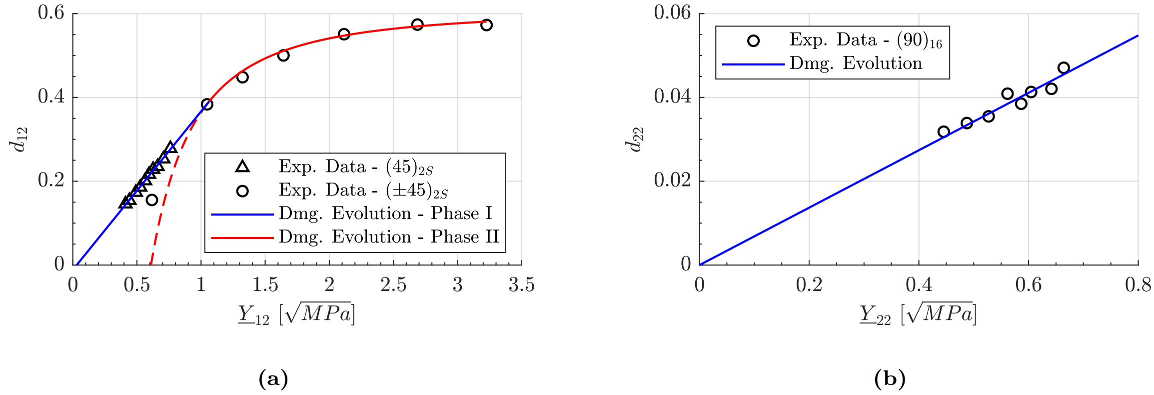

(a) **(b)**

Figure 5.3: Experimental damage behaviour and curve fitting for (a) shear and (b) transverse response of AS4/PEEK composite.

The shear damage evolution is therefore characterized on a first phase by a linear law, transitioning soon after to a power law type progression, given by Equation 5.12.

$$d_{fm} = d_{12} = \begin{cases} 0 & , \text{if } 0 \leq \underline{Y}_{12} < \underline{Y}_{12}^{0} \\ 0.3780\underline{Y}_{12} - 0.0114 & , \text{if } \underline{Y}_{12}^{0} \leq \underline{Y}_{12} < \underline{Y}_{12}^{trans} \\ 0.6094 - 0.245\underline{Y}_{12}^{\;-1.84} & , \text{if } \underline{Y}_{12}^{trans} \leq \underline{Y}_{12} < \underline{Y}_{12}^{c} \end{cases} \tag{5.12}$$

Regarding transverse damage, it behaves as shown in Figure 5.3b, leading to a linear damage evolution law, specified in Equation 5.13.

$$d_m = d_{22} = 0.0685\underline{Y}_{22} \tag{5.13}$$

Once the damage components have been identified, they are considered in the stiffness matrix originating the damaged stiffness matrix $\boldsymbol{C}_d$, as shown in Equation 5.14.

$$\boldsymbol{C}_d = \begin{bmatrix} C_{11} & C_{12} & C_{13} & 0 & 0 & 0 \\ C_{21} & C_{22}(1-d_m) & C_{23} & 0 & 0 & 0 \\ C_{31} & C_{32} & C_{33}(1-d_m) & 0 & 0 & 0 \\ 0 & 0 & 0 & C_{44}(1-d_{fm}) & 0 & 0 \\ 0 & 0 & 0 & 0 & C_{55}(1-d_{fm}) & 0 \\ 0 & 0 & 0 & 0 & 0 & C_{66}(1-d_{fm}) \end{bmatrix} \tag{5.14}$$

The diffuse damage calculation process in a computational environment can thus be described through Algorithm 1.

Algorithm 1 Diffuse damage evolution

```
Require: $E_{22}$, $G_{12}$, $\nu_{12}$, $\nu_{21}$, $\varepsilon^c_{11}$, $\varepsilon^c_{22}$, $\gamma^c_{12}$
Ensure: Matrix failure has not occurred.
  $\underline{Y}^c_{22} \leftarrow \sqrt{\frac{1}{2}E_{22}\frac{1+\nu_{12}}{1-\nu_{12}\nu_{21}}(\varepsilon^c_{11}+\varepsilon^c_{22})^2}$
  $\underline{Y}^c_{12} \leftarrow \sqrt{\frac{1}{2}G_{12}{\gamma^c_{12}}^2}$
  $\underline{Y}_{22} \leftarrow \sqrt{\frac{1}{2}E_{22}\frac{1+\nu_{12}}{1-\nu_{12}\nu_{21}}\langle\varepsilon^e_{11}+\varepsilon^e_{22}\rangle^2_+}$
  $\underline{Y}_{12} \leftarrow \sqrt{\frac{1}{2}G_{12}{\gamma^e_{12}}^2}$
  if $\underline{Y}^0_{ij} \leq \underline{Y}_{ij} < \underline{Y}^c_{ij}$ then
    $d_{ij} \leftarrow f(\underline{Y}_{ij})$
  end if
```

5.2 Plasticity

As discussed in Section 4.4 and observed in Figure 5.2, pseudo-plastic phenomena take place in fiber reinforced composites. This concept will be implemented in the current numerical model through an elasto-plastic approach with non-linear isotropic hardening, expanding the previously introduced framework to a three-dimensional scenario.

In order to do this, a tensor based formulation was used alongside the free energy potential concept within a thermodynamic framework. The free energy φ is such that:

$$\varphi = \varphi(\boldsymbol{\varepsilon}^{\boldsymbol{e}}, p, \alpha) \tag{5.15}$$

where $\boldsymbol{\varepsilon}^{\boldsymbol{e}}$ is the elastic strain tensor, p is the effective accumulated plastic strain and α is associated to kinematic hardening [50], the latter of which will not be considered in the current approach. The yield function can then be expressed as:

$$F_p(\bar{\boldsymbol{\sigma}}, R) = \sigma^{eq} - R \tag{5.16}$$

where R describes the evolution of the yield surface obtained by:

$$R(p) = \rho\frac{\partial\varphi}{\partial p} \tag{5.17}$$

and σ^{eq} is a Hill-type plastic potential function, independent of the longitudinal effective stress $\bar{\sigma}_{11}$ due to purely elastic behaviour in that direction:

$$\sigma^{eq} = \sqrt{\bar{\sigma}^2_{12} + \bar{\sigma}^2_{13} + \bar{\sigma}^2_{23} + a^2(\bar{\sigma}^2_{22} + \bar{\sigma}^2_{33})} \tag{5.18}$$

where the parameter a^2 describes the relation between plastic deformation formed due to transverse loads compared to shear loads [52], being obtained experimentally and defined through the following relation:

$$a^2 = \frac{\dot{\bar{\varepsilon}}^p_{22}(1-d_{22})^2\sigma_{12}}{2\dot{\bar{\varepsilon}}^p_{12}(1-d_{12})^2\sigma_{22}} \tag{5.19}$$

The use of $\bar{\sigma}_{ij}$ effective stress components in the plastic potential is due to the notion that the internal stress generated under loading is sustained by the undamaged part of the material [54]. As a result, plastic effects only occur in that section and are described in relation to the effective stress $\bar{\boldsymbol{\sigma}}$, obtained through the undamaged stiffness matrix $\boldsymbol{C}_0$ by Equation 5.21. The definition of p also takes into account the effect of damage in the measured plastic strain so that the effective accumulated plastic strain is obtained [59]:

$$p = 2(1-d_{12})\varepsilon^p_{12} \tag{5.20}$$

$$\bar{\boldsymbol{\sigma}} = \boldsymbol{C}_0 : \boldsymbol{\varepsilon}^e \tag{5.21}$$

where the previous considerations for the additive decomposition of the elastic strain tensor remain valid:

$$\boldsymbol{\varepsilon} = \boldsymbol{\varepsilon}^e + \boldsymbol{\varepsilon}^p \;\wedge\; \dot{\boldsymbol{\varepsilon}} = \dot{\boldsymbol{\varepsilon}}^e + \dot{\boldsymbol{\varepsilon}}^p \tag{5.22}$$

The plastic strain rate tensor is expressed as a function of the plastic multiplier and the plastic flow tensor:

$$\dot{\boldsymbol{\varepsilon}}^p = \dot{\lambda}\frac{\partial F_p}{\partial \bar{\boldsymbol{\sigma}}} \tag{5.23}$$

and the rate of the hardening variable p is analogously given by:

$$\dot{p} = -\dot{\lambda}\frac{\partial F_p}{\partial R} \tag{5.24}$$

Considering the Karush-Kuhn-Tucker conditions expressed in Equation 4.47 and the condition that stresses must remain on the yield surface when plastic flow is occurring:

$$\dot{F}_p = 0 \Rightarrow \frac{\partial F_p}{\partial \bar{\boldsymbol{\sigma}}} : \dot{\bar{\boldsymbol{\sigma}}} + \frac{\partial F_p}{\partial R} : \dot{R} = 0 \tag{5.25}$$

where:

$$\begin{cases} \dot{\bar{\boldsymbol{\sigma}}} = \boldsymbol{C}_0 : \dot{\boldsymbol{\varepsilon}}^e = \boldsymbol{C}_0 : (\dot{\boldsymbol{\varepsilon}} - \dot{\boldsymbol{\varepsilon}}^p) = \boldsymbol{C}_0 : (\dot{\boldsymbol{\varepsilon}} - \dot{\lambda}\frac{\partial F_p}{\partial \bar{\boldsymbol{\sigma}}}) \\ \frac{\partial F_p}{\partial R} = -1 \end{cases} \tag{5.26}$$

Using an hardening law of the type $R = Kp \Rightarrow \dot{R} = K\dot{p} = K\dot{\lambda}$, the plastic multiplier can then be expressed by the following relation:

$$\dot{\lambda} = \frac{\frac{\partial F_p}{\partial \bar{\boldsymbol{\sigma}}} : \boldsymbol{C}_0 : \dot{\boldsymbol{\varepsilon}}}{\frac{\partial F_p}{\partial \bar{\boldsymbol{\sigma}}} : \boldsymbol{C}_0 : \frac{\partial F_p}{\partial \bar{\boldsymbol{\sigma}}} + K} \tag{5.27}$$

Special attention must be given to the value of $\dot{\lambda}$ when implementing the model since a negative plastic multiplier would imply plastic unloading from the yield surface, which is not possible [62]. Therefore, if Equation 5.27 results in a negative value, $\dot{\lambda}$ should be assumed null, so that elastic unloading occurs.

Application: Considering once again the behaviour of the AS4/PEEK composite, it is possible to compute the evolution of the effective accumulated plastic strain in relation to the effective stress, thereby obtaining the material specific hardening law. This evaluation is done using data from the $[\pm 45]_{2S}$ tensile test due to its significant plastic behaviour, allowing for better understanding of its development. A necessary step that must be taken before characterizing plasticity is the establishment of the damage evolution law.

$$R_i + R_0 = \sqrt{2\int_0^{\sigma_{12}^{max}} \frac{\sigma_{12}}{(1-d_{12}^i)} d\sigma_{12}} = \frac{\sigma_{12}^i}{1-d_{12}^i} \tag{5.28}$$

$$p_i = \int_0^{(\varepsilon_{12}^p)^i} 2(R_i + R_0)\frac{(1-d_{12}^i)^2}{\sigma_{12}^i} d\varepsilon_{12}^p = 2(1-d_{12}^i)(\varepsilon_{12}^p)^i \tag{5.29}$$

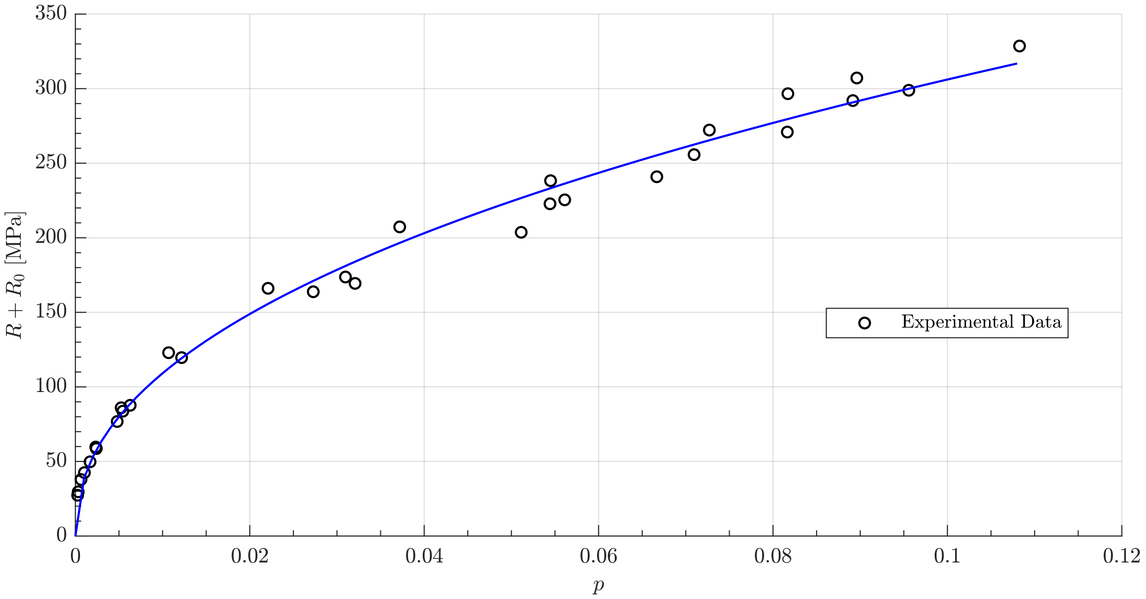

Figure 5.4: Master plasticity curve for AS4/PEEK.

Resulting in a power law of the type $R(p) = K(p+\beta)^\alpha$. The yield function can thus be established:

$$F_p = \sqrt{\bar{\sigma}_{12}^2 + \bar{\sigma}_{13}^2 + \bar{\sigma}_{23}^2 + a^2(\bar{\sigma}_{22}^2 + \bar{\sigma}_{33}^2)} - R(p) \tag{5.30}$$

and the plastic multiplier given by the following relation:

$$\dot{\lambda} = \frac{\frac{\partial F_p}{\partial \bar{\sigma}} : \boldsymbol{C}_0 : \dot{\boldsymbol{\varepsilon}}}{\frac{\partial F_p}{\partial \bar{\sigma}} : \boldsymbol{C}_0 : \frac{\partial F_p}{\partial \bar{\sigma}} + \Lambda}, \text{ where } \Lambda = K\alpha p^{\alpha-1} \tag{5.31}$$

Figure 5.4 illustrates the measured experimental data, along with the derived master plasticity curve previously described. The application of plasticity in a computational environment is given by Algorithm 2.

Algorithm 2 Plasticity algorithm

```
Require: $\bar{\boldsymbol{\sigma}}$, $\boldsymbol{C}_0$, $\boldsymbol{\varepsilon}$, $\dot{\boldsymbol{\varepsilon}}$, $R(p)$, $a^2$
Ensure: Matrix failure has not occurred.
  $F_p \leftarrow \sqrt{\bar{\sigma}_{12}^2 + \bar{\sigma}_{13}^2 + \bar{\sigma}_{23}^2 + a^2(\bar{\sigma}_{22}^2 + \bar{\sigma}_{33}^2)} - R(p)$
  if $F_p = 0$ then
      $\dot{\lambda} \leftarrow \frac{\frac{\partial F_p}{\partial \bar{\boldsymbol{\sigma}}} : \boldsymbol{C}_0 : \dot{\boldsymbol{\varepsilon}}}{\frac{\partial F_p}{\partial \bar{\boldsymbol{\sigma}}} : \boldsymbol{C}_0 : \frac{\partial F_p}{\partial \bar{\boldsymbol{\sigma}}} + \Lambda}$
      if $\dot{\lambda} < 0$ then
          $\dot{\lambda} \leftarrow 0$
      end if
  else
      $\dot{\lambda} \leftarrow 0$
  end if
  $\dot{\boldsymbol{\varepsilon}}^p \leftarrow \dot{\lambda} \frac{\partial F_p}{\partial \bar{\boldsymbol{\sigma}}}$
  $\boldsymbol{\varepsilon}^e \leftarrow \boldsymbol{\varepsilon} - (\boldsymbol{\varepsilon}^p + \dot{\boldsymbol{\varepsilon}}^p)$
```

5.3 Fiber Rotation

An increase of stress can be observed in the later stages of the $[\pm 45]_{2S}$ quasi-static tensile test (Figure 5.5a), where the laminate reaches large strain values. This occurs in agreement with the standard ASTM D3518 [61] and the observations made by Wisnom [63], which warn of significant fiber scissoring effects in this type of test that limit the validity of the shear stress results up to 5% of calculated shear strains values [61]. It is especially relevant to consider fiber rotation in the case of composites with matrices of higher ductility, such as thermoplastics, since this effect is exacerbated in those materials, as it can be verified in Figure 5.5b, where the AS4/PEEK thermoplastic sustained 10° of fiber rotation under shear solicitation.

Moreover, although this event is not expected to affect typical quad-type laminates since the 0° layer fails before the large axial strains necessary for fiber rotation take place, structures designed in accordance with the novel double-double composite layup method will be susceptible to it. Therefore, it was considered relevant to include and model the fiber scissoring phenomenon in the present model.

Three methods of calculating and implementing fiber rotation were considered, with increasing orders of complexity. The first one stems from the general rule of Kellas et al. [64] that states that one degree of fiber rotation occurs for every 2% of axial strain, or 3.5% of shear strain; the second one consists of a geometrically based approach that considers the effect of the principal axial strains, developed by Herakovich et al. [65] and Fuller and Wisnom [66]; the third one, formulated by Eskandari et al. [67] is a tensor based formulation that unpacks the total rotation tensor into rigid rotation and fiber

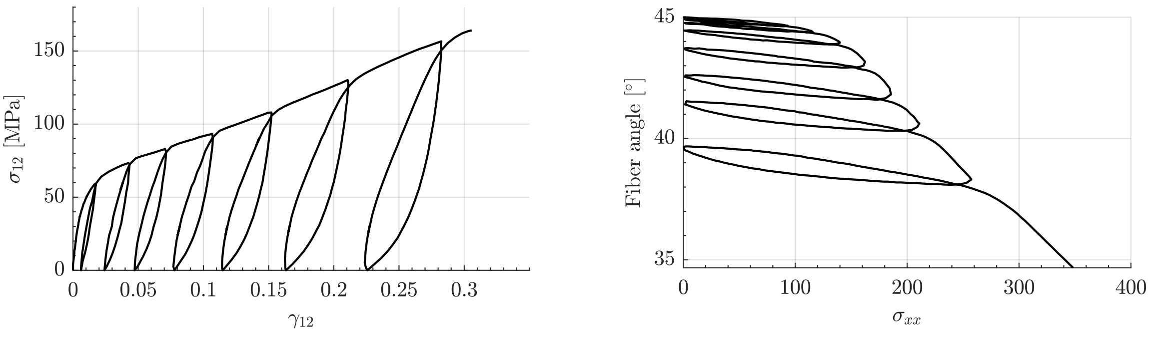

(a) (b)

Figure 5.5: Behaviour of the $[\pm 45]_{2S}$ laminate of AS4/PEEK subjected to a uniaxial tensile load [59]. (a) Shear stress strain response and (b) Variation of fiber angle in relation to the imposed stress.

rotation tensors with the aid of body kinematics, where the latter, expressed as $\mathbf{R}$, is a second order tensor that represents the rotation of the fiber in three dimensions.

Given the high complexity of the tensor based formulation and the overgeneralized approach of the first method, the calculation fiber rotation was based on the approach of Herakovich et al. [65] and Fuller and Wisnom [66], where the fibers are considered to be inextensible, realigning towards the direction of applied stress. The updated fiber angle θ' is thus function of the axial strains ε_{xx} and ε_{yy} is given by Equation 5.32, resulting in the fiber angle evolution illustrated in Figure 5.6.

$$\theta' = \arctan\left(\frac{\tan(\theta) + \varepsilon_{yy}}{1 + \varepsilon_{xx}}\right) \tag{5.32}$$

In the case of large deformations, fiber rotation can significantly influence the shear behaviour of the specimen. In that case, the strain-stress curve does not represent a pure shear stress state since it is based on the assumption of a constant fiber angle. Thus, it is necessary to adapt the curve considering the rotation of the fibers.

Lamination theory allows for the stresses in the principal coordinate system to be described in relation to the longitudinal axial stress σ_{xx} and the orientation angle θ of the laminate in relation to the principal axis [65]:

$$\begin{cases} \sigma_{11} = B\sigma_{xx} \\ \sigma_{22} = (1-B)\sigma_{xx} \\ \sigma_{12} = \frac{-1}{2mn}[B(1-2m^2) + m^2]\sigma_{xx} \end{cases} \tag{5.33}$$

where $m = \cos\theta$, $n = \sin\theta$ and:

$$B = \left[\frac{m^2(2m^2-1) + 4m^2n^2\frac{G_{12}}{E_{22}}\left(\frac{E_{22}}{E_{11}}\nu_{12} + 1\right)}{4m^2n^2\frac{G_{12}}{E_{22}}\left(\frac{E_{22}}{E_{11}} + 2\frac{E_{22}}{E_{11}}\nu_{12} + 1\right) + (2m^2-1)(m^2-n^2)}\right] \tag{5.34}$$

Given that the experimental shear stress was obtained considering $\theta = 45°$ and thus,

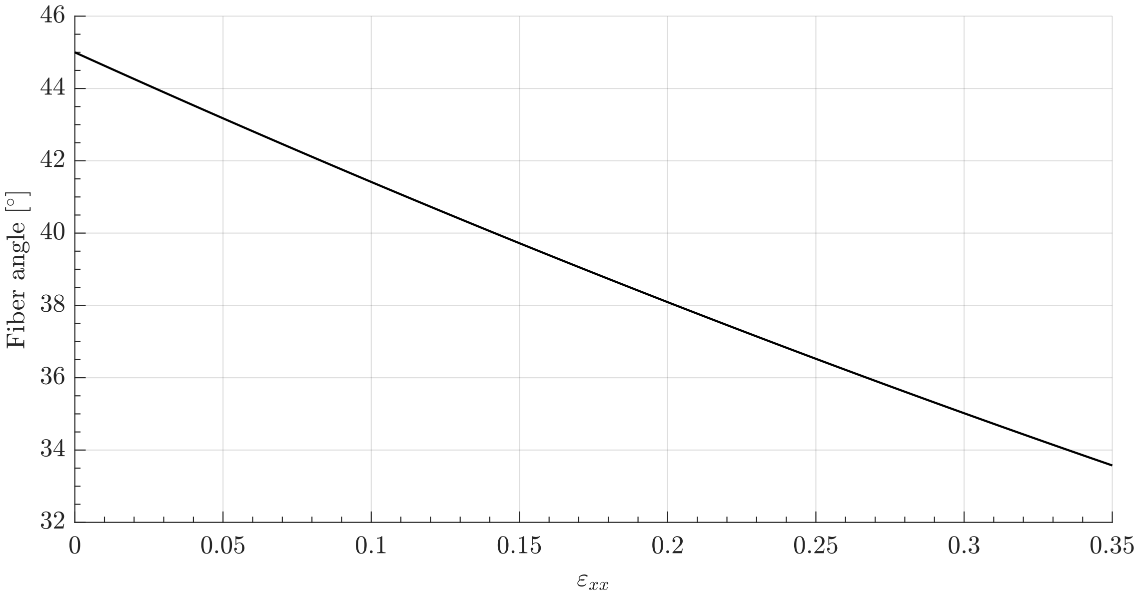

Figure 5.6: Variation of fiber rotation with the increase of axial strain, for an initial ply angle of 45°.

$\sigma_{xx}/2$, and that the fiber angle went down to less than 35° (Figure 5.5b), there is a large discrepancy between the value of pure shear stress and the directly measured one, as can be verified in Figure 5.7.

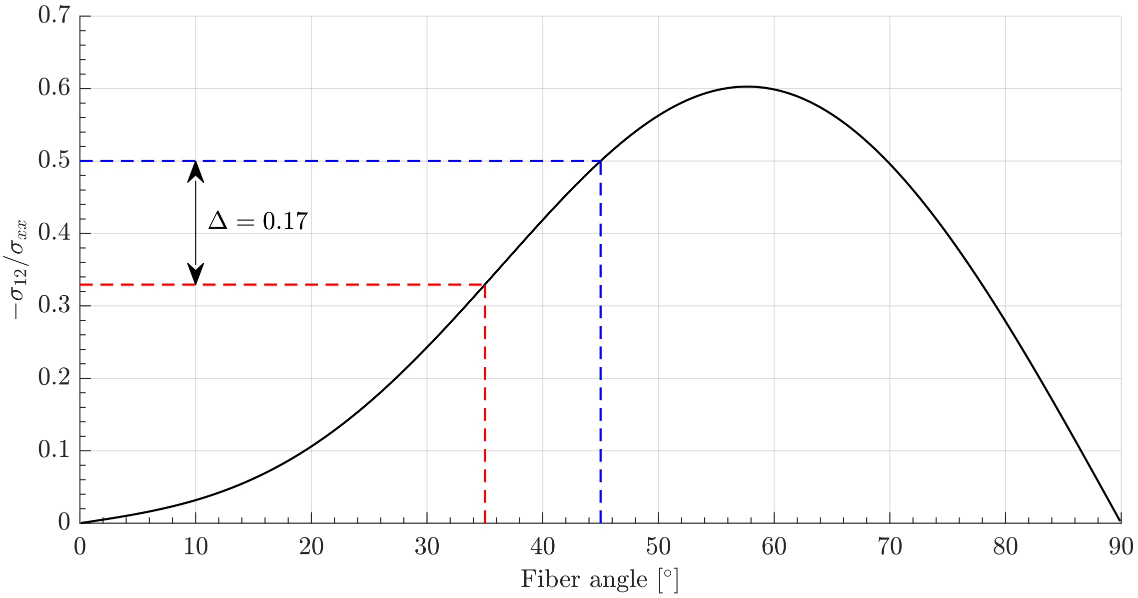

Figure 5.7: Variation of σ_{12}/σ_{xx} in relation to fiber angle.

Since a correction will have to be done to the shear stress-strain curve, it is also necessary to consider the adjustments to the shear strain γ_{12}. This is done through the strain transformation relation:

$$\begin{bmatrix}\varepsilon_{11}\\ \varepsilon_{22}\\ \gamma_{12}\end{bmatrix} = \begin{bmatrix} m^2 & n^2 & mn \\ n^2 & m^2 & -mn \\ -2mn & 2mn & m^2-n^2 \end{bmatrix} \begin{bmatrix}\varepsilon_{xx}\\ \varepsilon_{yy}\\ \gamma_{xy}\end{bmatrix} \Rightarrow \gamma_{12}\big|_{\gamma_{xy}\approx 0} = -2mn(\varepsilon_{xx}-\varepsilon_{yy}) \tag{5.35}$$

The effect of fiber rotation on the material properties is minor [68] and will therefore not be taken into account. Thus, with m and n updating as fibers reorient, the corrected shear stress strain curve is displayed in Figure 5.8.

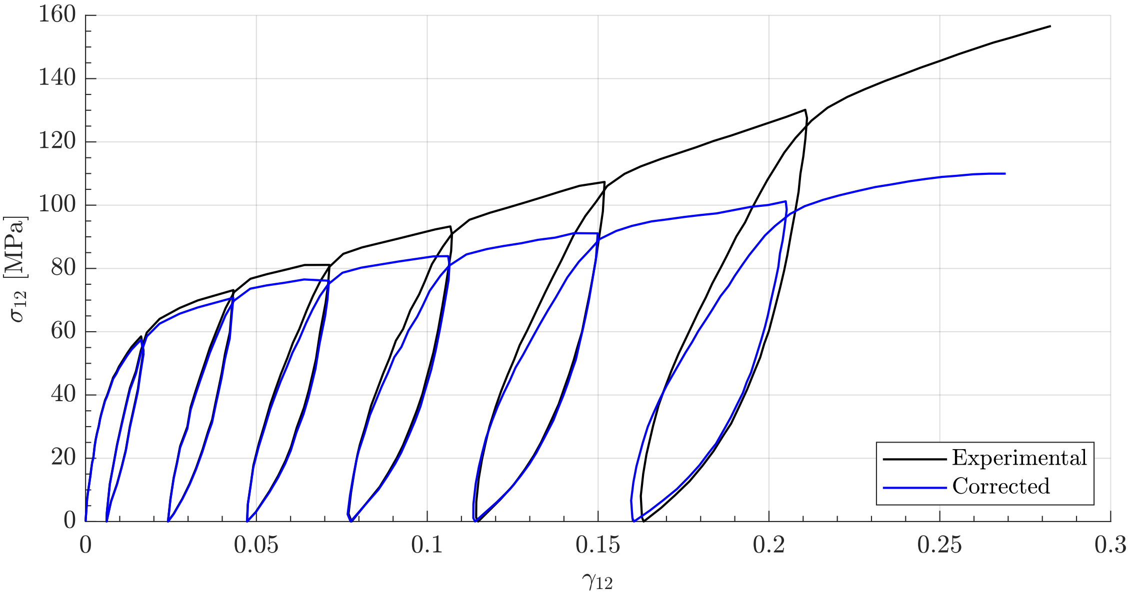

Figure 5.8: Original shear stress strain curve vs corrected pure shear stress strain curve.

Consequently, the diffuse damage curve has to be adapted to what now is the pure shear stress strain curve, resulting in Figure 5.9.

The $(45)_{2S}$ experimental test data was not adjusted given that its domain is only marginally affected by fiber rotation. The corrected shear diffuse damage is therefore given by:

$$d_{fm} = \begin{cases} 0 & \text{, if } 0 \leq \underline{Y}_{12} < \underline{Y}_{12}^{0} \\ 0.3780\underline{Y}_{12} - 0.0114 & \text{, if } \underline{Y}_{12}^{0} \leq \underline{Y}_{12} < \underline{Y}_{12}^{trans} \\ 0.9 - 0.505\underline{Y}_{12}^{-0.765} & \text{, if } \underline{Y}_{12}^{trans} \leq \underline{Y}_{12} < \underline{Y}_{12}^{c} \end{cases} \tag{5.36}$$

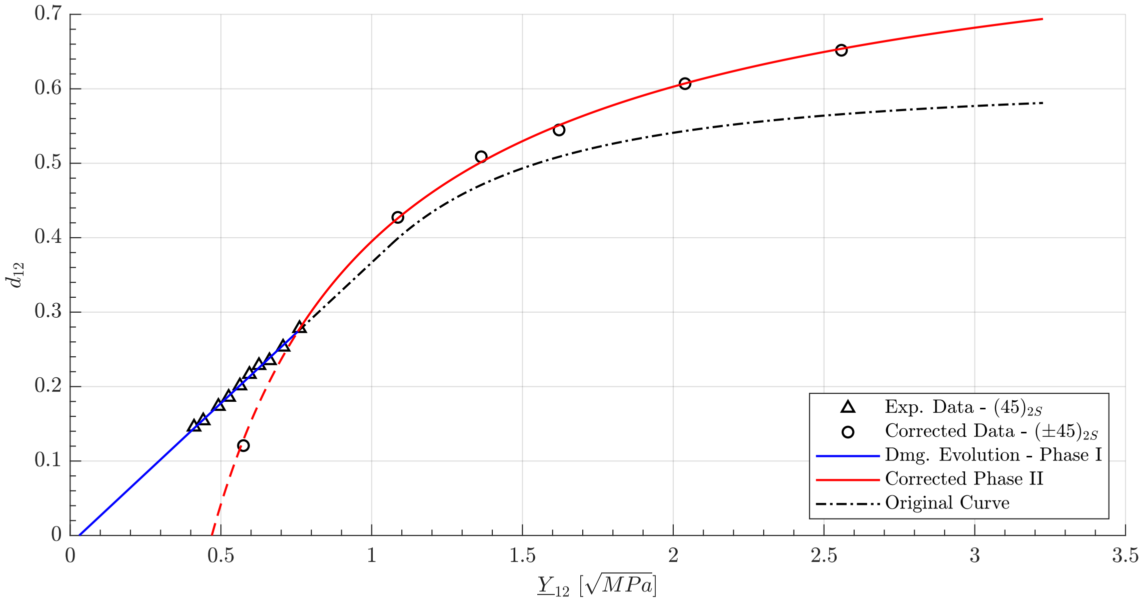

Figure 5.9: Corrected diffuse shear damage master curve.

Application: The insertion of the fiber rotation process in a computational environment can then be summarized by Algorithm 3.

Algorithm 3 Fiber rotation algorithm

```
Require: $0 < \theta_0 < \pi/2$
Ensure: $0 \leq \theta \leq \pi/2$
  $\varepsilon_{xx} \leftarrow \frac{\varepsilon_{11}+\varepsilon_{22}}{2} + \frac{\varepsilon_{11}-\varepsilon_{22}}{2}\cos(-2\theta) + \frac{\gamma_{12}}{2}\sin(-2\theta)$
  $\varepsilon_{yy} \leftarrow \frac{\varepsilon_{11}+\varepsilon_{22}}{2} - \frac{\varepsilon_{11}-\varepsilon_{22}}{2}\cos(-2\theta) - \frac{\gamma_{12}}{2}\sin(-2\theta)$
  $\varepsilon_{xy} \leftarrow -\frac{\varepsilon_{11}-\varepsilon_{22}}{2}\sin(-2\theta) + \frac{\gamma_{12}}{2}\cos(-2\theta)$
  if $\theta > 0$ then
      $\theta' \leftarrow \arctan\left(\frac{tan(\theta_0)+\varepsilon_{yy}}{1+\varepsilon_{xx}}\right)$
  else
      $\theta' \leftarrow -\arctan\left(\frac{tan(\theta_0)+\varepsilon_{yy}}{1+\varepsilon_{xx}}\right)$
  end if
  $\varepsilon'_{11} \leftarrow \frac{\varepsilon_{x}+\varepsilon_{yy}}{2} + \frac{\varepsilon_{xx}-\varepsilon_{yy}}{2}\cos(2\theta') + \varepsilon_{xy}\sin(2\theta')$
  $\varepsilon'_{22} \leftarrow \frac{\varepsilon_{xx}+\varepsilon_{yy}}{2} - \frac{\varepsilon_{xx}-\varepsilon_{yy}}{2}\cos(2\theta') - \varepsilon_{xy}\sin(2\theta')$
  $\gamma'_{12} \leftarrow 2\left(-\frac{\varepsilon_{xx}-\varepsilon_{yy}}{2}\sin(2\theta') + \varepsilon_{xy}\cos(2\theta')\right)$
```

5.4 Failure Criteria

It is now necessary to establish the criteria by which failure is evaluated. Based on the comparison of different formulations done in Section 4.2.4, the three-dimensional failure criteria developed by Catalanotti et al. [29] was deemed the most reliable.

This formulation considers longitudinal and transverse failure modes, in both tension and compression, whose implementation process will be explained next.

5.4.1 Transverse Failure

It was previously introduced that failure in the transverse direction leads to the formation of a fracture plane characterized by the angle between the fracture plane and the through-thickness direction, α. The determination of this angle requires that a maximization problem is solved, that is, finding the angle that maximizes the matrix failure index for a given stress state.

Hence, an iterative process is done by varying α from 0° to 180° and rotating the stress tensor $\boldsymbol{\sigma}$ by that same amount in order to calculate ϕ_{MT} and ϕ_{MC}, the failure indices for matrix tension and compression, respectively.

$$\boldsymbol{\sigma}^{\alpha} = \boldsymbol{T}^{\alpha} \cdot \boldsymbol{\sigma} \tag{5.37}$$

where $\boldsymbol{T}^{\alpha}$ is given by Equation 4.32. And the stresses on the fracture plane are established as:

$$t_N = \sigma_{22}^{\alpha} \qquad t_L = \sigma_{21}^{\alpha} \qquad t_T = \sigma_{23}^{\alpha} \tag{5.38}$$

The fracture angle α then corresponds to the angle that originated the maximum failure index in tension or compression. Experimental results indicate that $\alpha_0 = 53 \pm 2°$ in uniaxial compression [39], decreasing to around 40° as the off-axis compression degree increases, going then suddenly to 0° [60], as illustrated in Figure 5.10 for the specific case of a unidirectional E-glass epoxy lamina. Therefore, if it is necessary to decrease the computational effort of the model, α_0 can be assumed as either 53° in the case of compression or 0° in the case of tensile stress.

Looking now at the failure indices' formulation, it is necessary to determine several material related properties, namely: S_L^{is} *in situ* longitudinal shear strength; S_T^{is} *in situ* transverse shear strength; Y_T^{is} *in situ* transverse tensile strength; Y_C^{is} *in situ* transverse compressive strength; η_L longitudinal friction coefficient and η_T transverse friction coefficient, who are highlighted in the following equations:

$$\begin{cases} \phi_{MC} = \left(\frac{t_L}{\boldsymbol{S_L^{is}} - \boldsymbol{\eta_L} t_N}\right)^2 + \left(\frac{t_T}{\boldsymbol{S_T^{is}} - \boldsymbol{\eta_T} t_N}\right)^2 \\ \phi_{MT} = \left(\frac{t_N}{\boldsymbol{S_T^{is}}}\right)^2 + \left(\frac{t_N}{\boldsymbol{S_T^{is}}}\right)^2 + \left(\frac{t_L}{\boldsymbol{S_L^{is}}}\right)^2 + \lambda \left(\frac{t_N}{\boldsymbol{S_T^{is}}}\right) \left(\frac{t_L}{\boldsymbol{S_L^{is}}}\right)^2 + \kappa \left(\frac{t_N}{\boldsymbol{S_T^{is}}}\right) \\ \kappa = \frac{\boldsymbol{S_T^{is}}^2 - \boldsymbol{Y_T^{is}}^2}{\boldsymbol{S_T^{is}}^2 \boldsymbol{Y_T^{is}}^2} \\ \lambda = 2\boldsymbol{\eta_L} \boldsymbol{S_T^{is}} / \boldsymbol{S_L^{is}} - \kappa \end{cases} \tag{5.39}$$

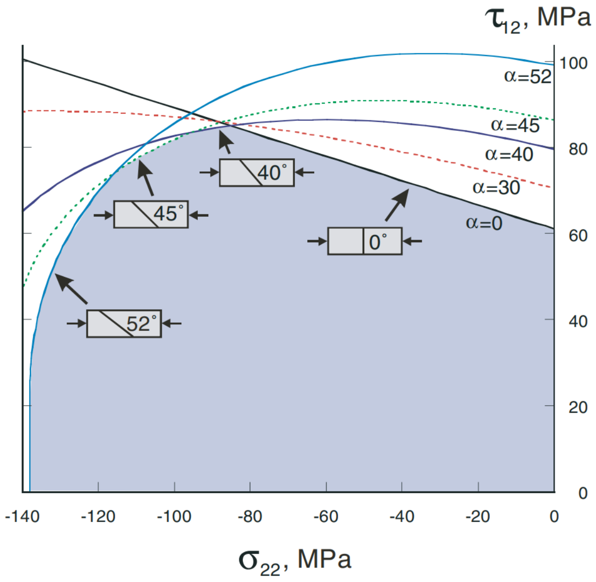

Figure 5.10: Matrix failure envelopes of a unidirectional E-glass epoxy lamina subjected to in-plane transverse compression and shear loading [69].

Of these, S_L^{is} and Y_T^{is} will be determined in the following Section 5.5, which concerns the *in situ* effect, and η_T was obtained by Dávila et al. [69] such that:

$$\eta_T = \frac{-1}{\tan(2\alpha_0)} \tag{5.40}$$

According to Koerber and Camanho [30] η_L can be obtained from a 15° off-axis test (with other bi-axial test data also being suitable). However, if no experimental data is available, η_L can be obtained from the relation between the friction coefficients proposed by Puck and Schürmann [39]:

$$\frac{\eta_L}{\eta_T} = \frac{S_L}{S_T} \Leftrightarrow \eta_L = -\frac{S_L \cos(2\alpha_0)}{Y_C \cos^2(\alpha_0)} \tag{5.41}$$

which then allows for the designation of Y_C^{is} and S_T^{is} by the following relations [29]:

$$Y_C^{is} = -\frac{S_L^{is}(2\cos^2(\alpha_0) - 1)}{\eta_L \cos^2(\alpha_0)} \tag{5.42}$$

$$S_T^{is} = \frac{S_L^{is}(2\sin^2(\alpha_0) - 1)}{2\sqrt{1 - \sin^2(\alpha_0)}\,\sin(\alpha_0)\eta_L} \tag{5.43}$$

An aspect that must be addressed is the fact that establishing these material properties requires the value of α_0 to be known. This property can be obtained from experimental tests but, if it is not defined, a value of 53° is assumed.

5.4.2 Longitudinal Failure

Regarding this type of failure, the main aspect that must be addressed lies within the fiber kinking failure mode and concerns the misalignment frame angle φ which is obtained through a Newton-Raphson procedure [70].

The total misalignment angle φ is understood to be comprised of the initial misalignment angle φ_0 and an angle γ_m originated by the shear stress. Assuming that the initial material is in pristine conditions, $\varphi_0 = 0$ and thus:

$$\varphi = sign(\sigma_{12})\gamma_m \tag{5.44}$$

However, γ_m depends on the shear constitutive law $\tau = f(\gamma_m)$ which, simplifying for a material that possesses linear behaviour in shear leads to:

$$\sigma_{12}^m = \chi\gamma_m \tag{5.45}$$

where χ is expressed as:

$$\chi = \frac{\sin(2\varphi_C)X_C}{2\varphi_C} \tag{5.46}$$

and φ_C is the misalignment angle at failure, when subjected to pure axial compression, and corresponds to:

$$\varphi_C = \arctan\left(\frac{1-\sqrt{1-4\left(\frac{S_L^{is}}{X_C}+\eta_L\right)\frac{S_L^{is}}{X_C}}}{2\left(\frac{S_L^{is}}{X_C}+\eta_L\right)}\right) \tag{5.47}$$

Solving Equation 5.45 can thus be solved using the Newton-Raphson method, where the same relation can be expressed as:

$$F = \chi\gamma_m + \frac{1}{2}(\sigma_{11}-\sigma_{22})\sin(2\gamma_m) - |\sigma_{12}|\cos(2\gamma_m) \tag{5.48}$$

and its derivative as:

$$\frac{dF}{d\gamma_m} = \chi + (\sigma_{11}-\sigma_{22})\cos(2\gamma_m) + 2|\sigma_{12}|\sin(2\gamma_m) \tag{5.49}$$

γ_m is then computed iteratively by:

$$\gamma_m^{i+1} = \gamma_m^i - \frac{F|_{\gamma_m=\gamma_m^i}}{\frac{dF}{d\gamma_m}|_{\gamma_m=\gamma_m^i}} \tag{5.50}$$

Application: The implementation of these criteria can then be summarized through the following algorithms, where Algorithm 4 relates to the transverse failure criteria and Algorithm 5 describes the longitudinal criteria.

Algorithm 4 Transverse failure criteria algorithm

```
Require: $\boldsymbol{\sigma}$, $\boldsymbol{T}^\alpha$, $Y_T^{is}$, $S_L^{is}$, $S_T^{is}$, $\eta_L$, $\eta_T$
  $\kappa \leftarrow \frac{{S_T^{is}}^2 - {Y_T^{is}}^2}{S_T^{is} Y_T^{is}}$
  $\lambda \leftarrow 2\eta_L S_T^{is} / S_L^{is} - \kappa$
  $\alpha \leftarrow 0$
  while $\alpha < 180$ do
      $\boldsymbol{\sigma}^\alpha \leftarrow \boldsymbol{T}^\alpha \boldsymbol{\sigma}$
      $t_N \leftarrow \sigma_{22}^\alpha \quad \wedge \quad t_L \leftarrow \sigma_{12}^\alpha \quad \wedge \quad t_T \leftarrow \sigma_{23}^\alpha$
      if $t_N > 0$ then
          $\phi_{MT} \leftarrow \left(\frac{t_N}{S_T^{is}}\right)^2 + \left(\frac{t_N}{S_T^{is}}\right)^2 + \left(\frac{t_L}{S_L^{is}}\right)^2 + \lambda \left(\frac{t_N}{S_T^{is}}\right) \left(\frac{t_L}{S_L^{is}}\right)^2 + \kappa \left(\frac{t_N}{S_T^{is}}\right)$
      else if $t_N < 0$ then
          $\phi_{MC} \leftarrow \left(\frac{t_L}{S_L^{is} - \eta_L t_N}\right)^2 + \left(\frac{t_T}{S_T^{is} - \eta_T t_N}\right)^2$
      end if
      if $\max(\phi_{MT}, \phi_{MC}) > \phi_M$ then
          $\phi_M \leftarrow \max(\phi_{MT}, \phi_{MC})$
          $\alpha_C \leftarrow \alpha$
      end if
      $\alpha \leftarrow \alpha + 1$
  end while
```

Algorithm 5 Longitudinal failure criteria algorithm

```
Require: $\boldsymbol{\sigma}$, $\boldsymbol{T}^{\theta}$, $\boldsymbol{T}^{\varphi}$, $\boldsymbol{T}^{\alpha}$, $\varepsilon_{11}^{ft}$, $X_C$, $Y_T^{is}$, $S_L^{is}$, $S_T^{is}$, $\eta_L$, $\eta_T$, $tol_\gamma$
  if $\sigma_{11} > 0$ then
      $\phi_{LT} \leftarrow \frac{\varepsilon_{11}}{\varepsilon_{11}^{ft}}$
  else if $\sigma_{11} \leq 0$ then
      $\theta \leftarrow \frac{1}{2}\arctan\left(\frac{\sigma_{23}}{\sigma_{22}-\sigma_{33}}\right)$
      $\boldsymbol{\sigma}^{\theta} \leftarrow \boldsymbol{T}^{\theta}\boldsymbol{\sigma}$
      $\varphi_C \leftarrow \arctan\left(\frac{1-\sqrt{1-4\left(\frac{S_L^{is}}{X_C}+\eta_L\right)\frac{S_L^{is}}{X_C}}}{2\left(\frac{S_L^{is}}{X_C}+\eta_L\right)}\right)$
      $\chi \leftarrow \frac{\sin(2\varphi_C)X_C}{2\varphi_C}$
      while $\Delta\gamma > tol_\gamma$ do
          $F \leftarrow \chi\gamma_m + \frac{1}{2}(\sigma_{11}-\sigma_{22})\sin(2\gamma_m) - |\sigma_{12}|\cos(2\gamma_m)$
          $dF \leftarrow \chi + (\sigma_{11}-\sigma_{22})\cos(2\gamma_m) + 2|\sigma_{12}|\sin(2\gamma_m)$
          $\gamma_{i+1} \leftarrow \gamma_i - \frac{F}{dF}$
          $\Delta\gamma \leftarrow \frac{|\gamma_{i+1}-\gamma_i|}{|\gamma_i|}$
      end while
      if $\sigma_{12}^{\theta} < 0$ then
          $\varphi \leftarrow -\gamma$
      else
          $\varphi \leftarrow \gamma$
      end if
      $\boldsymbol{\sigma}^{\varphi} \leftarrow \boldsymbol{T}^{\varphi}\boldsymbol{\sigma}$
  end if
  ⋮  ▷ Employ the procedure for determining the fracture plane angle from Algorithm 4,
  with the consequent failure indices being $\phi_{KMT}$, $\phi_{KMC}$ and $\phi_K$.
```

5.5 *In situ* Effect

While investigating the occurrence of constrained cracking in the inner layers of cross-ply laminates and the effect that ply thickness had on it, Parvizi et al. [71] observed that when a composite's layer is constrained by plies with different fiber orientations, its transverse tensile and shear strengths are higher than when the same ply is part of a unidirectional laminate .

Under those circumstances, ply strength becomes dependent on the ply's location in the laminate, its relative thickness and the orientation of its neighbouring plies. Therefore, in order to have accurate stress-based models for matrix cracking, it is necessary to take into account this effect and determine the *in situ* transverse and shear strengths of those plies.

With this in mind, Camanho et al. [31] distinguished ply configurations into three fundamental types: *thick plies*, *thin plies*, and *thin outer plies.* This is based on the notion that, under a fracture mechanics approach, these types of plies have inherently different boundary conditions for the propagation of a crack, which ultimately leads to different *in situ* strengths [72].

5.5.1 Thick Plies

In a thick embedded ply, as shown in Figure 5.11, the slit crack is smaller than the ply's thickness. Therefore, it propagates in the transverse direction, until it reaches the neighbouring plies.

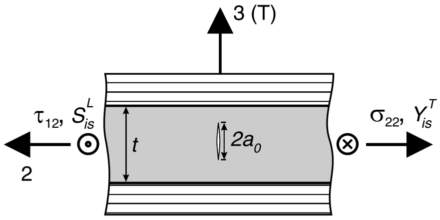

Figure 5.11: Embedded thick ply [31].

The *in situ* tensile strength can be obtained by:

$$Y_T^{is} = \sqrt{\frac{2G_{Ic}^T}{\pi a_0 \Lambda_{22}^0}} \Leftrightarrow Y_T^{is} = 1.12\sqrt{2}Y_T \tag{5.51}$$

where G_{Ic}^T is the mode I transverse fracture toughness, a_0 is half of the slit crack length and Λ_{22}^0, given by Dvorak and Laws [73], is a component of the tensor $\mathbf{\Lambda}$ established by Laws [74] when defining the solution of the interaction energy for a slit crack.

$$\Lambda_{22}^0 = 2\left(\frac{1}{E_2} - \frac{\nu_{21}^2}{E_1}\right) \tag{5.52}$$

Regarding the *in situ* shear strength for a thick ply, it can be obtained from the following expression, where S_L^{is} corresponds to its only positive real root.

$$\frac{(S_L^{is})^2}{G_{12}} + \frac{6}{4}\beta(S_L^{is})^4 = \frac{(S_L^{is})^2}{2G_{12}} + \frac{3}{4}\beta(S_L^{is})^4 \tag{5.53}$$

where β is the shear response factor previously mentioned.

5.5.2 Thin Plies

A thin ply has the same or smaller thickness than its surrounding plies, with the slit crack stretching across the ply's thickness and only growing in the longitudinal direction, as can be observed in Figure 5.12.

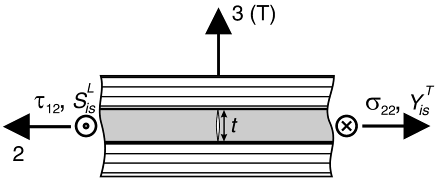

Figure 5.12: Embedded thin ply [31].

The *in situ* tensile strength of this type of ply can be obtained with the following expression, where G_{Ic}^L is the mode I longitudinal fracture toughness and t is the thickness of the ply.

$$Y_{is}^T = \sqrt{\frac{8G_{Ic}^L}{\pi t \Lambda_{22}^0}} \tag{5.54}$$

For a thin ply, the value of the *in situ* shear strength is given as the real root of the following expression:

$$\frac{(S_L^{is})^2}{8G_{12}} + \frac{3}{16}\beta(S_L^{is})^4 = \frac{G_{IIc}^L}{\pi t} \tag{5.55}$$

5.5.3 Outer Plies

In this type of ply, shown in Figure 5.13, the fact that the slit crack is in the vicinity of the surface of the laminate contributes to the magnification of the energy release rate.

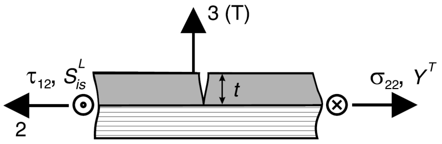

Figure 5.13: Thin outer ply [31].

The *in situ* transverse tensile strength is given as:

$$Y_T^{is} = 1.79\sqrt{\frac{G_{Ic}^L}{\pi t \Lambda_{22}^0}} \tag{5.56}$$

while the *in situ* shear strength is obtained by solving the following expression:

$$\frac{(S_L^{is})^2}{4G_{12}} + \frac{3}{8}\beta(S_L^{is})^4 = \frac{G_{IIc}^L}{\pi t} \tag{5.57}$$

5.5.4 Generalized in situ shear strength

Camanho et al. [31] verified that the solution of the *in situ* shear strength for each of the layer types has the same general form, given by:

$$S_L^{is} = \sqrt{\frac{\sqrt{1+\beta\phi {G_{12}}^2} - 1}{3\beta G_{12}}} \tag{5.58}$$

where ϕ is dependent on the ply configuration:

$$\phi = \begin{cases} \frac{12(S_L)^2}{G_{12}} + 18\beta(S_L)^4 & \text{, for a thick ply.} \\ \frac{48G_{IIc}}{\pi t} & \text{, for a thin ply.} \\ \frac{24G_{IIc}}{\pi t} & \text{, for an outer ply.} \end{cases} \tag{5.59}$$

Application: The procedure for obtaining the *in situ* material properties can thus be summarized in the form of Algorithm 6.

Algorithm 6 Assessment of *in situ* properties

```
Require: $E_1$, $E_2$, $G_{12}$, $\nu_{12}$, $Y_T$, $S_L$, $\beta$, $t_{ply}$, $G_{Ic}^L$, $G_{IIc}^L$, location, ply_type
  $\Lambda_{22}^0 \leftarrow 2\left(\frac{1}{E_2} - \frac{{\nu_{21}}^2}{E_1}\right)$
  if location = inner then
      if ply_type = thick then
          $\phi \leftarrow \frac{12{S_L}^2}{G_{12}} + 18\beta {S_L}^4$
          $Y_T^{is} \leftarrow 1.12\sqrt{2}Y_T$
      else if ply_type = thin then
          $\phi \leftarrow \frac{48G_{IIc}^L}{\pi t_{ply}}$
          $Y_T^{is} \leftarrow \sqrt{\frac{8G_{Ic}^L}{\pi t \Lambda_{22}^0}}$
      end if
  else if location = outer then
      $\phi \leftarrow \frac{24G_{IIc}^L}{\pi t_{ply}}$
      $Y_T^{is} \leftarrow 1.79\sqrt{\frac{G_{Ic}^L}{\pi t \Lambda_{22}^0}}$
  end if
  $S_L^{is} \leftarrow \sqrt{\frac{\sqrt{1+\beta\phi {G_{12}}^2}-1}{3\beta G_{12}}}$
```

5.6 Failure Damage

Three formulations for the evolution of failure damage were evaluated according to their ability to describe the post-failure behaviour of the material and the fracture energy resulting from their application.

The numerical implementation of all approaches took into account the regularization of the dissipated energy by including the characteristic length of the finite element in its calculation. This ensures that the solution is objective and independent of mesh refinement and element geometry [75].

5.6.1 First Method

In this approach, Wang et al. [54] implements linear progressive damage laws similar to those found in cohesive element damage formulation. The damage factor is based on the instantaneous strain present at each time step ε, the damage onset strain ε^0 and the complete failure strain ε^f. The failure damage variables are thus given by:

$$d_{ft} = \frac{\varepsilon_{ft}^f}{\varepsilon_{ft}^f - \varepsilon_{ft}^0}\left(1 - \frac{\varepsilon_{ft}^0}{\varepsilon_{ft}}\right) \tag{5.60}$$

$$d_{fc} = \frac{\varepsilon_{fc}^f}{\varepsilon_{fc}^f - \varepsilon_{fc}^0}\left(1 - \frac{\varepsilon_{fc}^0}{\varepsilon_{fc}}\right) \tag{5.61}$$

where the indices ft and fc represent the fiber tensile and compressive failure modes, respectively. The damage initiation strains and complete damage strains are:

$$\varepsilon_{ft}^0 = \frac{X_T}{E_{11}} \qquad \varepsilon_{ft}^f = \frac{2G_{fC}^T}{X_T L^c} \tag{5.62}$$

$$\varepsilon_{fc}^0 = \frac{X_C}{E_{11}} \qquad \varepsilon_{fc}^f = \frac{2G_{fC}^C}{X_C L^c} \tag{5.63}$$

where G_{fC}^T and G_{fC}^C represent the fracture toughness associated with fiber tensile and compressive failure, respectively, and L^c corresponds to the characteristic element length. The longitudinal failure behaviour under this formulation in tension, compression, and cyclic tension and compression is highlighted by Figure 5.14.

Regarding the matrix failure damage components, they are expressed as follows:

$$d_{mt} = \frac{\varepsilon_{mt}^f}{\varepsilon_{mt}^f - \varepsilon_{mt}^0}\left(1 - \frac{\varepsilon_{mt}^0}{\varepsilon_{mt}}\right) \tag{5.64}$$

$$d_{mc} = \frac{\varepsilon_{mc}^f}{\varepsilon_{mc}^f - \varepsilon_{mc}^0}\left(1 - \frac{\varepsilon_{mc}^0}{\varepsilon_{mc}}\right) \tag{5.65}$$

where mt and mc correspond to the matrix tensile and compressive failure modes. In the tensile direction, the damage initiation strains and complete damage strains are obtained

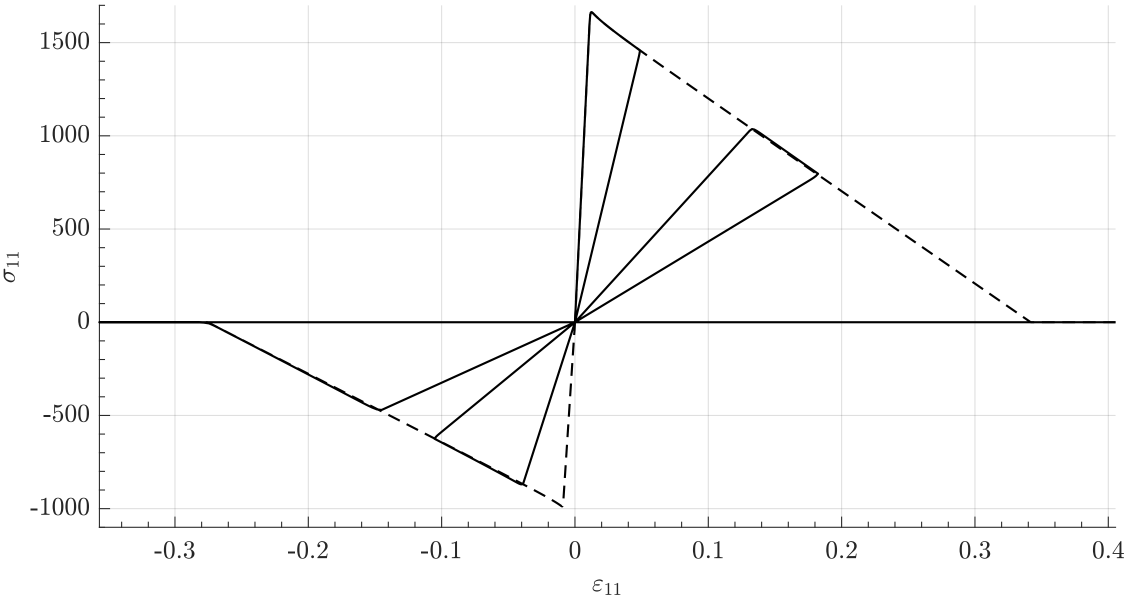

Figure 5.14: Longitudinal stress strain response under the Wang et al. failure damage formulation. Dashed lines correspond to pure tensile and compressive behaviour while the solid line represents a cyclic load scenario, alternating between tensile and compressive stresses.

in a similar way to the fiber related ones:

$$\varepsilon^0_{mt} = \frac{Y_T}{E_{22}} \qquad \varepsilon^f_{mt} = \frac{2G^T_{mC}}{Y_T L^c} \tag{5.66}$$

where G^T_{mC} corresponds to the fracture toughness of the matrix under tensile failure. For compressive matrix failure, the damage factor is dependent on the strains acting on the fracture plane. Hence, $\varepsilon_{mc} = \sqrt{{\varepsilon_n}^2 + {\gamma_T}^2 + {\gamma_L}^2}$ where:

$$\begin{cases} \varepsilon_n = \varepsilon_{22}\cos^2\theta + \varepsilon_{33}\sin^2\theta + \gamma_{23}(\cos^2\theta - \sin^2\theta) \\ \gamma_T = 2(\varepsilon_{33} - \varepsilon_{22})\sin\theta\cos\theta + \gamma_{23}(\cos^2\theta - \sin^2\theta) \\ \gamma_L = \gamma_{31}\sin\theta + \gamma_{21}\cos\theta \end{cases} \tag{5.67}$$

In this case, the value for the onset strain ε^0_{mc} is obtained by recording the value of the strain ε_{mc} when failure occurs and the value for the final strain ε^f_{mc} is given by:

$$\varepsilon^f_{mc} = \frac{2G^C_{mC}}{\sigma^0_{mc} L^c} \tag{5.68}$$

where G^T_{mC} is the fracture toughness of the matrix under tensile failure and the onset stress σ^0_{mc} is obtained in a similar way to that of the onset strain ε^0_{mc}, that is, saving the value of $\sigma_{mc} = \sqrt{{\sigma_n}^2 + {\tau_T}^2 + {\tau_L}^2}$ when compressive matrix failure occurs.

The post failure behaviour for matrix failure is similar to that of fiber failure, shown in Figure 5.14.

5.6.2 Second Method

Linde et al. [36] describes the behaviour of damage after failure as a gradual deterioration, with its exponential evolution being governed by the dissipation of the fracture energy of the fiber or matrix, depending on the failed constituent.

Fiber and matrix deterioration after failure are controlled by the same formulation:

$$d_k = 1 - \frac{\varepsilon_{ii}^{k}}{f_k} e^{\frac{-C_{ii}\varepsilon_{ii}^{f}(f_k - \varepsilon_{ii}^{f})}{G_{Ck}}} \tag{5.69}$$

where $k = f, m$ representing either fiber or matrix, C_{ii} is the modulus stiffness described in Section 4 and G_{Ck} is the fracture energy of the constituent.

Given that the original formulation is established in relation to criteria that assume the occurrence of failure once the maximum principal strains are reached (see Section 4.2.3.1) and that the criteria employed in this model do so by means of failure indexes, it is necessary to adapt the formulation of damage evolution as follows:

$$d_k = 1 - \frac{1}{f_k} e^{\frac{(1-f_k)C_{ii}L^{c}\varepsilon_{i}^{f\,2}}{G_{Ck}}} \tag{5.70}$$

Thus, Figure 5.15 highlights the post-failure behaviour according to the described formulation, for fiber tension and compression, with the matrix post-failure behaviour being similar due to being based on the same formulation.

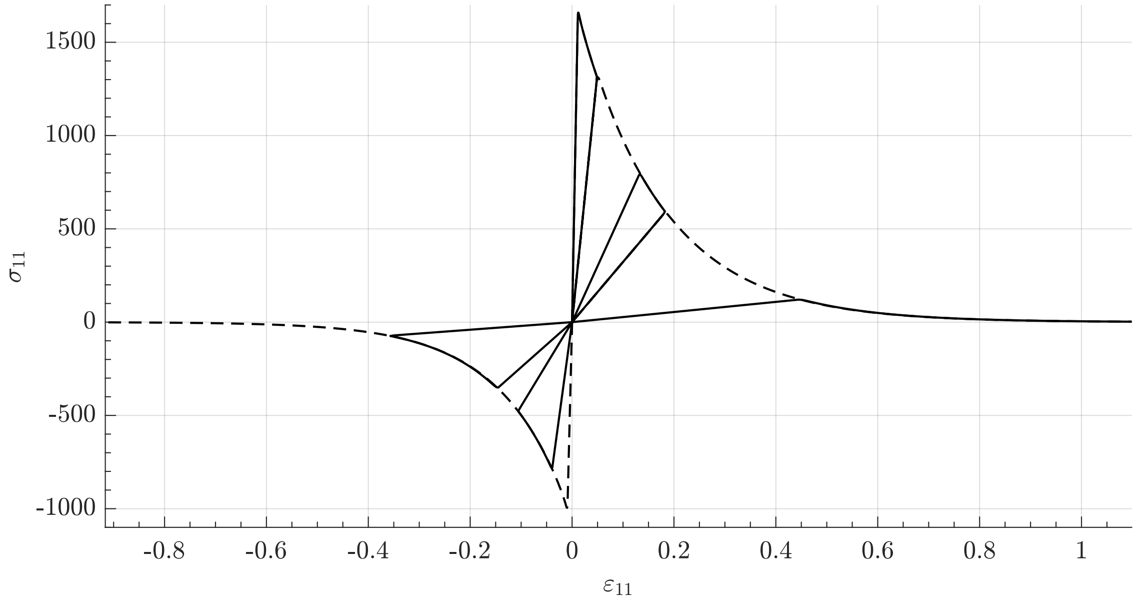

Figure 5.15: Longitudinal stress strain response with the Linde et al. failure damage formulation under the same loading scenarios as previously.

5.6.3 Third Method

The final approach that was analyzed for modeling the propagation of intralaminar failure mechanisms was developed by Maimí et al. [60, 76]. Like the other approaches, once a failure criterion is activated, the damage evolution laws force softening of the material, differentiating between fiber and matrix failure modes. Moreover, in the latter, closure and opening of crack under cyclic load reversal is taken into account.

Except for the longitudinal damage evolution law, the response of all the failure modes is represented by exponential laws. In a sense, it mixes the first method which is purely linear with the second which is completely exponential.

Under longitudinal tensile loading, the damage law is composed of two phases. The first, linear stage, simulates the fiber-bridging and fiber pull-out phenomena. Once the fiber pull-out strength X_{PO} is reached the softening response starts following an exponential law, as illustrated in Figure 5.16a.

$$d_{1+} = 1 - (1 - d_{1+}^{L})(1 - d_{1+}^{E}) \tag{5.71}$$

where d_{1+}^{L} and d_{1+}^{E} correspond to the linear and exponential damage variables. In the case of longitudinal compression, the law consists of a combination of the failure mechanisms caused by tensile, $d_{1+}(r_{1+})$, and compressive, $d_{1-}^{*}(r_{1-})$, loads:

$$d_{1-} = 1 - [1 - d_{1-}^{*}(r_{1-})][1 - A_{1}^{\pm} d_{1+}(r_{1+})] \tag{5.72}$$

Under the transverse domain, the tensile and compressive damage variables operate in a similar manner to the longitudinal ones, with tensile damage considering compressive and tensile mechanisms and compressive damage accounting only for compressive, owing to the matrix crack closure effect occurring under load reversal, as can be verified in Figure 5.16b.

$$d_{2+} = 1 - \frac{1}{f_{2+}(r_{2+})} \exp\left[A_{2+}(1 - f_{2+}(r_{2+}))\right] \tag{5.73}$$

$$d_{2-} = 1 - \frac{1}{r_{2-}} \exp\left[A_{2-}(1 - r_{2-})\right] \tag{5.74}$$

where the parameters A_{2+} and A_{2-} are obtained through numerical integration algorithms. Shear loading results in shear stiffness reduction as a result of longitudinal and transverse cracks, with its damage variable being defined as follows:

$$d_{6} = 1 - [1 - d_{6}^{*}(r_{2+})](1 - d_{1+}) \tag{5.75}$$

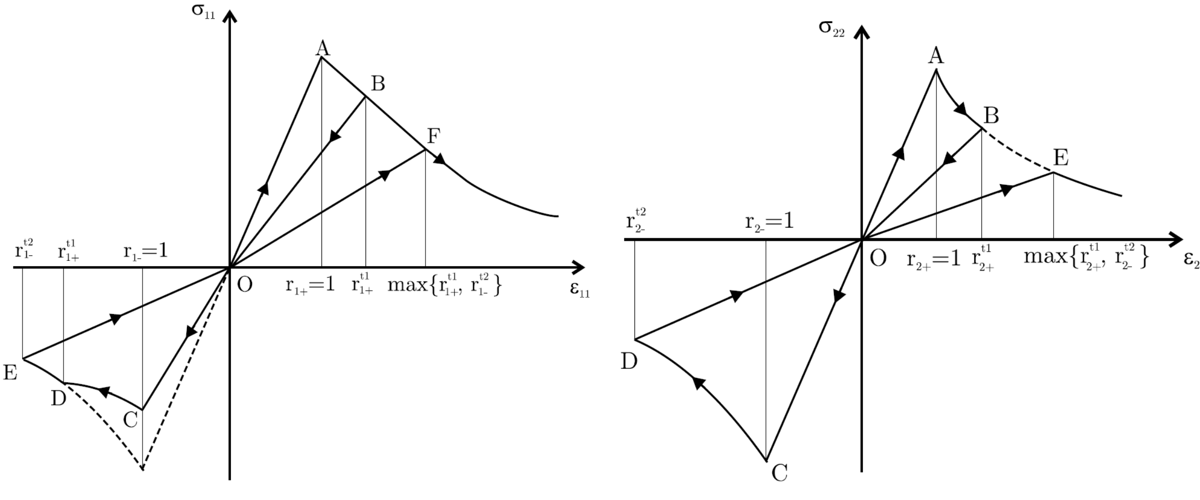

(a) **(b)**

Figure 5.16: Stress strain response under the Maimi et al. damage formulation for (a) longitudinal load cycle O–A–B–O–C–D–E–O–F and (b) transverse load cycle O–A–B–O–C–D–O–E [76].

5.6.4 Comparison

Numerical simulations employing the described failure damage evolution approaches were conducted in order to assess their effectiveness and computational efficiency. The fracture energy resulting from each method was obtained by calculating the area under the stress-strain curve through trapezoidal numeric integration and multiplying it by the characteristic element length, L^c.

Table 5.1: Comparison of the values obtained by each formulation for the fracture energy per unit area in relation to the experimental result, per failure mode. Evaluation made for the AS4/PEEK composite, with experimental values sourced from Lachaud [59].

	Experimental	**Wang**	**Linde**	**Maimí**
Fiber Tension - G_{Ic}^{ft} [N/mm]	218	214.82	218.16	215.70
Relative Error [%]	-	1.46	0.07	1.06
Fiber Compression - G_{Ic}^{fc} [N/mm]	104	102.66	103.66	102.48
Relative Error [%]	-	1.29	0.33	1.46
Matrix Tension - G_{Ic}^{mt} [N/mm]	1.16	0.96	1.05	-
Relative Error [%]	-	17.24	9.48	-
Matrix Compression - G_{Ic}^{mc} [N/mm]	1.98	4.67	2.04	-
Relative Error [%]	-	135.86	3.03	-

As can be verified in Table 5.1, the Linde et al. formulation obtained the most accurate results across all loading scenarios. It is necessary to mention that the Maimí formulation was not tested in the transverse domain due to the high complexity of the processes necessary to obtain its auxiliary parameters, which leaves room for the possibility of this approach achieving better results in that scenario.

Nevertheless, the Maimí continuum damage model presents the most comprehensive formulation of all three, given its incorporation of several relevant physical phenomena.

Thus, a similar approach to the response described by it under tensile and compressive load reversal scenarios in both the longitudinal and transverse domains will be included in the model under development.

It is understood that the longitudinal and transverse damage domains are not coupled due to the experimental results [77] and micromechanical models [78, 79, 80, 81] present in the literature. Conversely, compression and tensile damage present a coupled nature, influencing the material response under load reversal [60].

In the case of the transverse domain, tensile loads cause cracks perpendicular to the mid-plane, i.e. with $\alpha = 0°$. If the material is then subjected to compressive loads, those cracks close and, in effect, the transverse damage variable returns to its previous state. On the contrary, if the material is subjected to compressive loads that result in matrix cracking, this damage directly affects the tensile response, in the same manner that tension originated cracks do.

Regarding longitudinal loading, in the case of tensile stresses, the fracture is perpendicular to the fiber direction, with the occurrence of fiber and matrix cracking. Load reversal then leads to the closure of cracks and regeneration of matrix strength but not of the fractured fibers. In the case of compressive loads, the fiber kinking phenomenon originates kink bands and matrix cracking which, under load reversal, contribute to the tensile damage in a similar way to what occurs in the transverse domain.

Hence, the implemented softening response after failure is governed by the formulation developed by Linde et al. [36], with the load reversal considerations expressed by Maimí et al. [60]. Given that the damage parameter never truly reaches the value of one, reaching instead a saturation limit [59], maximum values of 0.87 and 0.95 are imposed on the fiber and matrix damage variables, respectively [68], which also helps prevent the occurrence of numerical instabilities in the computational implementation.

Application: Failure damage evolution can then be specified in a concise manner through Algorithm 7 in the case of fiber failure damage and Algorithm 8 in the case of matrix failure damage.

Algorithm 7 Fiber failure damage evolution

```
Require: $fi_{ft}$, $fi_{fc}$, $f_{ft}$, $f_{fc}$, $L^c$, $X_T$, $X_C$, $E_1$, $C_{11}$, $G^T_{fC}$, $G^C_{fC}$
  if $fi_{ft} > 1$ then
      if $f_{ft} \leftarrow 0$ then
          $L^c_f \leftarrow L^c$
          $f_{ft} \leftarrow 1$
      end if
      $\varepsilon^{ft}_{11} \leftarrow \frac{X_T}{E_1}$
      $d_{ft} \leftarrow 1 - \frac{1}{fi_{ft}} e^{\frac{(1-fi_{ft})C_{11}L^c_f {\varepsilon^{ft}_{11}}^2}{G^T_{fC}}}$
  else if $fi_{fc} > 1$ then
      if $f_{fc} \leftarrow 0$ then
          $L^c_f \leftarrow L^c$
          $f_{fc} \leftarrow 1$
      end if
      $\varepsilon^{fc}_{11} \leftarrow -\frac{X_C}{E_1}$
      $d_{fc} \leftarrow 1 - \frac{1}{fi_{fc}} e^{\frac{(1-fi_{fc})C_{11}L^c_f {\varepsilon^{fc}_{11}}^2}{G^C_{fC}}}$
  end if
  $d_f \leftarrow \min\left(0.87, \max\left(d_{ft}, d_{fc}\right)\right)$
```

Algorithm 8 Matrix failure damage evolution

```
Require: $fi_{mt}$, $fi_{mc}$, $f_{mt}$, $f_{mc}$, $fi_{kmt}$, $fi_{kmc}$, $f_{kmt}$, $f_{kmc}$, $L^c$, $Y_T$, $Y_C$, $E_2$, $C_{22}$, $G_C^{mt}$, $G_C^{mc}$
  $mode \leftarrow \{mt, mc, kmt, kmc\}$
  for $i = 1, mode(end)$ do
      if $fi_{mode(i)} > 1$ then
          if $f_{mode(i)} \leftarrow 0$ then
              $L_m^c \leftarrow L^c$
              $f_{mode(i)} \leftarrow 1$
              $\varepsilon_{22}^{mode(i)} \leftarrow \varepsilon_{22}$
          end if
          $d_{mode(i)} \leftarrow 1 - \frac{1}{fi_{mode(i)}} e^{\frac{(1-fi_{mode(i)}) C_{22} L_m^c \varepsilon_{22}^{mode(i)^2}}{G_C^{mode(i)}}}$
      end if
      if $\varepsilon_{22} > 0$ then
          $d_m \leftarrow \min(0.95, \max(d_{mt}, d_{mc}, d_{kmt}, d_{kmc}))$
      else if $\varepsilon_{22} < 0$ then
          $d_m \leftarrow \min(0.95, \max(d_{mc}, d_{kmc}))$
      end if
  end for
```

5.7 Overview of the Constitutive Model

A general scheme of the constitutive model is presented in Figure 5.17, highlighting the role of each module in achieving the desired output.

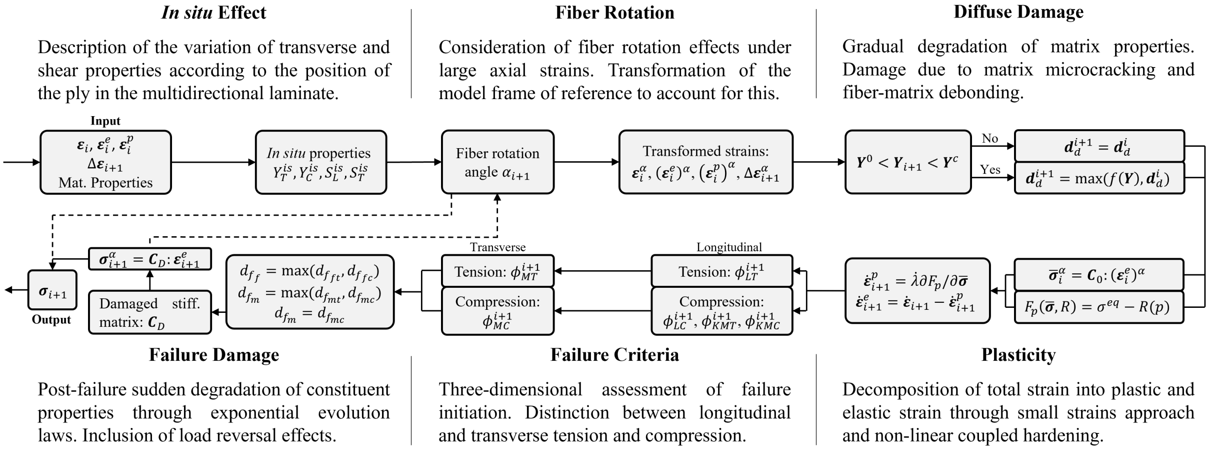

***In situ* Effect**

Description of the variation of transverse and shear properties according to the position of the ply in the multidirectional laminate.

Fiber Rotation

Consideration of fiber rotation effects under large axial strains. Transformation of the model frame of reference to account for this.

Diffuse Damage

Gradual degradation of matrix properties. Damage due to matrix microcracking and fiber-matrix debonding.

Failure Damage

Post-failure sudden degradation of constituent properties through exponential evolution laws. Inclusion of load reversal effects.

Failure Criteria

Three-dimensional assessment of failure initiation. Distinction between longitudinal and transverse tension and compression.

Plasticity

Decomposition of total strain into plastic and elastic strain through small strains approach and non-linear coupled hardening.

Figure 5.17: Structure of the developed constitutive model.

Part IV

Numerical Implementation

Chapter 6

Subroutine Development

Once the constitutive model is developed, the next step is its implementation in a computational framework. In the current approach, the commercial finite element analysis software Abaqus developed by Dassault Systèmes was the platform selected by Airbus Atlantic and the constitutive model was applied in both its Standard and Explicit schemes.

The final objective of the project is to develop a material model for the thermoplastic at hand, which can be used for static and dynamic analyses. This requires its implementation in the Abaqus finite element solver through a User Material (UMAT) subroutine and a Vectorized User Material (VUMAT) subroutine. Both options were developed because the UMAT provides higher fidelity results for static simulations, where convergence of the implicit formulation is achievable while the VUMAT, is especially useful for dynamic solicitations and impact cases, where the strain-rate effect becomes relevant. In that case, given the high non-linearities and strain rates, the convergence of the implicit formulation is difficult. Hence, the VUMAT uses an explicit formulation, advancing incrementally the kinematic state, resulting in less precision but not requiring convergence at each increment. A simplified scheme of the Abaqus solver stages in presented in Figure 6.1.

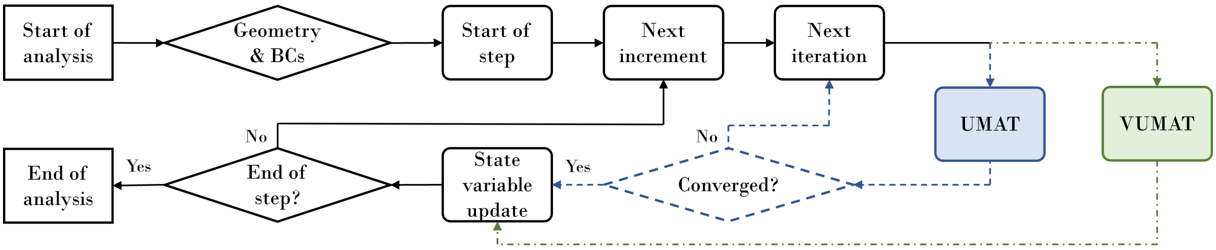

Figure 6.1: Simplified flowchart of the Abaqus solver, adapted from [82], where dashed lines pertain to phases exclusively involving the Standard solver and dash-dotted lines relate to the Explicit solver.

6.1 General Considerations

Given the application of the constitutive model in a numeric environment via the Abaqus software, it is important to consider this new context and make some adjustments.

6.1.1 Return Mapping Algorithm

Since the implementation of the constitutive model is done incrementally, a given increase of stress may lead to the infringement of the condition that F_p must be lower or equal than zero. In this scenario, the stress must be brought back to the yield surface by means of a return mapping algorithm. The implemented method is a radial return algorithm with basis on the backwards Euler integration procedure [54, 83, 84] similar to the closest point projection method [85], whose the procedure is established in Algorithm 9 and is illustrated in Figure 6.2, where the n variable represents the previous increment and the k variable corresponds to the iteration of the return mapping algorithm.

Algorithm 9 Plasticity update with return mapping algorithm

```
Require: $\bar{\boldsymbol{\sigma}}$, $\boldsymbol{C}_0$, $\boldsymbol{\varepsilon}$, $\Delta\boldsymbol{\varepsilon}$, $R(p)$, $a^2$
Ensure: Matrix failure has not occurred.
  $\boldsymbol{\varepsilon}_{n+1} \leftarrow \boldsymbol{\varepsilon}_n + \Delta\boldsymbol{\varepsilon}_{n+1}$
  $\bar{\boldsymbol{\sigma}}^{trial}_{n+1} \leftarrow \bar{\boldsymbol{\sigma}}_n + \boldsymbol{C}_0 : \Delta\boldsymbol{\varepsilon}_{n+1}$
  $F_p \leftarrow \sqrt{\bar{\sigma}^2_{12} + \bar{\sigma}^2_{13} + \bar{\sigma}^2_{23} + a^2(\bar{\sigma}^2_{22} + \bar{\sigma}^2_{33})} - R(p_n)$
  if $F_p > 0$ then
    while $F_p > 0$ do
      $\delta\lambda^{(k)} \leftarrow \frac{\frac{\partial F_p^{(k)}}{\partial \bar{\boldsymbol{\sigma}}}:\boldsymbol{C}_0:(\Delta\boldsymbol{\varepsilon}_{n+1} - \Delta\boldsymbol{\varepsilon}^{p(k)})}{\frac{\partial F_p^{(k)}}{\partial \bar{\boldsymbol{\sigma}}}:\boldsymbol{C}_0:\frac{\partial F_p^{(k)}}{\partial \bar{\boldsymbol{\sigma}}} + \frac{\partial R}{\partial p}}$
      if $\delta\lambda^{(k)} < 0$ then
        $\delta\lambda^{(k)} \leftarrow 0$
      end if
      $\Delta\lambda^{(k+1)}_{n+1} \leftarrow \Delta\lambda^{(k)}_{n+1} + \delta\lambda^{(k)}$
      $\Delta\boldsymbol{\varepsilon}^{p(k+1)} \leftarrow \Delta\lambda^{(k+1)}_{n+1} \frac{\partial F_p^{(k)}}{\partial \bar{\boldsymbol{\sigma}}}$
      ${\boldsymbol{\varepsilon}^p_{n+1}}^{(k+1)} \leftarrow \boldsymbol{\varepsilon}^p_n + \Delta\boldsymbol{\varepsilon}^{p(k+1)}$
      $\bar{\boldsymbol{\sigma}}^{(k+1)}_{n+1} \leftarrow \boldsymbol{C}_0 : (\boldsymbol{\varepsilon}_{n+1} - {\boldsymbol{\varepsilon}^p_{n+1}}^{(k+1)})$
      $p^{(k+1)}_{n+1} \leftarrow p_n + \Delta\lambda^{(k+1)}_{n+1}$
      $F_p \leftarrow \sigma^{(k+1)}_{eq} - R\left(p^{(k+1)}_{n+1}\right)$
    end while
  else
    $\Delta\lambda_{n+1} \leftarrow 0$
  end if
  $\Delta\boldsymbol{\varepsilon}^p_{n+1} \leftarrow \Delta\lambda_{n+1} \frac{\partial F_{p_{n+1}}}{\partial \bar{\boldsymbol{\sigma}}_{n+1}}$
  $\boldsymbol{\varepsilon}^e_{n+1} \leftarrow \boldsymbol{\varepsilon}_{n+1} - (\boldsymbol{\varepsilon}^p_n + \Delta\boldsymbol{\varepsilon}^p_{n+1})$
```

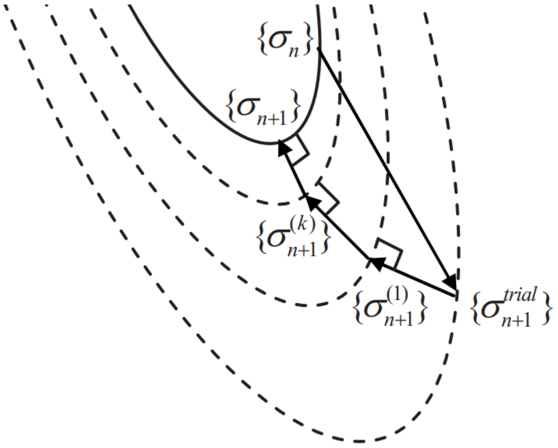

Figure 6.2: Stress return corresponding to the closest point projection algorithm [84].

6.1.2 Fiber Rotation

It is important to note that, within the Abaqus operating environment, the material coordinate system does not change based on the deformation sustained by the element (Figure 6.3), hence the necessity for a fiber rotation algorithm within the subroutine. Alternatively, a ORIENT subroutine could have been developed but this was not deemed expedient for the current project.

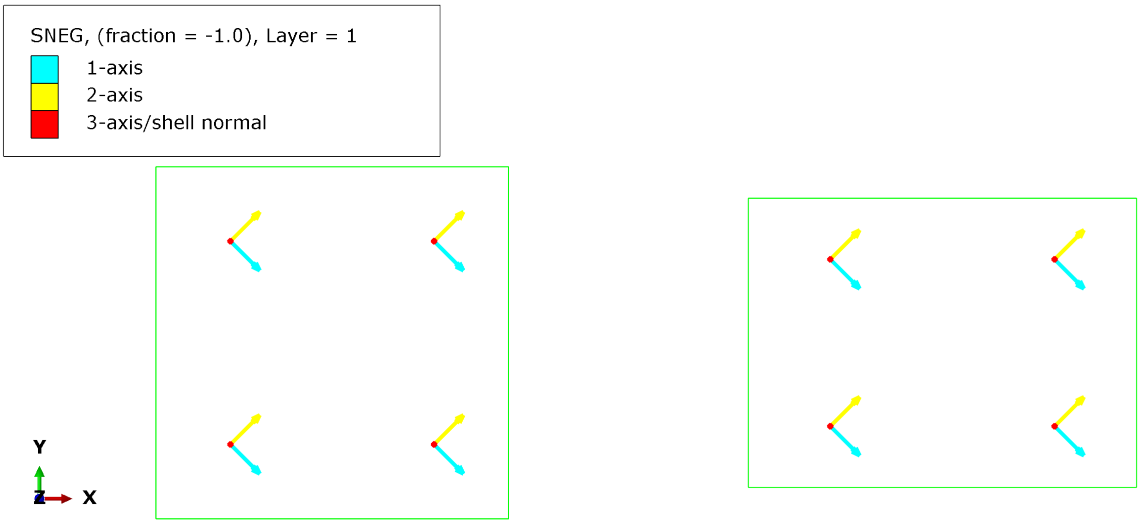

Figure 6.3: Abaqus material orientation vectors in (left) undeformed and (right) deformed element.

Although Algorithm 3 describes the process by which strains are transformed into their updated orientation following the event of fiber rotation, it is necessary to transform the resulting stress back into the element frame of reference.

Therefore, after the procedures of the subroutine have concluded, the resulting stress and Jacobian (in the case of the UMAT) tensors are rotated by:

$$\sigma_{11}^{undef} = \frac{\sigma_{11}+\sigma_{22}}{2} + \frac{\sigma_{11}-\sigma_{22}}{2}\cos 2(\theta-\theta') + \sigma_{12}\sin 2(\theta-\theta') \tag{6.1}$$

$$\sigma_{22}^{undef} = \frac{\sigma_{11}+\sigma_{22}}{2} - \frac{\sigma_{11}-\sigma_{22}}{2}\cos 2(\theta-\theta') - \sigma_{12}\sin 2(\theta-\theta') \tag{6.2}$$

$$\sigma_{12}^{undef} = -\frac{\sigma_{11}-\sigma_{22}}{2}\sin 2(\theta-\theta') + \sigma_{12}\cos 2(\theta-\theta') \tag{6.3}$$

6.1.3 Required Inputs

The properties given in Table 6.1 relate to the inputs necessary to effectively run the subroutines. The indices one to six concern the stiffness moduli, seven through nine the Poisson ratios, 10 to 18 the failure strains, 19 to 24 the material strengths, 25 the fracture angle under matrix compression failure, 26 the longitudinal friction coefficient, 27 the shear response factor, 28 to 32 the fracture toughnesses, 33 the viscous regularization parameter, 34 specifies the location of the ply, used in the *in situ* effect and 35 the orientation angle of the ply.

Table 6.1: Property vector inputted in the beginning of each iteration of the subroutines.

props(1)	E_1	**props(13)**	ε_{11}^{c}	**props(25)**	α_0
props(2)	E_2	**props(14)**	ε_{22}^{c}	**props(26)**	η_L
props(3)	E_3	**props(15)**	ε_{33}^{c}	**props(27)**	β
props(4)	G_{12}	**props(16)**	ε_{12}^{s}	**props(28)**	G_{IC}^{ft}
props(5)	G_{13}	**props(17)**	ε_{13}^{s}	**props(29)**	G_{IC}^{fc}
props(6)	G_{23}	**props(18)**	ε_{23}^{s}	**props(30)**	G_{IC}^{mt}
props(7)	ν_{12}	**props(19)**	X_T	**props(31)**	G_{IC}^{mc}
props(8)	ν_{13}	**props(20)**	X_C	**props(32)**	G_{IIC}^{ms}
props(9)	ν_{23}	**props(21)**	Y_T	**props(33)**	η
props(10)	ε_{11}^{t}	**props(22)**	Y_C	**props(34)**	ply location
props(11)	ε_{22}^{t}	**props(23)**	S_L	**props(35)**	ply angle
props(12)	ε_{33}^{t}	**props(24)**	S_T		

6.2 User Material Subroutine

The UMAT runs in the context of the Standard solver, where the formulation is implicit and equilibrium is enforced between externally applied loads and internally generated reaction forces at every solution step, using the Newton Raphson method. This approach is unconditionally stable, being incremental as well as iterative.

Therefore, some considerations have to be taken into account while developing the UMAT, especially regarding the stability and convergence of the calculation.

6.2.1 Viscous Regularization

Softening behaviour and stiffness degradation in implicit analysis might lead to instabilities in the simulation due to spurious loss of positive definiteness of the tangent stiffness matrix, which leads to damage localization and convergence issues [86].

In order to avoid this, viscous regularization is introduced, causing the tangent stiffness matrix to be positive definite for small time increments and improving the convergence of the implicit calculation. This is done by regularizing the damage variables through the introduction of a viscosity regularization factor η, where the viscous damage variable is given by:

$$\delta d_\nu = \frac{1}{\eta}(d - d_\nu)\delta t \tag{6.4}$$

which is then used to compute the viscous damaged elastic matrix $\boldsymbol{C}_d^\nu$ and the viscous Jacobian matrix $\frac{\partial \Delta \boldsymbol{\sigma}^\nu}{\partial \Delta \varepsilon}$ instead of the previously calculated damage variables d. The stress output of the UMAT is also given in its viscous form $\boldsymbol{\sigma}^\nu$.

Given that η represents the relaxation time of the viscous system, using this value such that $\eta < \Delta t$ improves the convergence without compromising the accuracy of the results [87]. In effect, the solution of the regularized system then relaxes to that of the inviscid case as time increases. Implementing this concept in the UMAT requires the use of a backward Euler approach, resulting in the following relation for the viscous damage:

$$d_\nu^{t+\Delta t} = \frac{\eta}{\eta + \Delta t} d_\nu^t + \frac{\Delta t}{\eta + \Delta t} d^{t+\Delta t} \tag{6.5}$$

It is possible to observe in Figure 6.4 the effects of different viscous regularization values, with the relaxation times being evidently larger as η increases.

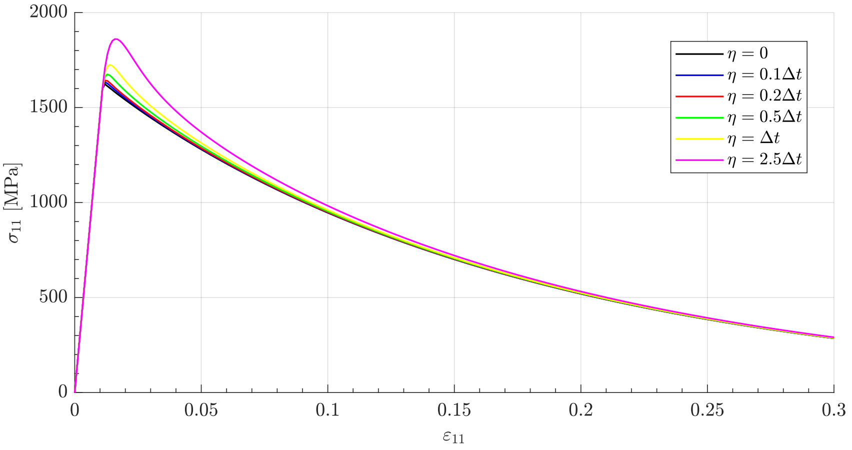

Figure 6.4: Effect of different values of η in the final stress strain curve.

6.2.2 Jacobian matrix

Besides the stress tensor, the UMAT is required to provide the Jacobian matrix, given by:

$$\overline{\overline{\boldsymbol{J}}} = \frac{\partial \Delta \boldsymbol{\sigma}}{\partial \Delta \boldsymbol{\varepsilon}} = \begin{bmatrix} \frac{\partial \sigma_{11}}{\partial \varepsilon_{11}} & \frac{\partial \sigma_{11}}{\partial \varepsilon_{22}} & \frac{\partial \sigma_{11}}{\partial \varepsilon_{33}} & 0 & 0 & 0 \\ \frac{\partial \sigma_{22}}{\partial \varepsilon_{11}} & \frac{\partial \sigma_{22}}{\partial \varepsilon_{22}} & \frac{\partial \sigma_{22}}{\partial \varepsilon_{33}} & 0 & 0 & 0 \\ \frac{\partial \sigma_{33}}{\partial \varepsilon_{11}} & \frac{\partial \sigma_{33}}{\partial \varepsilon_{22}} & \frac{\partial \sigma_{33}}{\partial \varepsilon_{33}} & 0 & 0 & 0 \\ \frac{\partial \sigma_{12}}{\partial \varepsilon_{11}} & \frac{\partial \sigma_{12}}{\partial \varepsilon_{22}} & 0 & \frac{\partial \sigma_{12}}{\partial \varepsilon_{12}} & 0 & 0 \\ \frac{\partial \sigma_{13}}{\partial \varepsilon_{11}} & 0 & \frac{\partial \sigma_{13}}{\partial \varepsilon_{33}} & 0 & \frac{\partial \sigma_{13}}{\partial \varepsilon_{13}} & 0 \\ 0 & \frac{\partial \sigma_{23}}{\partial \varepsilon_{22}} & \frac{\partial \sigma_{23}}{\partial \varepsilon_{33}} & 0 & 0 & \frac{\partial \sigma_{23}}{\partial \varepsilon_{23}} \end{bmatrix} \tag{6.6}$$

This is necessary due to the use of a backwards Euler procedure by the Standard solver, which requires the Newton Raphson method to be implemented.

Each of the terms are specified analytically, where an example of one is given as:

$$\begin{aligned} \frac{\partial \sigma_{11}}{\partial \varepsilon_{11}} = (1-d_{f1})(1-d_{d1})C_{11} - \frac{\partial d_{d1}}{\partial \varepsilon_{11}}(1-d_{f1})C_{11}\varepsilon_{11} - \frac{\partial d_{f1}}{\partial \varepsilon_{11}}(1-d_{d1})C_{11}\varepsilon_{11} - \\ \frac{\partial d_{f1}}{\partial \varepsilon_{11}}(1-d_{d2})(1-d_{f2})C_{12}\varepsilon_{22} - \frac{\partial d_{f1}}{\partial \varepsilon_{11}}(1-d_{d3})(1-d_{f3})C_{13}\varepsilon_{33} \end{aligned} \tag{6.7}$$

6.3 Vectorised User Material Subroutine

The VUMAT, through the Explicit solver, does not require the calculation of the Jacobian matrix, neither does it require the solution to converge at every increment. Its accuracy is obtained by significantly reducing the increment size, with the solution being determined without iterating by explicitly advancing the kinematic state from the previous increment. Therefore, it is much less demanding, especially so for complex models.

Unfortunately, it was not possible to finish the implementation of the VUMAT in the computational framework, given that higher priority was given to the UMAT. Therefore, the VUMAT is missing three-dimensional coupled plasticity, only presenting coupling between the transverse and shear directions, and three-dimensional failure criteria, having the previously implemented the Linde failure criteria, introduced in Section 4.2.3.1.

Chapter 7

Validation

The robustness of the model will be evaluated by subjecting it to various stress conditions, first through an RVE with fundamental load scenarios and then by simulating standard test specimens. Numerical results will be compared with experimental tests available in the literature. Multiple modeling strategies were implemented in the Standard and Explicit solving schemes:

1. Standard:
    (a) **UMAT SE** - Single Element model, used only in the RVE.
    (b) **UMAT CL** - Continuous Laminate (modeled using the *Composite Layup* tool of the *Property* module. Only valid in Standard since, in Explicit, solid elements can only be composed of a single homogeneous material).
    (c) **UMAT DL** - Discrete Laminate (each layer is modeled individually).
2. Explicit:
    (a) **VUMAT SE**
    (b) **VUMAT DL**

7.1 Material Selection

This chapter has the objective of clarifying the selection of composite material systems that are suitable to be used in the evaluation and validation of the numerical model under development.

This selection process requires that extensive experimental data about these materials is available in the literature and that all the required properties for their use are accessible or able to be inferred through reasonable engineering assumptions.

The AS4/PEEK material system was chosen given the experimental procedures done by Lachaud [59] and the material properties supplied by Liu et al. [88]. The data presented in Table 7.1 was then used in the numerical simulations.

Table 7.1: AS4/PEEK material properties.

Property	**Lachaud** [59]	**Liu et al.** [88]	**Calculated**	**Assumed**	**Used**
E_{11} [MPa]	143463.8	127000	-	-	143463.8
E_{22} [MPa]	9417.56	10300	-	-	9417.56
E_{33} [MPa]	-	10300	-	9417.56	9417.56
G_{12} [MPa]	5794.4	5700	6457.318	-	6457.318
G_{13} [MPa]	-	5700	-	7642.141	7642.141
G_{23} [MPa]	-	-	-	3700	3700
ν_{12}	0.297	0.3	-	-	0.297
ν_{13}	-	0.3	-	0.297	0.297
ν_{23}	-	-	-	0.45	0.45
ε_{11}^{ft}	0.01072	-	-	-	0.01072
ε_{22}^{ft}	0.00997	-	-	-	0.00997
ε_{33}^{ft}	-	-	-	0.00997	0.00997
ε_{11}^{fc}	0.00836	-	-	-	0.00836
ε_{22}^{fc}	0.00637	-	-	-	0.00637
ε_{33}^{fc}	0.00637	-	-	-	0.00637
γ_{12}^{s}	0.195	-	-	-	0.195
γ_{13}^{s}	-	-	-	0.195	0.195
γ_{23}^{s}	-	-	-	0.195	0.195
X_T [MPa]	1601.74	2070	-	-	1601.74
X_C [MPa]	-	1360	-	-	954.6
Y_T [MPa]	80.78	85	-	-	80.78
Y_C [MPa]	-	276	-	-	205.9
S_L [MPa]	164.6	186	-	-	164.6
S_T [MPa]	-	186	-	-	72.7
α_0 [°]	-	-	-	53	53
η_L	-	-	0.608	-	0.608
β	-	-	-	4.72E-08	4.72E-08
G_{Ic}^{ft} [N/mm]	-	218	-	-	218
G_{Ic}^{fc} [N/mm]	-	104	-	-	104
G_{Ic}^{mt} [N/mm]	-	1.7	-	-	1.7
G_{Ic}^{mc} [N/mm]	-	2	-	-	2
G_{Ic}^{ms} [N/mm]	-	2	-	-	2
G_{Ic} [N/mm]	1.156	1.7	-	-	1.156
G_{IIc} [N/mm]	1.98	2	-	-	1.98
BK	-	1.09	-	-	-
t_{33}^{0} [MPa]	-	43	-	-	-
t_{31}^{0} [MPa]	-	50	-	-	-
t_{32}^{0} [MPa]	-	50	-	-	-
K [MPa/mm]	-	6.40E+05	-	-	-

7.2 Homogenized Representative Volume Element

In a first stage, a unit sized cube (1x1x1 mm) is used for testing the mechanical behaviour of the composite under fundamental load conditions. The use of a singular element is useful to corroborate the implementation of the behaviour established by the constitutive model in a low computational effort environment.

The previously described modeling strategies are employed. Nevertheless, the element type used is C3D8 in both Standard and Explicit formulations. The boundary conditions are controlled by two reference points connected to opposing faces of the RVE by means of kinematic coupling constraints whose degrees of freedom can be activated as deemed necessary. Generally, one of the reference points is pinned in the load direction whilst the other is prescribed a finite displacement following a determined amplitude (Figure 7.1).

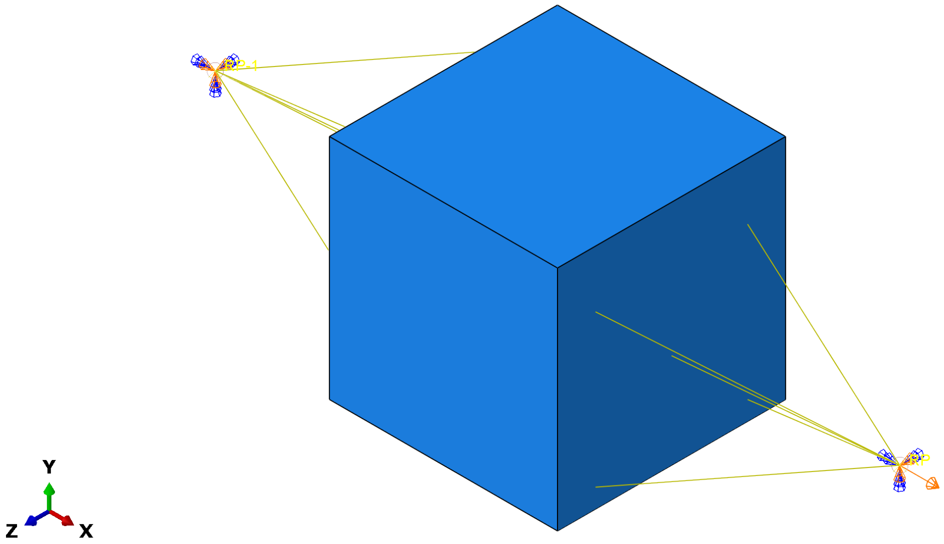

Figure 7.1: Representative volume element with corresponding constraints and boundary conditions.

The RVE will be used to validate the model in the longitudinal, transverse and shear stress states, which will be achieved by varying the layer / material orientation to the corresponding layup configuration. In order to obtain the data directly from what the model predicts and given that this elementary model converges easily, viscous regularization is disabled in Standard and no mass scaling is used in Explicit. The total number of outputs was set to 1000.

7.2.1 Longitudinal

This section pertains to simulations done with loading applied longitudinally, i.e. along the fiber axis, in continuous and cyclic tension and compression, and load reversal cases.

7.2.1.1 Tensile

A displacement of 1 mm was imposed resulting in the longitudinal stress-strain curve found on Figure 7.2. In order to assess if damage was behaving as intended, that is, not reducing when the stress state is outside the failure state, cyclic loading was employed with load interruption at determined stages.

Cyclic behaviour is shown in Figure 7.3a, where it is possible to verify gradual stiffness degradation, as the damage state evolves. Regarding that, as is verifiable in Figure 7.3b, the fiber failure damage does not diminish when load alleviation occurs, maintaining instead its current level until the stress state once again reaches the failure envelope.

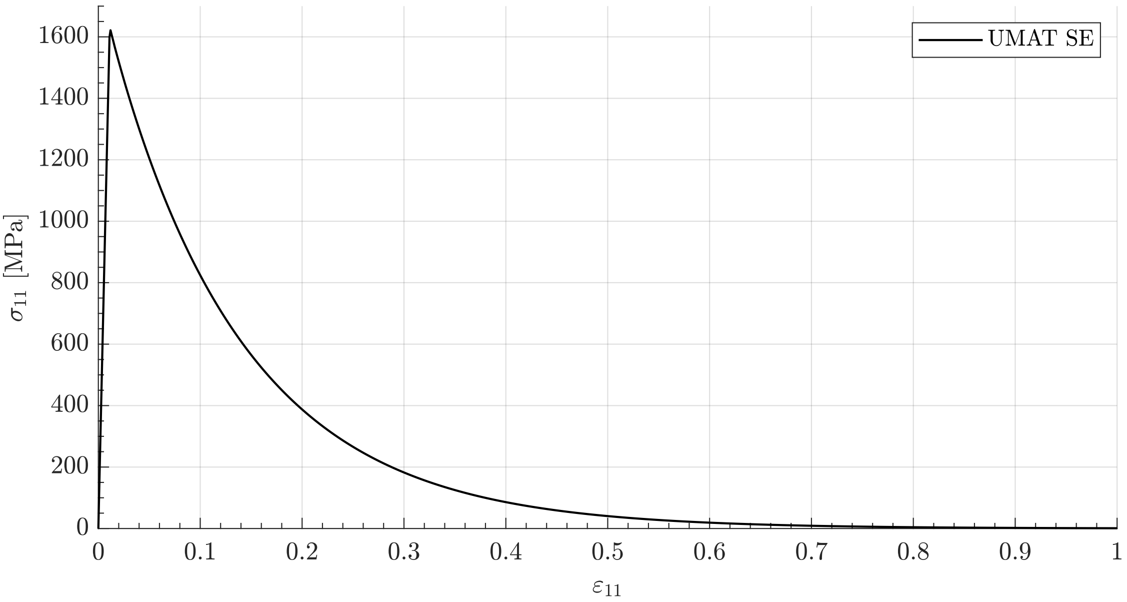

Figure 7.2: Longitudinal tensile stress strain response under monotonic loading.

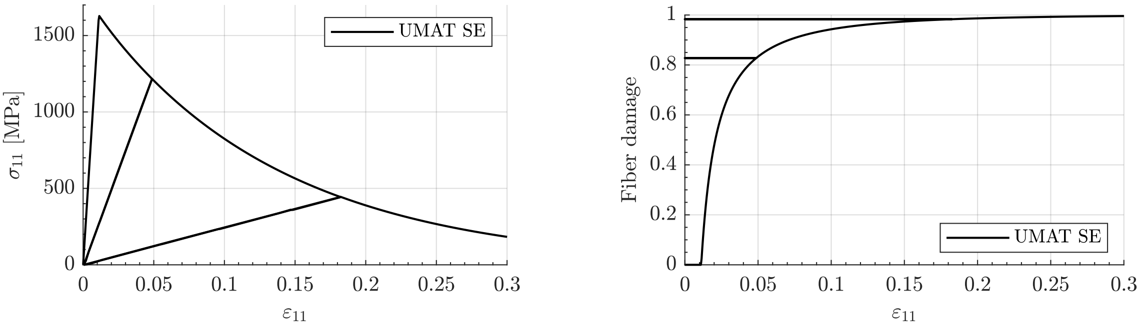

(a) **(b)**

Figure 7.3: Longitudinal tensile response under cyclic loading given by (a) stress strain curve and (b) fiber failure damage evolution.

7.2.1.2 Compressive

As expected, under compressive longitudinal loading, the material behaves in a similar fashion to that when under tensile loading, incurring in linear elastic behaviour before failure and then suffering an exponential type degradation, as is verifiable in Figure 7.4. Figure 7.5 illustrates cyclic compressive loading and its respective fibre failure damage evolution, which remains constant under load alleviation.

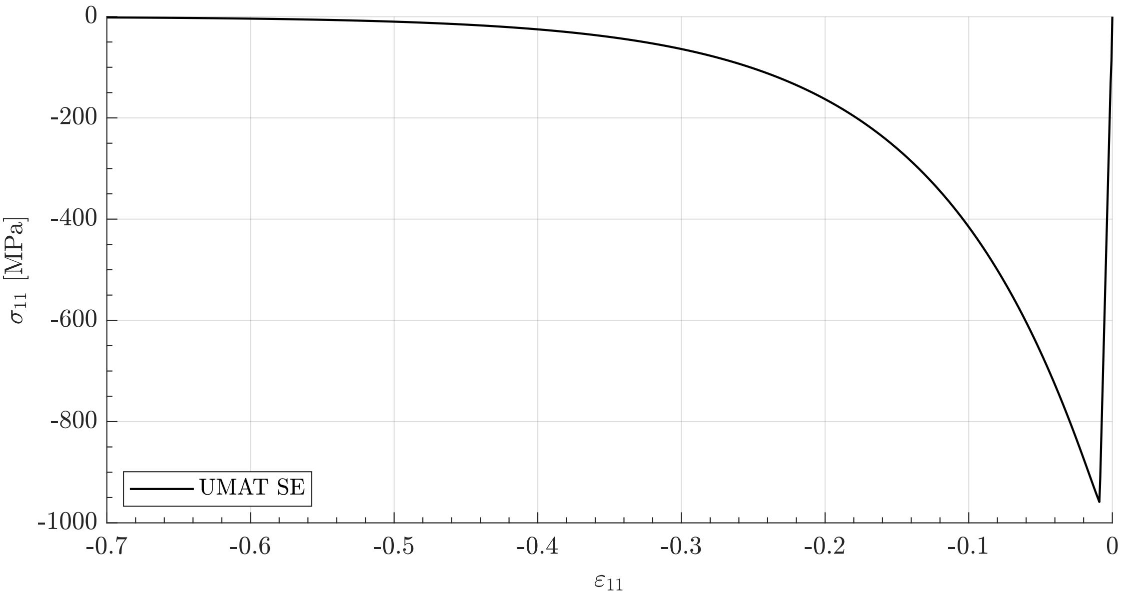

Figure 7.4: Longitudinal compressive stress strain under monotonic loading.

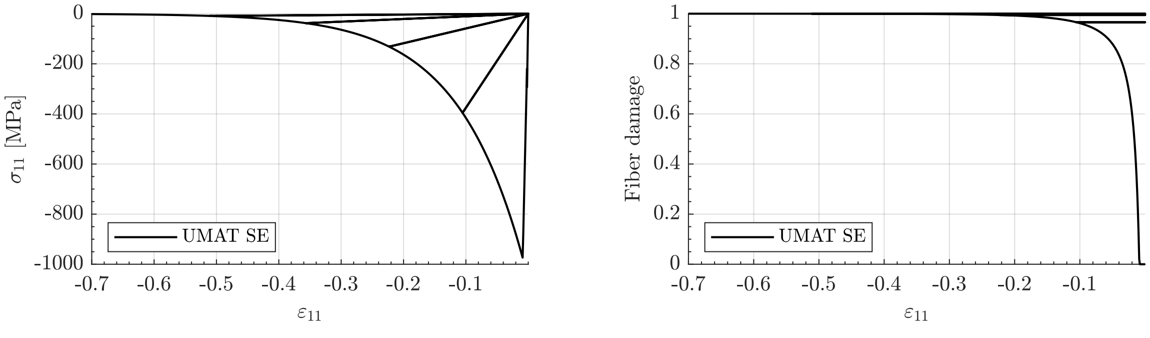

(a) **(b)**

Figure 7.5: Longitudinal compressive response under cyclic loading given by (a) stress strain curve and (b) fiber failure damage evolution.

7.2.1.3 Load reversal

Under longitudinal cyclic tension-compression loading, damage is cumulative and transferable from one failure mode to the other, i.e. the damage incurred during compression has effect on the behaviour under tensile loading, and vice-versa, as observed in Figure 7.6.

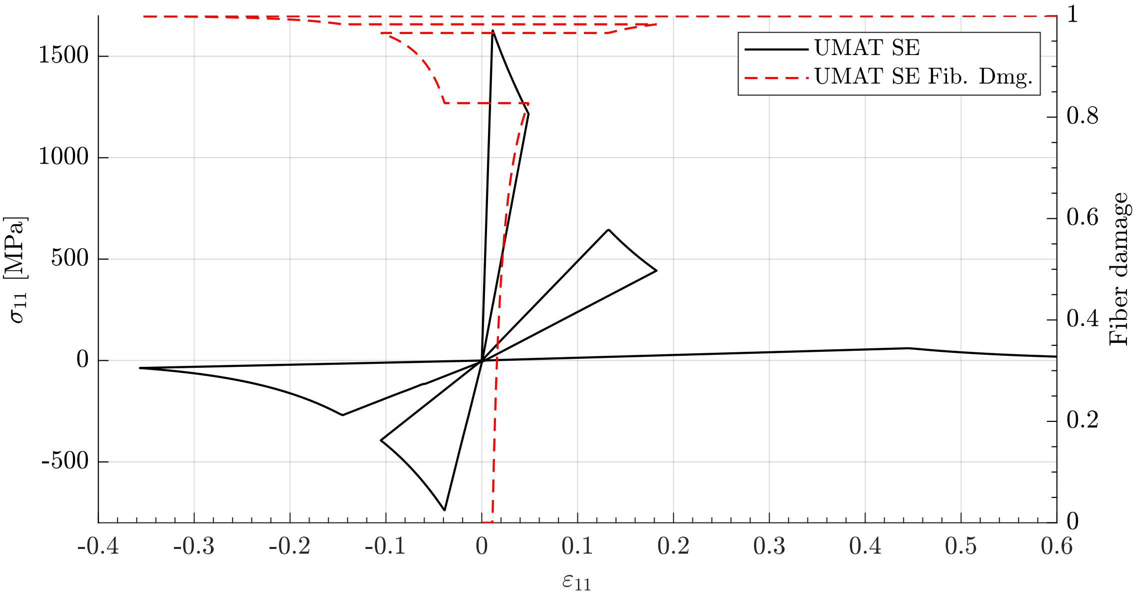

Figure 7.6: Longitudinal cyclic tension-compression stress strain response and fiber damage evolution.

7.2.2 Transverse

Considering now loading in the transverse direction the material orientation was rotated by 90° and the same approach was taken as for the longitudinal direction, evaluating the behaviour of the material under tensile and compressive monotonic and cyclic loading, and under load reversal solicitation.

7.2.2.1 Tensile

The transverse behaviour under monotonic loading can be seen in Figure 7.7, where a non-linear stage can be spotted before failure occurs. This is the effect of plasticity and diffuse damage, which can be observed in Figure 7.8a, where the curve, upon unloading returns to a strain value larger than zero, and in Figure 7.8b where it is possible to observe the development of diffuse damage. In the latter, the line corresponding to the value of diffuse damage returns several times to zero. That is due to the nullification of damage when the matrix enters the compressive domain, i.e. $\varepsilon_{22}^{e} < 0$.

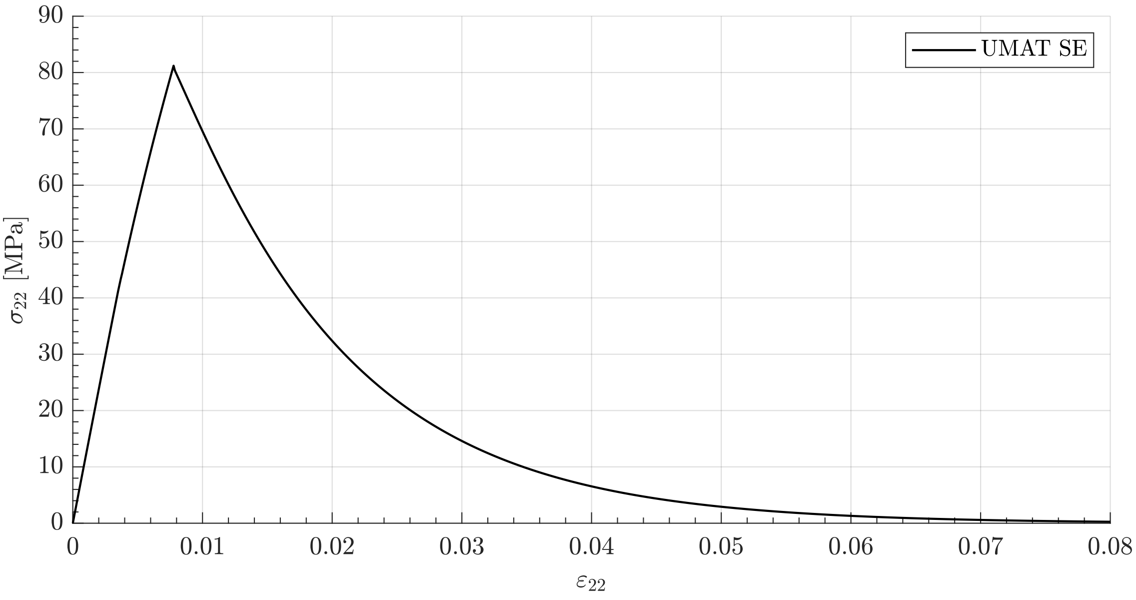

Figure 7.7: Transverse tensile stress strain under monotonic loading.

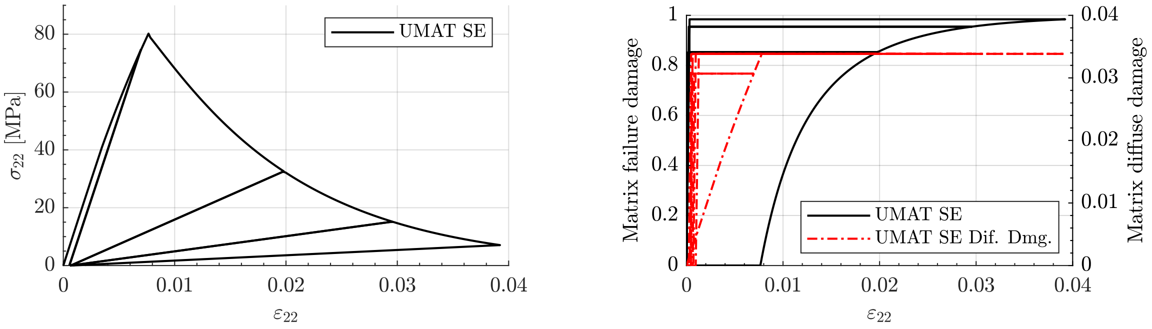

(a) **(b)**

Figure 7.8: Transverse tensile response under cyclic loading given by (a) stress strain curve and (b) matrix diffuse and failure damage evolution.

7.2.2.2 Compressive

The behaviour under compressive loading was not modeled to present either plasticity nor diffuse damage and it should therefore be similar to that of the longitudinal domain. However, as can be verified on Figure 7.9, the stress strain curve after failure does not present the exponential decay that it is supposed to have. Upon further analysis, it is verified that the compressive kinking failure mode was activated and the matrix started prematurely taking damage from it. Once compressive kinking failure stops being the governing mode, the stress strain response returns to the expected exponential evolution.

Checking the state of the element at the time when failure began gave some insights as to why this is occurring. It can be verified in Figure 7.10 that spurious unsymmetric

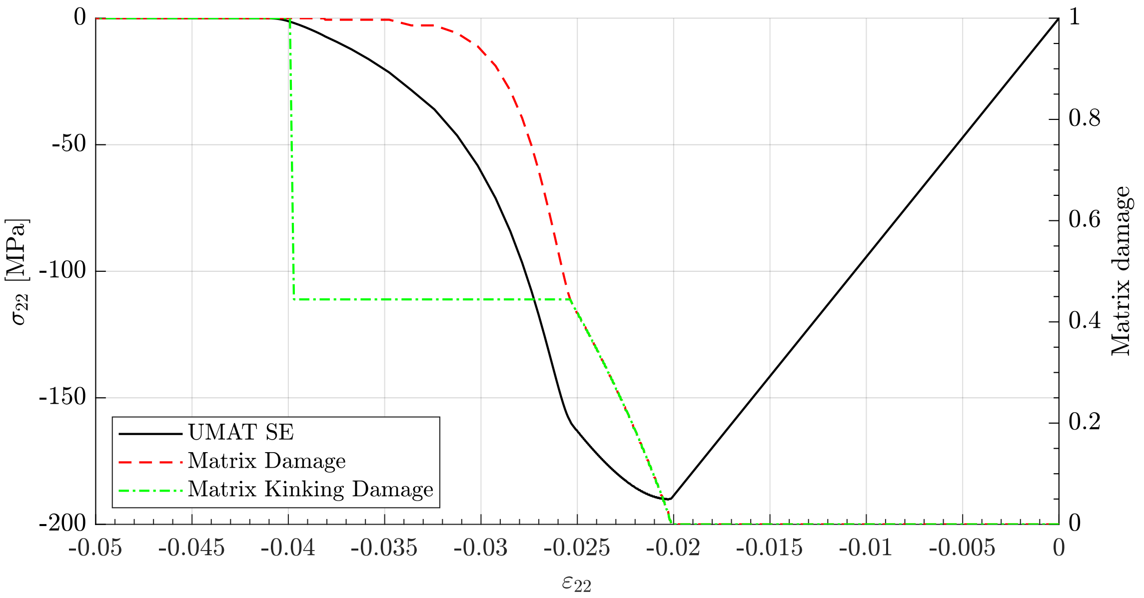

Figure 7.9: Transverse compressive stress strain under monotonic loading.

deformation of the element took place, transitioning the stress state from purely compressive to a more complex one, which ended up incurring in matrix compression failure in the fiber kinking misalignment frame.

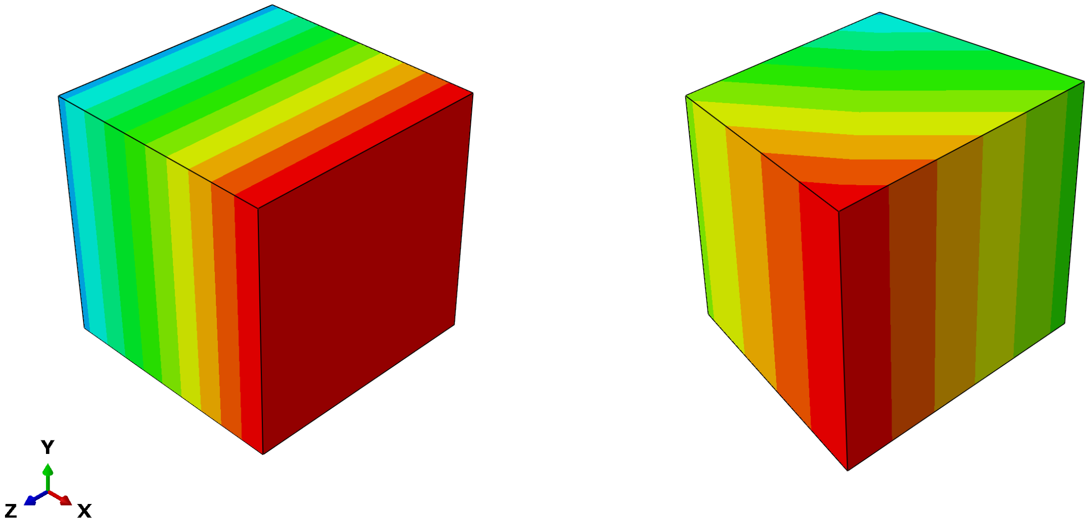

Figure 7.10: Normal element deformation amplitude under compressive loading (left) and observed element deformation amplitude which incurred in kinking matrix compression failure (right).

In order to obtain the compressive behaviour isolated from boundary conditions that might induce those deformations, it was decided to switch from a single element RVE to one meshed with elements of 0.2 mm in size. This resulted in the updated stress strain curve visible in Figure 7.11, where the evolution of matrix damage corresponds to what is expected.

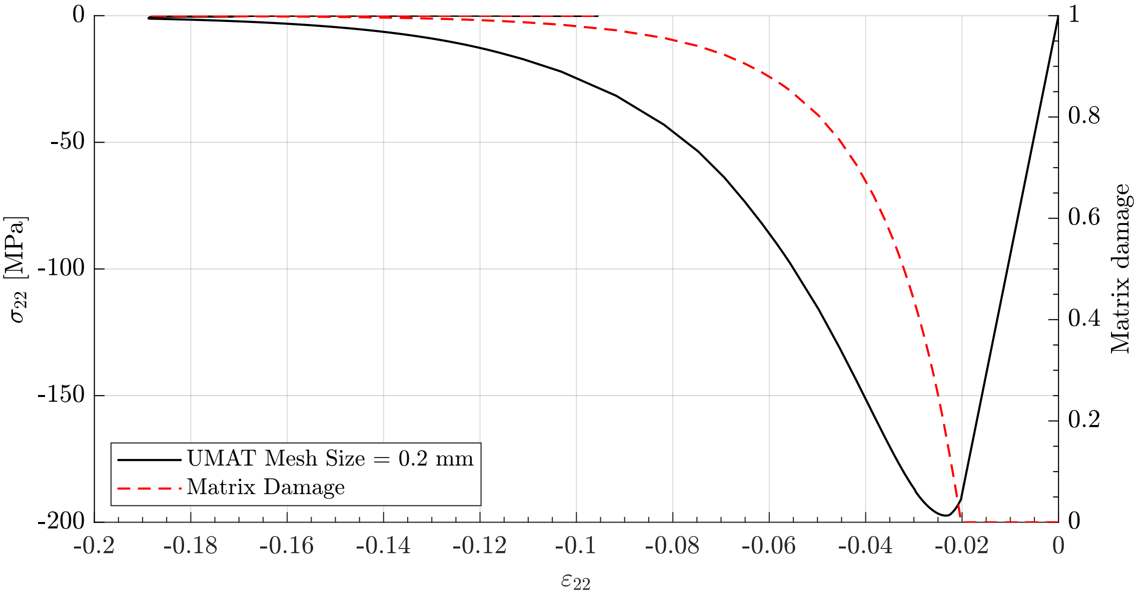

Figure 7.11: Transverse compressive stress strain curve using a 0.2 mm mesh size in the RVE.

Unexpectedly, the cyclic compression simulation with the single element RVE did not present the same spurious phenomena as the monotonic loading one, with the damage and stress strain response evolving according to what was projected, as can be verified in Figure 7.12.

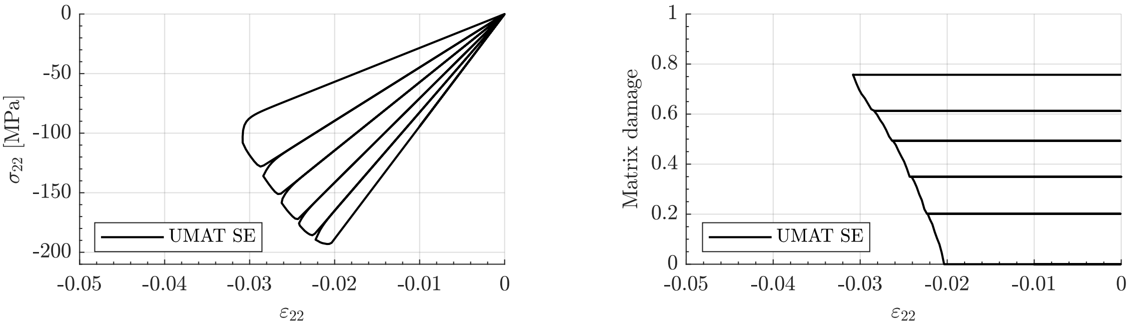

(a) **(b)**

Figure 7.12: Transverse compressive response under cyclic loading given by (a) stress strain curve and (b) failure damage evolution.

7.2.2.3 Load reversal

Cyclic transverse tension and compression, leads to the stress strain and matrix damage evolution curves of Figure 7.13, where it can be observed the accumulation of damage in the tensile domain, being additive with the compression originated damage. Thus, even after the material has completely failed in tension, if it is displaced in the sense of compression, it still retains stiffness pertaining to that mode.

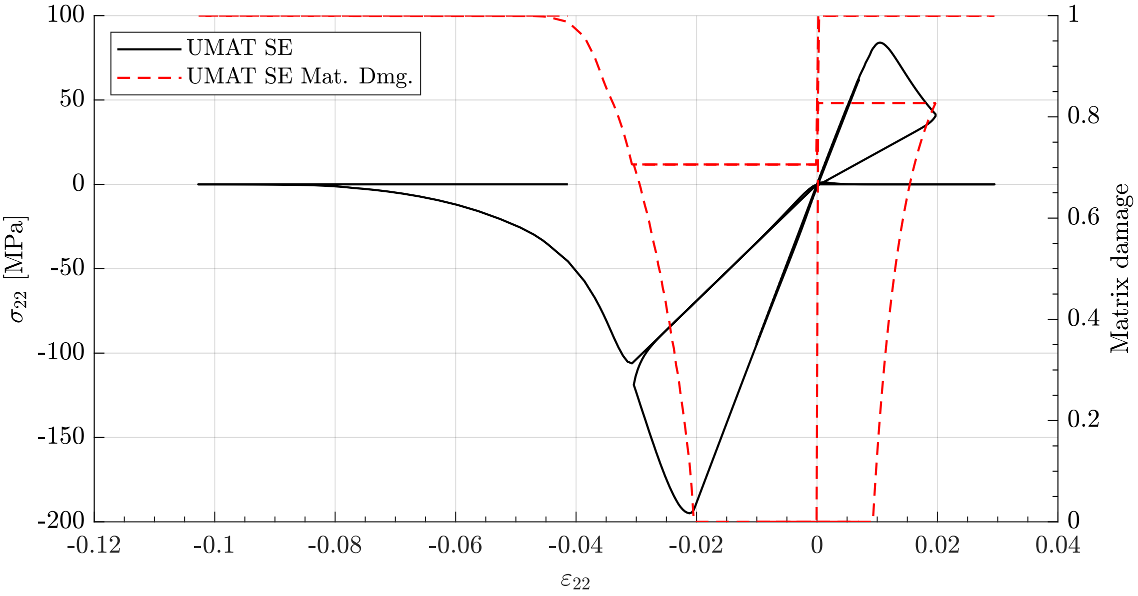

Figure 7.13: Transverse cyclic tension-compression stress strain response and matrix damage evolution.

Given the unnatural transition of damage between the tensile and compressive domains and the possibility that such an abrupt variation might lead to local instabilities in the solver, smooth damage activation functions are proposed, in a similar concept to what viscous regularization accomplishes but with control over the damage convergence rate.

Damage deactivation function - tension to compression: Passing from a tensile domain to a compressive one entails that the damage attained due to tension loads is neutralized by crack closing phenomena and the only damage that is sustained is the previously gained under compression.

$$d_f = (d_f^{mt} + d_f^{mc}) + k_c(d_f - d_f^{mc})(\varepsilon_{22}^e)^3 \tag{7.1}$$

where k_c is expressed as:

$$k_c = \frac{(d_f^{mt} + d_f^{mc}) - d}{-\varepsilon^3(d_f^{mc} - d)} \tag{7.2}$$

and where d and ε are the control variables stating how much damage has to have occurred by a certain strain. These should be used in relation to explicit properties, e.g. $d = 1.1d_f^{mc}$

and $\varepsilon = 0.9\varepsilon_{22}^{fc}$, especially the damage variable, since $d \in]d_f^{mc}, d_f^{mc} + d_f^{mt}[$. The specified function can then be observed in Figure 7.14.

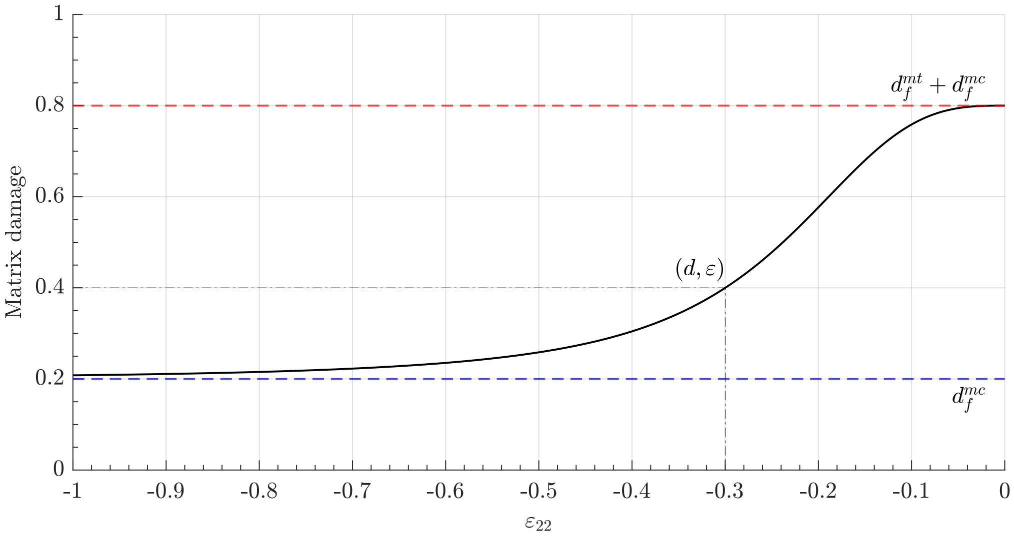

Figure 7.14: Damage deactivation function when entering compressive loading with rate of convergence controlled by parameters $d = 0.4$ and $\varepsilon = 0.3$.

Damage activation function - compression to tension: When going from compression to tension, the inverse behaviour is desired, that is, the compressive damage will effect tensile behaviour. Thus, the activation function is expressed in Equation 7.3 and illustrated in Figure 7.15.

$$d_f = d_f^{mc} - k_t(d_f - (d_f^{mt} + d_f^{mc}))(\varepsilon_{22}^{e})^3 \tag{7.3}$$

where k_t is given by:

$$k_t = \frac{d - d_f^{mc}}{\varepsilon^3((d_f^{mt} + d_f^{mc}) - d)} \tag{7.4}$$

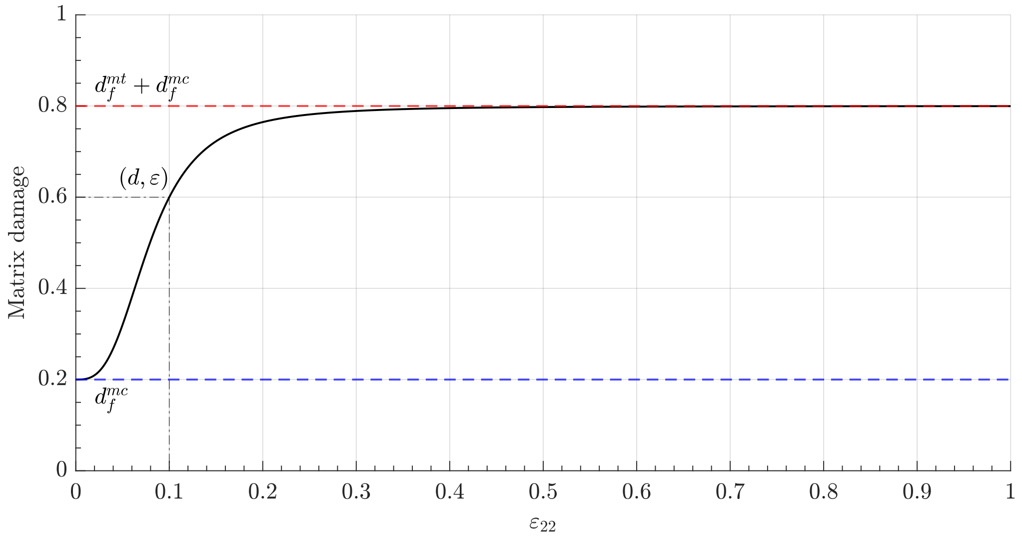

Figure 7.15: Damage activation function when entering tensile loading with rate of convergence controlled by parameters $d = 0.6$ and $\varepsilon = 0.1$.

7.2.3 In-plane shear

It is under in-plane shear that the greatest development of plasticity and diffuse damage is observed, allowing for the verification of the return mapping algorithm and the diffuse damage and plasticity evolution laws. Furthermore, by employing a composite layup with differently oriented layers, it is possible to validate the fiber rotation feature of the subroutines. Therefore, the modeling strategy adopted for validation under shear loading switched from using a single element RVE representing a unidirectional ply to a multi-layered one, portraying a multi-directional laminate in its simplest form. Figure 7.16 showcases this approach.

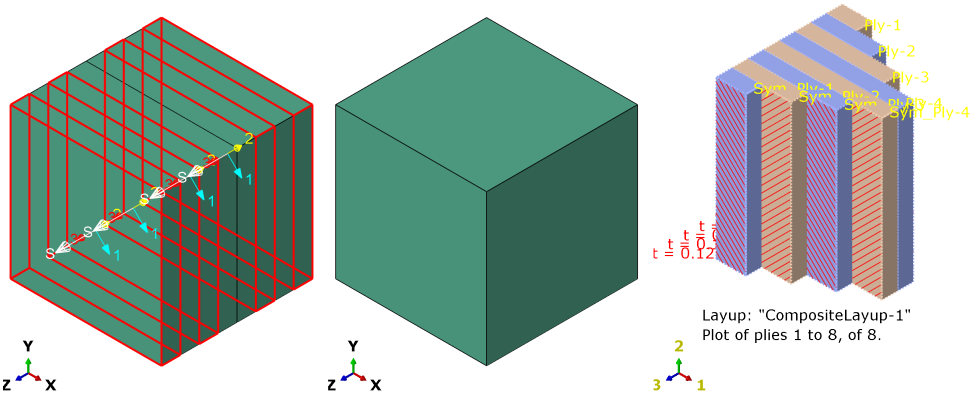

Figure 7.16: RVE modelling strategies. (left) Discrete laminate with highlighted (−45) layers, (middle) continuous laminate and (right) ply stack plot of the continuous laminate.

7.2.3.1 Tensile

In a similar fashion to what was done for longitudinal and transverse orientations, monotonic and cyclic loading will be simulated. Continuous loading, found in Figure 7.17 confirms that the characteristically high shear strain and the increase in stress due to fiber rotation are successfully simulated by the material model.

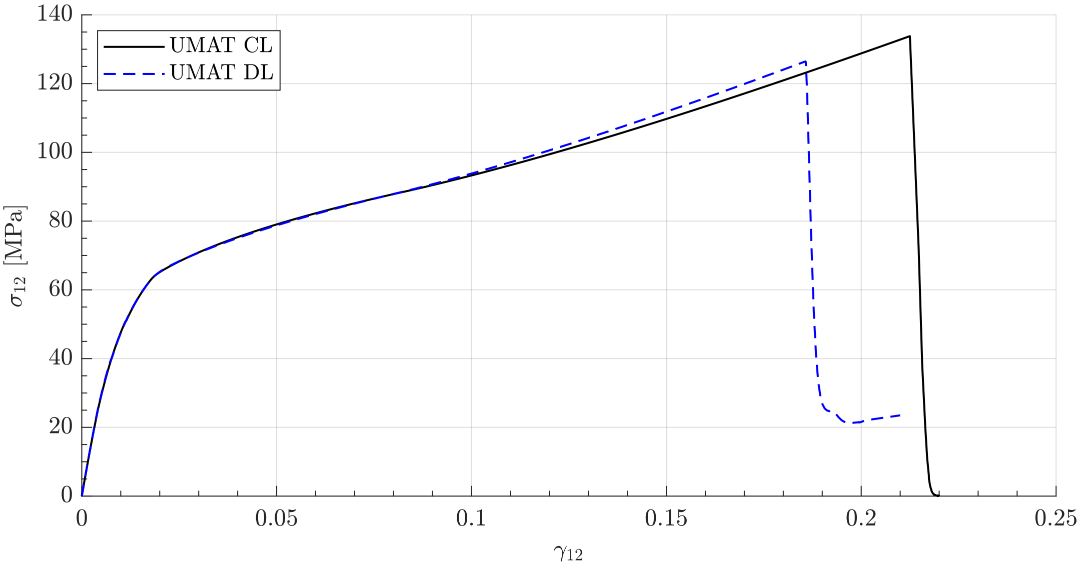

Figure 7.17: In-plane tensile shear stress strain under monotonic loading.

Furthermore, under cyclic solicitation, it is possible to observe in Figure 7.18a the development of diffuse damage, through the noticeable decrease in the slope of the load alleviation regions, indicating degradation of the shear stiffness, as well as the development of significant plastic strains. Figure 7.18b illustrates the successful application of the shear diffuse damage laws and, in Figure 7.18c, the implementation of plasticity with the return mapping algorithm controlling the value of the plastic yield function (Figure 7.18d), successfully obeying the consistency condition $F_p \leq 0$.

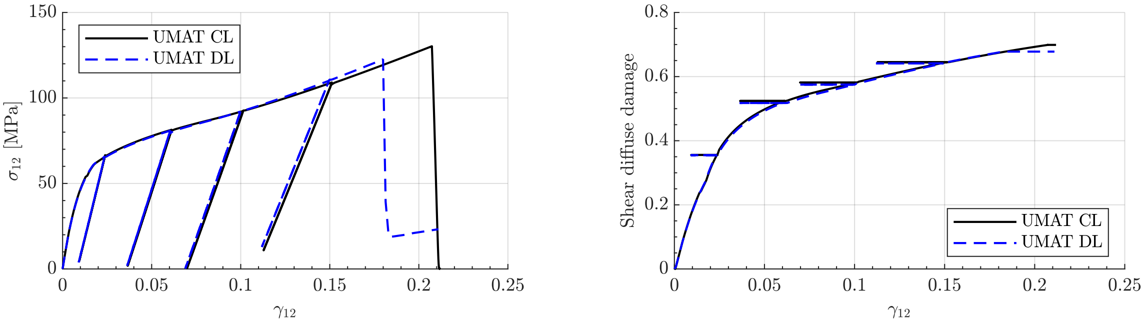

(a)

(b)

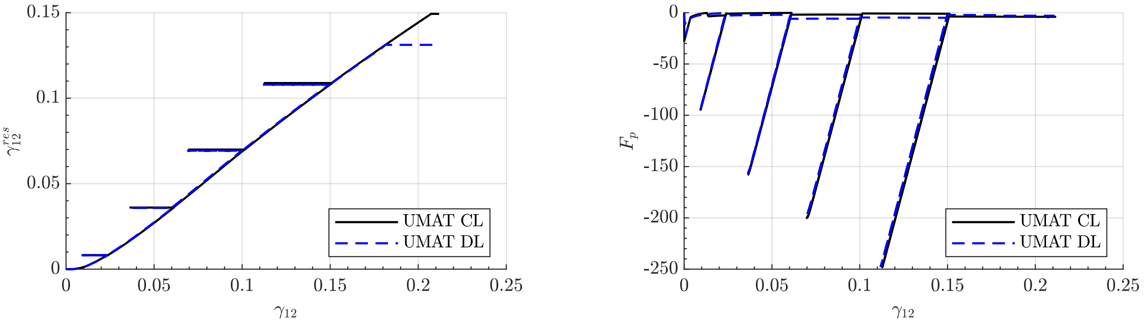

(c) **(d)**

Figure 7.18: In-plane shear response under cyclic loading given by (a) stress strain curve, (b) diffuse damage evolution, (c) plastic strain evolution and (d) plastic yield function.

7.2.4 Result Comparison

Assessing the values at which failure occurred and the respective fracture toughnesses originated by the evolution of the failure damage, the values resulting from the UMAT are given in Table 7.2.

Table 7.2: Experimental strength and fracture energies versus obtained results, for the UMAT formulation.

Property	**Experimental**	**Obtained** (Error)
X_T [MPa]	1601.74	1621.48 (1.23%)
G_{Ic}^{ft} [N/mm]	218	218.16 (0.07 %)
X_C [MPa]	954.6	958.66 (0.42%)
G_{Ic}^{fc} [N/mm]	104	103.66 (0.33 %)
Y_T [MPa]	80.78	80.72 (0.07%)
G_{Ic}^{mt} [N/mm]	1.156	1.11 (3.98 %)
Y_C [MPa]	205.9	197.38 (4.14 %)
G_{Ic}^{mc} [N/mm]	1.98	2.04 (3.03 %)
S_L [MPa]	164.6	133.81 (18.58 %)

7.3 Coupons

In order to better validate the subroutines, it was deemed appropriate to test them in scenarios closer to the real world. Therefore, coupons similar to those used to characterize composites in what is the first step in the building block approach were simulated.

Mesh size was considered according to the notion that a local snap-back must not exist in the stress-strain relation, .i.e. the elastic energy at the onset of localization must be equal or lower than the fracture energy [76], hence:

$$l^* \leq \frac{2E_M G_M}{X_M^2} \tag{7.5}$$

where M represents each damage law ($M = \pm 1 \vee M = \pm 2$).

Tensile specimens based on the standard test method ASTM D3039 [89] and compression specimens based on the work of Gohorianu [90] were simulated.

7.3.1 Tensile Specimen

Longitudinal, transverse and in-plane shear tests were simulated. The results of these tests will be compared with experimental data obtained by Lachaud [59], for the AS4/PEEK composite. The dimensions of the models are presented in Figures B.1, B.2 and B.4 for the tensile (also shown in Figure 7.19 in the model form), in-plane shear and transverse specimens, respectively. UMAT CL, UMAT DL and VUMAT DL modeling strategies were employed. Following a mesh convergence study, and ensuring that the condition of Equation 7.5 is fulfilled, an approximate global element size of 4mm was employed.

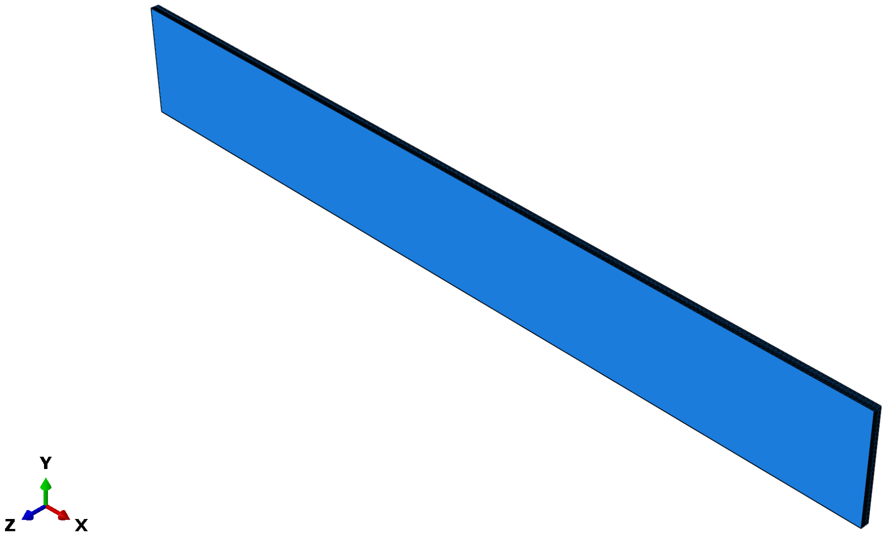

Figure 7.19: Longitudinal tensile specimen.

7.3.1.1 Longitudinal

The tensile specimen was displaced 1.8 mm until failure occurred resulting in the stress strain response found in Figure 7.20.

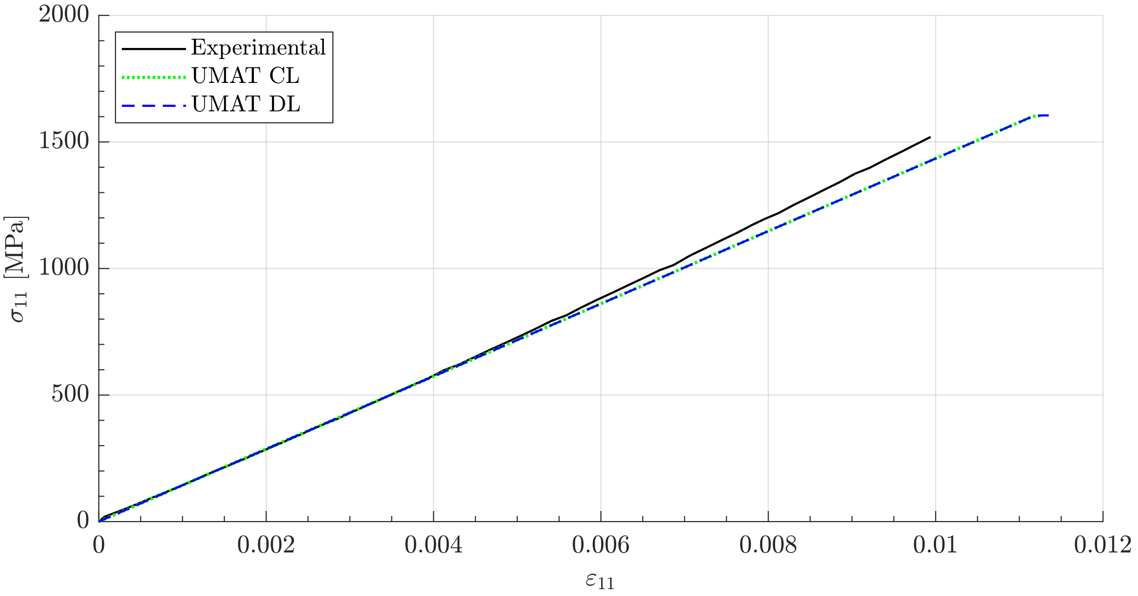

Figure 7.20: Simulation of longitudinal tension applied on a $[0]_8$ specimen compared with experimental data.

Although the experimental curve deviates slightly from the linear elastic type curve of the simulation, due to unaccounted for hardening phenomena, and indicates failure before the simulation does, good results are considered to have been achieved. This is because the inputted material properties indicated a maximum strength X_T of 1601.74 MPa and a maximum stress of 1603.99 MPa in the UMAT CL and 1604.94 MPa in the UMAT DL were achieved.

7.3.1.2 Transverse

Regarding the transverse tension simulations, whose stress strain curves can be found in Figure 7.21, the ones resulting from the UMAT presented close similarity to what was observed experimentally, with diffuse damage and plasticity evolutions matching the experimental ones. Regarding the curve resulting from the VUMAT, it did not coincide with the developed material model, given that its implementation was not completed, as stated in Section 6.3.

Notably, the comparison between the UMAT and VUMAT showcases the effect of using a correct three-dimensional formulation for plasticity. Whilst the VUMAT presented the same plasticity and diffuse damage evolution laws, plasticity was only influenced by shear and transverse stress components, resulting in loss of information given by the other directions and a less than optimal solution.

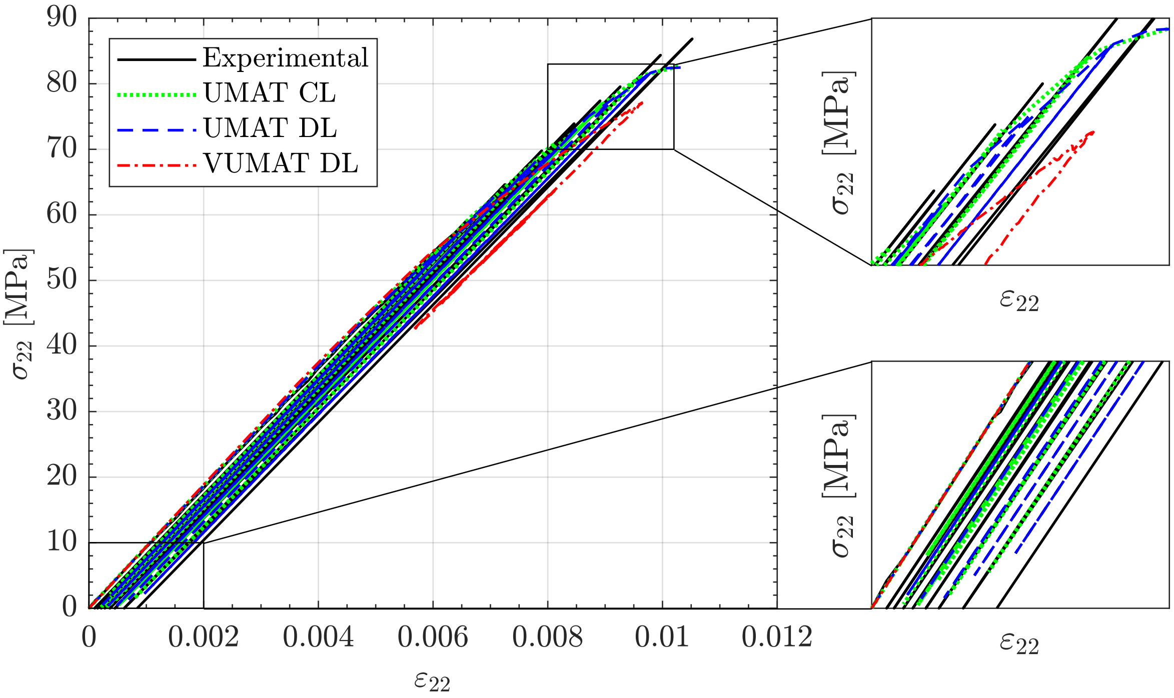

Figure 7.21: Simulation results of transverse cyclic tension applied on a $[90]_8$ specimen compared with experimental data.

In terms of strength of the specimen, the UMAT CL coupon failed at 80.80 MPa while the UMAT DL failed at 80.27 MPa, in relation to an experimental value of 80.78 MPa. It is possible to verify in Figure 7.22 the damage incurred by transverse tension, distributed across the specimen.

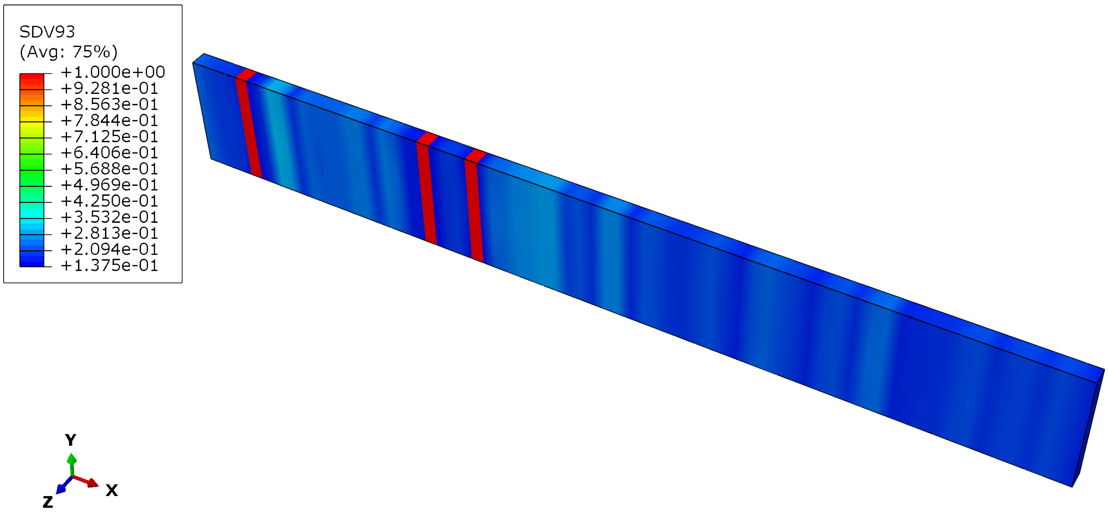

Figure 7.22: Tensile matrix damage distribution across the transverse tensile test specimen.

7.3.1.3 In-plane shear

The results from the UMAT in-plane shear test were remarkably positive, as can be verified in Figure 7.23. A cyclic displacement was applied, as to mimic the experimental solicitations, unveiling the diffuse damage and plasticity evolution as the test progressed. Both the CL and DL modeling strategies had similar behaviours, with the plastic strain and diffuse damage developing as they did in the experimental test.

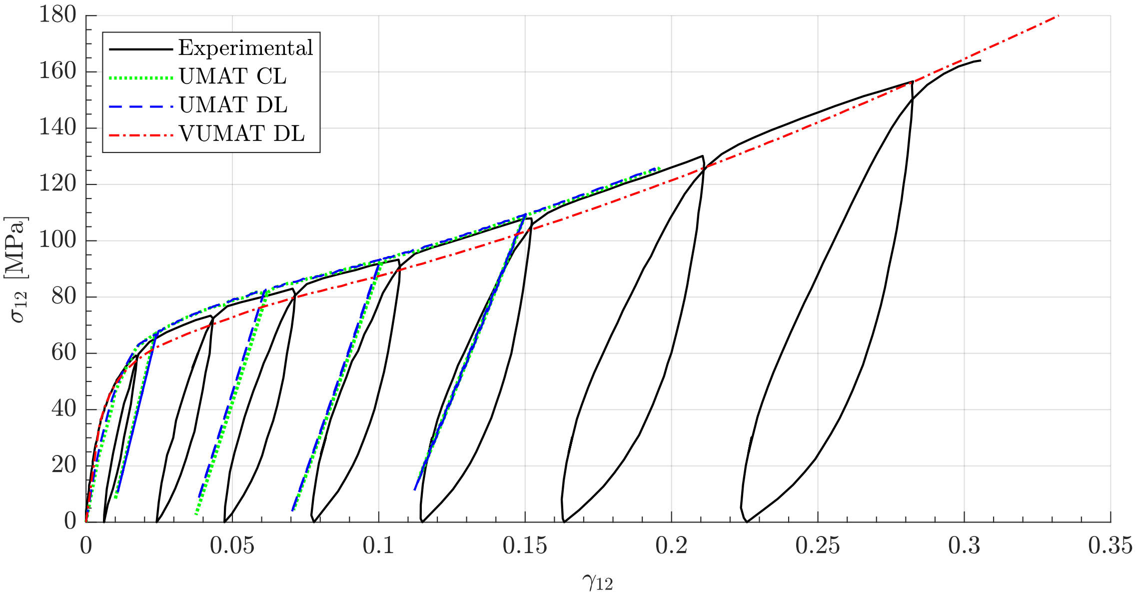

Figure 7.23: Simulation of in-plane cyclic shear tension applied on a $[\pm 45]_{2S}$ specimen compared with experimental data.

An aspect that needs to be improved is the determination of failure, which happens prematurely. Nevertheless, it is important to mention that *in situ* effects were not considered in this simulation despite being implemented in the model. These could prove to be the key to achieving the correct shear strength.

Regarding the VUMAT, despite having an incomplete implementation, its behaviour is similar to that of the experimental one, as it was in the transverse solicitation. Failure was disabled for this test given that the VUMAT's implemented failure criteria used the Linde formulation, resulting in extremely premature failure of the matrix under this type of solicitation.

7.3.2 Compression Specimen

The dog-bone geometry, developed by Gohorianu [90] was used in the compression specimen, instead of the one proposed in ASTM D3410 [91] due to not requiring a specific mounting to carry out the tests and also because this design allows the least over-stress in the central rectangular gauge section. The dimensions of this specimen can be found on

Figures B.5 and B.6 for the longitudinal and transverse cases, respectively and the model used for the simulations can be found in Figure 7.24. Following a mesh convergence study and taking into account the localization of stress in the center region of the specimen, a 2 mm mesh with gradual decrease to 0.6 mm in the center region was implemented.

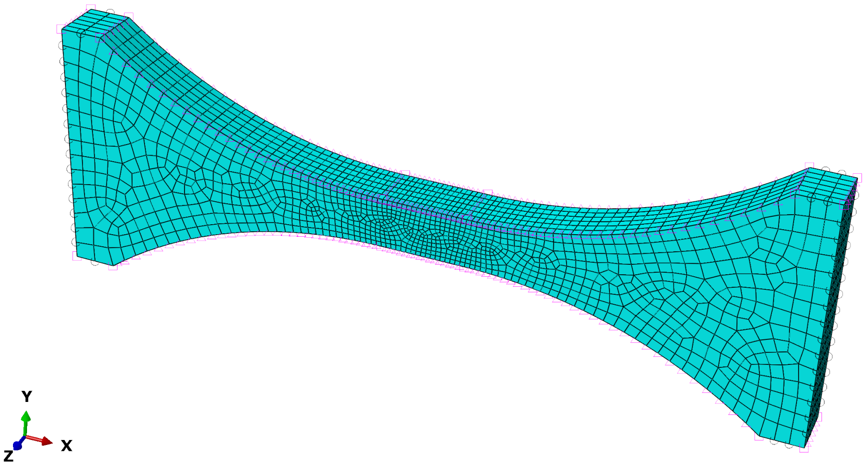

Figure 7.24: Compressive "dog-bone" specimen with biased mesh configuration.

7.3.2.1 Longitudinal

Considering the cross-sectional area of the specimen (37.536 mm^2), the maximum compressive stress reached in the simulation is given as 963.96 MPa, in relation to a compressive strength of 954.6 MPa. In the later stages, after the onset of failure, it is possible to observe buckling occurring in the specimen (Figure 7.25), leading to the increase of the slope of the curve in the force displacement graph given in Figure 7.26.

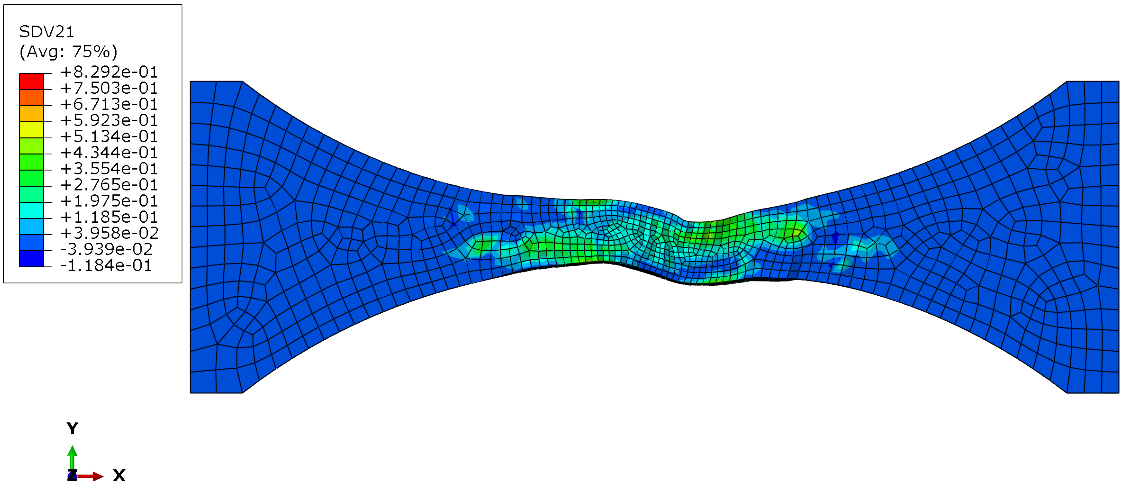

Figure 7.25: Fiber damage distribution across the longitudinal compressive test specimen.

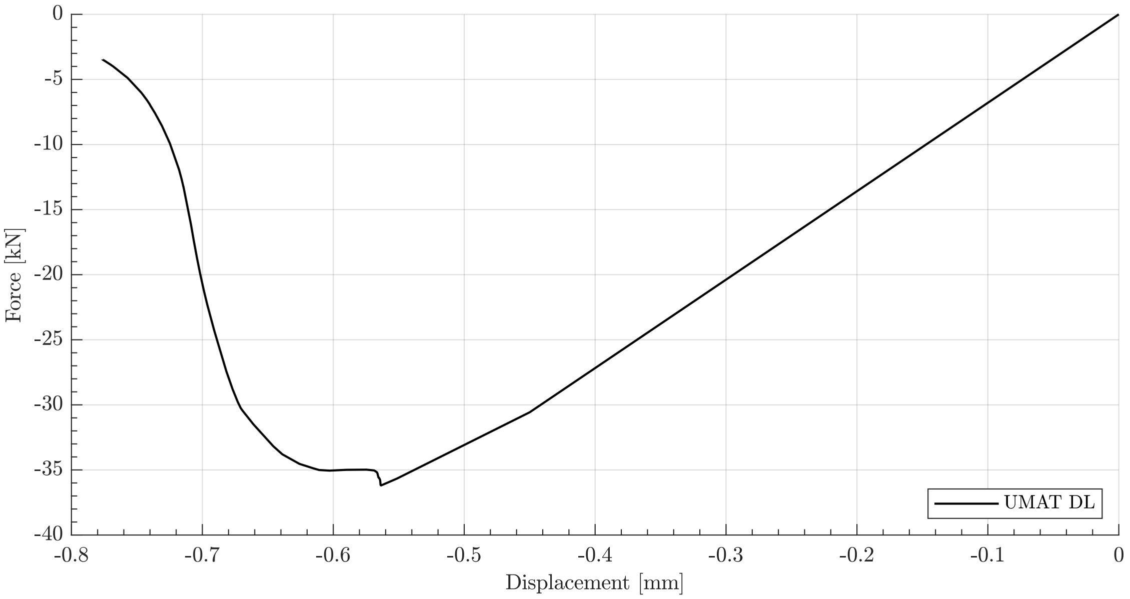

Figure 7.26: Force displacement curve for longitudinal compressive loading.

7.3.2.2 Transverse

In the case of transverse compression, the occurrence of the plateauing region is even more apparent, as the simulation was able to achieve higher post-failure displacements (Figure 7.27). In this scenario, the specimen withstood a maximum of 236.4 MPa of compressive stress, versus a strength of 205.9 MPa, having relatively good accuracy. It is noteworthy to mention that in the linear elastic region, the increment size was large, which might have lead to an overstep in this regard, resulting in larger values of failure stress.

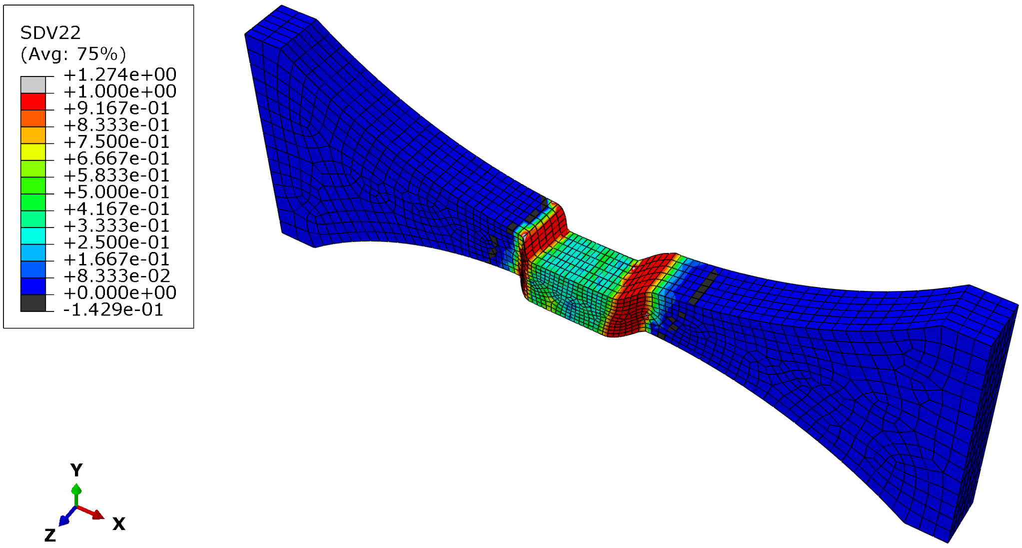

Figure 7.27: Matrix compressive damage distribution across the transverse compressive test specimen.

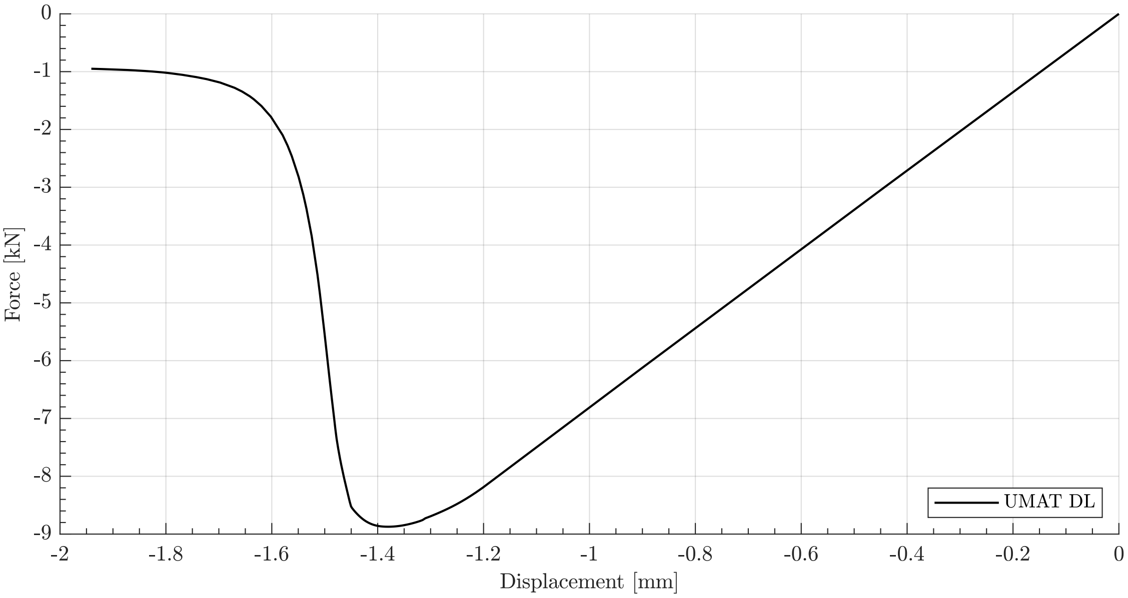

Figure 7.28: Force displacement curve for transverse compressive loading.

Part V

Final Considerations

Chapter 8

Conclusion

The aim of the work developed in this dissertation was to develop a constitutive model that accurately characterizes the intra-ply behaviour of thermoplastic composites and laying the foundation for further improvements that will lead to the development of a static and dynamic material model for intra and inter-ply behaviour. To this effect, UMAT and VUMAT subroutines were developed and employed in the Abaqus commercial finite element solver.

Broad literature research was conducted to select the most appropriate modules of the constitutive model, leading to the inclusion of diffuse damage, plasticity, fiber rotation, *in situ* effect, failure criteria and failure damage features. Unfortunately, not all of these were able to be implemented in the VUMAT, as the main development focus lied within the UMAT.

In order to verify the viability of the model, RVE-based simple load tests were done, in order to check the model's behaviour under longitudinal, transverse and shear tensile and compressive loading. Cyclic and alternating loading was also verified, with the objective of including all possible alternatives that might occur under a real loading scenario.

Standard tensile specimens were then simulated and compared with experimental results, with the complete UMAT achieving accurate results in the longitudinal, transverse and in-plane shear load configurations, proving the effectiveness of the model in that domain. Compressive test specimens were also tested, proving the occurrence of expected buckling phenomena but not being able to verify quantitatively the accuracy of the simulation.

In essence, the constitutive model was developed successfully for the static intra-ply behaviour of thermoplastic composites, with partial experimental validation via comparison with AS4/PEEK tests found in the literature. Although the VUMAT was not completely developed to the same level of detail as the UMAT, it still constituted an important step to the end goal of producing a dynamic-based model.

8.1 Future Works

In order to improve the work that has been done, the first step should be to complete the VUMAT, bringing it up to the standard of the UMAT. Following this, the inclusion of strain-rate effects is apparent, as well as the addition of inter-ply behaviour, either through the use of cohesive elements or by the development of a specific UMAT, VUMAT, UINTER or an additional module inside of the current subroutines, for the characterization of those elements, validated through the DCB, ENF, ILSS and L-Shape experimental tests.

Besides that, the inclusion of kinematic plasticity, allied with better convergence methods in the return-mapping algorithm could prove instrumental to better results and less computation time.

Finally, more tests in load scenarios of higher complexity, such as a bolted joint or impact simulations are necessary for a better validation of the model, with higher levels of the test pyramid also being extremely pertinent.

References

[1] Evergreen Aviation and Space Museum. *History of the Spruce Goose*. `https://www.evergreenmuseum.org/exhibit/the-spruce-goose/` [Accessed: (11/09/2023)]. 2021.

[2] Dana Parker. *Building Victory: Aircraft Manufacturing in the Los Angeles Area in World War II*. English. 2013.

[3] Slayter Games. *Method and apparatus for making glass wool*. U.S. Patent US2133235A, Nov. 1933.

[4] Dimitri Bettebghor, Stéphane Grihon, and Joseph Morlier. "Bilevel optimization of large composite structures based on lamination parameters and post-optimal sensitivities. Part 1: Theoretical aspects". In: *Structural and Multidisciplinary Optimization* (2018), p. 16.

[5] Sidney Goossens. "Barely visible impact damage detection in aerospace-grade carbon fibre reinforced polymer components with optical fibre sensors". PhD thesis. Vrije Universiteit Brussel, June 2021. DOI: `10.13140/RG.2.2.23149.05606`.

[6] Rebecca Slayton and Graham Spinardi. "Radical innovation in scaling up: Boeing's Dreamliner and the challenge of socio-technical transitions". In: *Technovation* 47 (Sept. 2015). DOI: `10.1016/j.technovation.2015.08.004`.

[7] Composites World. *Composites testing as part of a building block approach, Part 1: Coupon-level testing*. `https://www.compositesworld.com/articles/composites-testing-as-part-of-a-building-block-approach-part-1-coupon-level-testing` [Accessed: (11/09/2023)]. 2021.

[8] Clean Aviation. *Multi Functional Fuselage Demonstrator*. `https://www.clean-aviation.eu/multi-functional-fuselage-demonstrator` [Accessed: (11/09/2023)]. 2023.

[9] Composites World. *Clean Sky 2 OUTCOME project demonstrates PEEK thermoplastic composite wingbox cover*. `https://www.compositesworld.com/news/clean-sky-2-outcome-project-demonstrates-peek-thermoplastic-composite-wingbox-cover` [Accessed: (11/09/2023)]. 2023.

[10] Jaap Willem van Ingen et al. "Development of the Gulfstream G650 induction welded thermoplastic elevators and rudder". In: *SAMPE International Conference Exhibition*. May 2010.

[11] ISAE-SUPAERO. *ISAE-SUPAERO Website.* `https://www.isae-supaero.fr/en` [Accessed: (19/06/2023)]. 2022.

[12] I.M. Daniel and O. Ishai. *Engineering Mechanics of Composite Materials.* Vol. 1994. Oxford University Press New York, 2006. ISBN: 9780195150971.

[13] C. Zweben. *Mechanical Engineers' Handbook.* Vol. 1: Materials and Engineering Mechanics. Section 10: Composite Materials. Wiley Online Library, 2015. DOI: `https://doi.org/10.1002/9781118985960.meh110`.

[14] Waruna Seneviratne, John Waruna, and Brandon Saathoff. *Thermoplastic Joining Materials Guidance for Aircraft Design and Certification.* `https://www.wichita.edu/industry_and_defense/NIAR/Documents/jams-presentations-2021/Thermoplastic_Joining-Materials-Guidance-Seneviratne.pdf` [Accessed: (05/08/2023)]. 2021.

[15] Composites World. *PEEK vs. PEKK vs. PAEK and Continuous Compression Molding.* `https://www.compositesworld.com/articles/peek-vs-pekk-vs-paek-and-continuous-compression-molding` [Accessed: (12/09/2023)]. 2023.

[16] Ramesh Talreja and Chandra Veer Singh. *Damage and Failure of Composite Materials.* Chapter 3. Cambridge University Press, 2012. DOI: `10.1017/CBO9781139016063`.

[17] B. Budiansky and N.A. Fleck. "Compressive failure of fibre composites". In: *Journal of the Mechanics and Physics of Solids* 41.1 (1993), pp. 183–211. ISSN: 0022-5096. DOI: `https://doi.org/10.1016/0022-5096(93)90068-Q`. URL: `https://www.sciencedirect.com/science/article/pii/002250969390068Q`.

[18] Simon Skovsgård. "Failure of composite materials by kink band formation". PhD thesis. Institut for Ingeniørvidenskab, June 2019. DOI: `10.7146/aulsps-e.337`.

[19] Ole Thomsen and K.K. Kratmann. "Experimental Characterisation of Parameters Controlling the Compressive Failure of Pultruded Unidirectional Carbon Fibre Composites". In: *Applied Mechanics and Materials* 24-25 (June 2010), pp. 15–22. DOI: `10.4028/www.scientific.net/AMM.24-25.15`.

[20] B Walter Rosen. *Mechanics of Composite Strengthening: Fibre Composite Materials.* American Society of Metals, 1965.

[21] Ramesh Talreja. "Physical modelling of failure in composites". In: *Philosophical Transactions of the Royal Society A: Mathematical, Physical and Engineering Sciences* 374.2071 (2016), p. 20150280.

[22] BD Agarwal et al. *Analysis and performance of fiber composites Second edition.* John Wiley & Sons, 1990.

[23] Carlos González and Javier LLorca. "Mechanical behavior of unidirectional fiber-reinforced polymers under transverse compression: Microscopic mechanisms and modeling". In: *Composites Science and Technology* 67.13 (2007), pp. 2795–2806. ISSN: 0266-3538. DOI: `https://doi.org/10.1016/j.compscitech.2007.02.001`. URL: `https://www.sciencedirect.com/science/article/pii/S0266353807000711`.

[24] Olivia Redon. “Fatigue damage development and failure in unidirectional and angle-ply glass fibre/carbon fibre hybrid laminates”. PhD thesis. Roskilde, Denmark: Risø National Laboratory, 2000.

[25] HW Bargmann. *Mechanics of composite materials basic equation for fiber reinforced composites.* Tech. rep. 1971.

[26] Stephen W. Tsai and Edward M. Wu. “A General Theory of Strength for Anisotropic Materials”. In: *Journal of Composite Materials* 5.1 (1971), pp. 58–80. DOI: `10.1177/002199837100500106`. eprint: `https://doi.org/10.1177/002199837100500106`. URL: `https://doi.org/10.1177/002199837100500106`.

[27] Khong Wui Gan, Stephen R. Hallett, and Michael R. Wisnom. “Measurement and modelling of interlaminar shear strength enhancement under moderate through-thickness compression”. In: *Composites Part A: Applied Science and Manufacturing* 49 (2013), pp. 18–25. ISSN: 1359-835X. DOI: `https://doi.org/10.1016/j.compositesa.2013.02.004`. URL: `https://www.sciencedirect.com/science/article/pii/S1359835X1300047X`.

[28] P.P. Camanho and M. Lambert. “A design methodology for mechanically fastened joints in laminated composite materials”. In: *Composites Science and Technology* 66.15 (2006), pp. 3004–3020. ISSN: 0266-3538. DOI: `https://doi.org/10.1016/j.compscitech.2006.02.017`. URL: `https://www.sciencedirect.com/science/article/pii/S0266353806000546`.

[29] G. Catalanotti, P.P. Camanho, and A.T. Marques. “Three-dimensional failure criteria for fiber-reinforced laminates”. In: *Composite Structures* 95 (2013), pp. 63–79. ISSN: 0263-8223. DOI: `https://doi.org/10.1016/j.compstruct.2012.07.016`. URL: `https://www.sciencedirect.com/science/article/pii/S0263822312003443`.

[30] H. Koerber, J. Xavier, and P.P. Camanho. “High strain rate characterisation of unidirectional carbon-epoxy IM7-8552 in transverse compression and in-plane shear using digital image correlation”. In: *Mechanics of Materials* 42.11 (2010), pp. 1004–1019. ISSN: 0167-6636. DOI: `https://doi.org/10.1016/j.mechmat.2010.09.003`. URL: `https://www.sciencedirect.com/science/article/pii/S0167663610001262`.

[31] Pedro P. Camanho et al. “Prediction of in situ strengths and matrix cracking in composites under transverse tension and in-plane shear”. In: *Composites Part A: Applied Science and Manufacturing* 37.2 (2006). CompTest 2004, pp. 165–176. ISSN: 1359-835X. DOI: `https://doi.org/10.1016/j.compositesa.2005.04.023`. URL: `https://www.sciencedirect.com/science/article/pii/S1359835X05002526`.

[32] W. J. Macquorn Rankine. “On the Stability of Loose Earth”. In: *Philosophical Transactions of the Royal Society of London* 147 (1857), pp. 9–27. ISSN: 02610523. URL: `http://www.jstor.org/stable/108608` (visited on 07/15/2023).

[33] Renaud Gutkin and Silvestre Pinho. *Review on failure of laminated composites: Experimental perspective and modelling.* Department of Aeronautics, Imperial College London, Feb. 2016.

[34] Rodney Hill. "A theory of the yielding and plastic flow of anisotropic metals". In: *Proceedings of the Royal Society of London. Series A. Mathematical and Physical Sciences* 193.1033 (1948), pp. 281–297.

[35] VD Azzi and Stephen W Tsai. "Anisotropic strength of composites: Investigation aimed at developing a theory applicable to laminated as well as unidirectional composites, employing simple material properties derived from unidirectional specimens alone". In: *Experimental mechanics* 5 (1965), pp. 283–288.

[36] Peter Linde et al. "Modelling and Simulation of Fibre Metal Laminates". In: *ABAQUS Users' Conference* (Jan. 2004).

[37] Zvi Hashin. "Failure Criteria for Unidirectional Fiber Composites". In: *Journal of Applied Mechanics* 47.4 (1980), pp. 329–334.

[38] Chun H. Wang and Cong N. Duong. "Chapter 2 - Failure criteria". In: *Bonded Joints and Repairs to Composite Airframe Structures.* Ed. by Chun H. Wang and Cong N. Duong. Oxford: Academic Press, 2016, pp. 21–45. ISBN: 978-0-12-417153-4. DOI: `https://doi.org/10.1016/B978-0-12-417153-4.00002-5`. URL: `https://www.sciencedirect.com/science/article/pii/B9780124171534000025`.

[39] A. Puck and H. Schürmann. "Failure Analysis of FRP Laminates by means of Physically based Phenomenological Models". In: *Composites Science and Technology* 58.7 (1998), pp. 1045–1067. ISSN: 0266-3538. DOI: `https://doi.org/10.1016/S0266-3538(96)00140-6`. URL: `https://www.sciencedirect.com/science/article/pii/S0266353896001406`.

[40] Sergei Georgievich Lekhnitskii et al. *Theory of elasticity of an anisotropic elastic body.* American Institute of Physics, 1964.

[41] CT Sun and Jianxin Tao. "Prediction of failure envelopes and stress/strain behavior of composite laminates". In: *Failure Criteria in Fibre-Reinforced-Polymer Composites.* Elsevier, 2004, pp. 316–333.

[42] S.R. Swanson, M.J. Messick, and Z. Tian. "Failure of Carbon/Epoxy Lamina Under Combined Stress". In: *Journal of Composite Materials* 21.7 (1987), pp. 619–630. DOI: `10.1177/002199838702100703`. eprint: `https://doi.org/10.1177/002199838702100703`. URL: `https://doi.org/10.1177/002199838702100703`.

[43] L. Kachanov. "Time of the Rupture Process under Creep Conditions". In: *Izvestiia Akademii Nauk SSSR* (1958), pp. 26–31.

[44] Yu. N. Rabotnov, F. A. Leckie, and W. Prager. "Creep Problems in Structural Members". In: *Journal of Applied Mechanics* 37.1 (Mar. 1970), pp. 249–249. ISSN: 0021-8936. DOI: `10.1115/1.3408479`. eprint: `https://asmedigitalcollection.asme.org/appliedmechanics/article-pdf/37/1/249/5450383/249\_2.pdf`. URL: `https://doi.org/10.1115/1.3408479`.

[45] Lasar Kachanov. *Introduction to continuum damage mechanics.* Vol. 10. Springer Science & Business Media, 1986.

[46] Jean Lemaitre. “How to use damage mechanics”. In: *Nuclear Engineering and Design* 80.2 (1984). 4th Special Issue on Smirt-7, pp. 233–245. ISSN: 0029-5493. DOI: `https://doi.org/10.1016/0029-5493(84)90169-9`. URL: `https://www.sciencedirect.com/science/article/pii/0029549384901699`.

[47] Jean Lemaître and Jean Louis Chaboche. “ASPECT PHENOMENOLOGIQUE DE LA RUPTURE PAR ENDOMMAGEMENT”. In: 1978. URL: `https://api.semanticscholar.org/CorpusID:131574321`.

[48] Sumio Murakami. *Continuum Damage Mechanics: A Continuum Mechanics Approach to the Analysis of Damage and Fracture.* Vol. 185. Springer Dordrecht, 2012.

[49] A. Matzenmiller, J. Lubliner, and R.L. Taylor. “A constitutive model for anisotropic damage in fiber-composites”. In: *Mechanics of Materials* 20.2 (1995), pp. 125–152. ISSN: 0167-6636. DOI: `https://doi.org/10.1016/0167-6636(94)00053-0`. URL: `https://www.sciencedirect.com/science/article/pii/0167663694000530`.

[50] Lachaud, Frédéric, Haramburu, Eric, and Jetteur, Philippe. “Modélisation élasto-plastique endommageable des composites”. In: *Mécanique & Industries* 7.4 (2006), pp. 403–414. DOI: `10.1051/meca:2006054`. URL: `https://doi.org/10.1051/meca:2006054`.

[51] Wei Tan and Brian G. Falzon. “Modelling the nonlinear behaviour and fracture process of AS4/PEKK thermoplastic composite under shear loading”. In: *Composites Science and Technology* 126 (2016), pp. 60–77. ISSN: 0266-3538. DOI: `https://doi.org/10.1016/j.compscitech.2016.02.008`. URL: `https://www.sciencedirect.com/science/article/pii/S0266353816300343`.

[52] P. Ladeveze and E. LeDantec. “Damage modelling of the elementary ply for laminated composites”. In: *Composites Science and Technology* 43.3 (1992), pp. 257–267. ISSN: 0266-3538. DOI: `https://doi.org/10.1016/0266-3538(92)90097-M`. URL: `https://www.sciencedirect.com/science/article/pii/026635389290097M`.

[53] Eduardo A de Souza Neto, Djordje Peric, and David RJ Owen. *Computational methods for plasticity: theory and applications.* John Wiley and Sons, 2011.

[54] Fuji Wang et al. “A comparison of cutting mechanisms of the carbon fibre reinforced thermoset and thermoplastic composites by the experimental and computational modelling methods”. In: *Journal of Manufacturing Processes* 79 (2022), pp. 895–910. ISSN: 1526-6125. DOI: `https://doi.org/10.1016/j.jmapro.2022.05.033`. URL: `https://www.sciencedirect.com/science/article/pii/S1526612522003474`.

[55] Andrew Noel Schofield and Peter Wroth. *Critical state soil mechanics.* Vol. 310. McGraw-Hill London, 1968.

[56] Hong T. Hahn and Stephen W. Tsai. “Nonlinear Elastic Behavior of Unidirectional Composite Laminae”. In: *Journal of Composite Materials* 7.1 (1973), pp. 102–118. DOI: `10.1177/002199837300700108`. eprint: `https://doi.org/10.1177/002199837300700108`. URL: `https://doi.org/10.1177/002199837300700108`.

[57] Fu-Kuo Chang, Richard A. Scott, and George S. Springer. “Failure Strength of Nonlinearly Elastic Composite Laminates Containing a Pin Loaded Hole”. In: *Journal of Composite Materials* 18.5 (1984), pp. 464–477. DOI: `10.1177/002199838401800506`. eprint: `https://doi.org/10.1177/002199838401800506`. URL: `https://doi.org/10.1177/002199838401800506`.

[58] P.D. Soden, M.J. Hinton, and A.S. Kaddour. “Lamina properties, lay-up configurations and loading conditions for a range of fibre-reinforced composite laminates”. In: *Composites Science and Technology* 58.7 (1998), pp. 1011–1022. ISSN: 0266-3538. DOI: `https://doi.org/10.1016/S0266-3538(98)00078-5`. URL: `https://www.sciencedirect.com/science/article/pii/S0266353898000785`.

[59] Frédéric Lachaud. “Délaminage de matériaux composites à fibres de carbone et à matrices organiques : étude numérique et expérimentale, suivi par émission acoustique”. PhD thesis. Institut Superieur de l’Aéronautique et de l’Espace, 1997.

[60] P. Maimí et al. “A continuum damage model for composite laminates: Part I – Constitutive model”. In: *Mechanics of Materials* 39.10 (2007), pp. 897–908. ISSN: 0167-6636. DOI: `https://doi.org/10.1016/j.mechmat.2007.03.005`. URL: `https://www.sciencedirect.com/science/article/pii/S0167663607000543`.

[61] ASTM International. *ASTM D 3518/D 3518M: Standard Test Method for In-Plane Shear Response of Polymer Matrix Composite Materials by Tensile Test of a ±45° Laminate.* 2001.

[62] M A Crisfield. “Nonlinear finite element analysis of solids and structures. Volume 1: Essentials”. In: (Dec. 1991). URL: `https://www.osti.gov/biblio/226942`.

[63] Michael R. Wisnom. “The effect of fibre rotation in ±45° tension tests on measured shear properties”. In: *Composites* 26.1 (1995), pp. 25–32. ISSN: 0010-4361. DOI: `https://doi.org/10.1016/0010-4361(94)P3626-C`. URL: `https://www.sciencedirect.com/science/article/pii/0010436194P3626C`.

[64] Sotiris Kellas, John Morton, and Karen E Jackson. “Damage and failure mechanisms in scaled angle-ply laminates”. In: *Composite materials: Fatigue and fracture.* 4 (1993), pp. 257–280.

[65] Carl T. Herakovich et al. “Damage evolution in [±45]s laminates with fiber rotation”. In: *Composites Science and Technology* 60.15 (2000), pp. 2781–2789. ISSN: 0266-3538. DOI: `https://doi.org/10.1016/S0266-3538(00)00091-9`. URL: `https://www.sciencedirect.com/science/article/pii/S0266353800000919`.

[66] J.D. Fuller and M.R. Wisnom. "Pseudo-ductility and damage suppression in thin ply CFRP angle-ply laminates". In: *Composites Part A: Applied Science and Manufacturing* 69 (2015), pp. 64–71. ISSN: 1359-835X. DOI: `https://doi.org/10.1016/j.compositesa.2014.11.004`. URL: `https://www.sciencedirect.com/science/article/pii/S1359835X1400342X`.

[67] Sina Eskandari et al. "Intralaminar damage in polymer composites in the presence of finite fiber rotation: Part I – Constitutive model". In: *Composite Structures* 151 (2016). Smart composites and composite structures In honour of the 70th anniversary of Professor Carlos Alberto Mota Soares, pp. 114–126. ISSN: 0263-8223. DOI: `https://doi.org/10.1016/j.compstruct.2016.01.047`. URL: `https://www.sciencedirect.com/science/article/pii/S026382231600060X`.

[68] Cheng Chen. "Contribution à la prise en compte des effets de l'environnement sur la tolérance aux dommages d'impact de stratifiés composites". 2015ESAE0004. PhD thesis. Institut Superieur de l'Aéronautique et de l'Espace, 2015. URL: `http://www.theses.fr/2015ESAE0004/document`.

[69] Carlos G. Davila, Pedro P. Camanho, and Cheryl A. Rose. "Failure Criteria for FRP Laminates". In: *Journal of Composite Materials* 39.4 (2005), pp. 323–345. DOI: `10.1177/0021998305046452`. eprint: `https://doi.org/10.1177/0021998305046452`. URL: `https://doi.org/10.1177/0021998305046452`.

[70] Jean-Pierre Dedieu. "Newton-Raphson Method". In: *Encyclopedia of Applied and Computational Mathematics*. Ed. by Björn Engquist. Berlin, Heidelberg: Springer Berlin Heidelberg, 2015, pp. 1023–1028. ISBN: 978-3-540-70529-1. DOI: `10.1007/978-3-540-70529-1_374`. URL: `https://doi.org/10.1007/978-3-540-70529-1_374`.

[71] A. Parvizi, K. W. Garrett, and J. E. Bailey. "Constrained cracking in glass fibre-reinforced epoxy cross-ply laminates". In: *Journal of Materials Science* 13 (Jan. 1978). DOI: `10.1007/BF00739291`.

[72] ST Pinho et al. "Material and structural response of polymer-matrix fibre-reinforced composites". In: *Journal of Composite Materials* 46.19-20 (2012), pp. 2313–2341. DOI: `10.1177/0021998312454478`. eprint: `https://doi.org/10.1177/0021998312454478`. URL: `https://doi.org/10.1177/0021998312454478`.

[73] George J. Dvorak and Norman Laws. "Analysis of Progressive Matrix Cracking In Composite Laminates II. First Ply Failure". In: *Journal of Composite Materials* 21.4 (1987), pp. 309–329. DOI: `10.1177/002199838702100402`. eprint: `https://doi.org/10.1177/002199838702100402`. URL: `https://doi.org/10.1177/002199838702100402`.

[74] N. Laws. "A note on interaction energies associated with cracks in anisotropic solids". In: *The Philosophical Magazine: A Journal of Theoretical Experimental and Applied Physics* 36.2 (1977), pp. 367–372. DOI: `10.1080/14786437708244940`. eprint: `https://doi.org/10.1080/14786437708244940`. URL: `https://doi.org/10.1080/14786437708244940`.

[75] Zdenek Bazant and Byung Oh. "Crack Band Theory for Fracture of Concrete". In: *Matériaux et Constructions* 16 (May 1983), pp. 155–177. DOI: `10.1007/BF02486267`.

[76] P. Maimí et al. "A continuum damage model for composite laminates: Part II – Computational implementation and validation". In: *Mechanics of Materials* 39.10 (2007), pp. 909–919. ISSN: 0167-6636. DOI: `https://doi.org/10.1016/j.mechmat.2007.03.006`. URL: `https://www.sciencedirect.com/science/article/pii/S0167663607000555`.

[77] L.A. Carlsson and R.B. Pipes. *Experimental Characterization of Advanced Composite Materials*. Prentice-Hall, 1987. ISBN: 9780132949507. URL: `https://books.google.pt/books?id=X8FRAAAAMAAJ`.

[78] George J. Dvorak, Norman Laws, and Mehdi Hejazi. "Analysis of Progressive Matrix Cracking in Composite Laminates I. Thermoelastic Properties of a Ply with Cracks". In: *Journal of Composite Materials* 19.3 (1985), pp. 216–234. DOI: `10.1177/002199838501900302`. eprint: `https://doi.org/10.1177/002199838501900302`. URL: `https://doi.org/10.1177/002199838501900302`.

[79] N. Laws, G.J. Dvorak, and M. Hejazi. "Stiffness changes in unidirectional composites caused by crack systems". In: *Mechanics of Materials* 2.2 (1983), pp. 123–137. ISSN: 0167-6636. DOI: `https://doi.org/10.1016/0167-6636(83)90032-7`. URL: `https://www.sciencedirect.com/science/article/pii/0167663683900327`.

[80] R.J. Nuismer and S.C. Tan. "Constitutive Relations of a Cracked Composite Lamina". In: *Journal of Composite Materials* 22.4 (1988), pp. 306–321. DOI: `10.1177/002199838802200401`. eprint: `https://doi.org/10.1177/002199838802200401`. URL: `https://doi.org/10.1177/002199838802200401`.

[81] S.C. Tan and R.J. Nuismer. "A Theory for Progressive Matrix Cracking in Composite Laminates". In: *Journal of Composite Materials* 23.10 (1989), pp. 1029–1047. DOI: `10.1177/002199838902301006`. eprint: `https://doi.org/10.1177/002199838902301006`. URL: `https://doi.org/10.1177/002199838902301006`.

[82] Enio Silva et al. "Accelerated Aging on the Compression Properties of a Green Polyurethane Foam: Experimental and Numerical Analysis". In: *Polymers* 15 (Apr. 2023), p. 1784. DOI: `10.3390/polym15071784`.

[83] R. D. Krieg and D. B. Krieg. "Accuracies of Numerical Solution Methods for the Elastic-Perfectly Plastic Model". In: *Journal of Pressure Vessel Technology* 99.4 (Nov. 1977), pp. 510–515. ISSN: 0094-9930. DOI: `10.1115/1.3454568`. eprint: `https://asmedigitalcollection.asme.org/pressurevesseltech/article-pdf/99/4/510/5689466/510\_1.pdf`. URL: `https://doi.org/10.1115/1.3454568`.

[84] Jinsong Huang and DV Griffiths. "Return mapping algorithms and stress predictors for failure analysis in geomechanics". In: *Journal of Engineering Mechanics* 135.4 (2009), pp. 276–284.

[85] J.C. Simo and M. Ortiz. "A unified approach to finite deformation elastoplastic analysis based on the use of hyperelastic constitutive equations". In: *Computer Methods in Applied Mechanics and Engineering* 49.2 (1985), pp. 221–245. ISSN: 0045-7825. DOI: `https://doi.org/10.1016/0045-7825(85)90061-1`. URL: `https://www.sciencedirect.com/science/article/pii/0045782585900611`.

[86] M. R. T. Arruda, M. Trombini, and A. Pagani. "Implicit to Explicit Algorithm for ABAQUS Standard User-Subroutine UMAT for a 3D Hashin-Based Orthotropic Damage Model". In: *Applied Sciences* 13.2 (2023). ISSN: 2076-3417. DOI: `10.3390/app13021155`. URL: `https://www.mdpi.com/2076-3417/13/2/1155`.

[87] Michael Smith. *ABAQUS/Standard User's Manual, Version 6.9.* English. United States: Dassault Systèmes Simulia Corp, 2009.

[88] Haibao Liu et al. "A three-dimensional elastic-plastic damage model for predicting the impact behaviour of fibre-reinforced polymer-matrix composites". In: *Composites Part B: Engineering* 201 (2020), p. 108389. ISSN: 1359-8368. DOI: `https://doi.org/10.1016/j.compositesb.2020.108389`. URL: `https://www.sciencedirect.com/science/article/pii/S1359836820334375`.

[89] ASTM International. *ASTM D 3039/D 3039M: Standard Test Method for Tensile Properties of Polymer Matrix Composite Materials.* 2002.

[90] Gina Gohorianu. "Interactions entre les défauts d'usinage et la tenue en matage d'assemblages boulonnés en carbone/epoxy". 2008TOU30046. PhD thesis. Institut Superieur de l'Aéronautique et de l'Espace, 2008, 1 vol. (200 p.) URL: `http://www.theses.fr/2008TOU30046/document`.

[91] ASTM International. *ASTM D3410/D3410M-16e1: Standard Test Method for Compressive Properties of Polymer Matrix Composite Materials with Unsupported Gage Section by Shear Loading.* 2021.

Appendix A

Proposed Experimental Testing Campaign

Given the purpose of establishing the intra-ply, inter-ply and impact behaviour of the composite, an assortment of tests is proposed. Five iterations of each should be carried out in order to achieve statistical significance of the acquired data.

For intra-ply properties and behaviour, the tests displayed in Table A.1 should be implemented. These allow for the characterization of the material's fundamental properties in longitudinal, transverse and in-plane shear directions, as well as its fracture related properties, both in tension and compression.

Table A.1: Tests for characterisation and identification of damage, plasticity and failure.

Type of test	**Properties**	**Layup**	**Nr. of tests**
Longitudinal tensile	X_T, ϵ_{11}^R, E_{11}	$[0]_8$	5
Transverse tensile	Y_T, ϵ_{22}^R, E_{22}	$[90]_{16}$	5
In-plane shear	S_L, ϵ_{12}^R, G_{12}	$[\pm 45]_{2S}$	5
Coupled tensile	Coupling coefficient	$[\pm 60]_{2S}$	5
Longitudinal compressive	X_C, ϵ_{11}^R, E_{11}^c	$[0]_{34}$	5
Transverse compressive	Y_C, ϵ_{22}^R, E_{22}	$[90]_{34}$	5
Compact tension	G_c^T	$[(0/90)_5]_S$	5
Compact compression	G_c^C	$[(0/90)_5]_S$	5

Regarding the inter-ply behaviour, double cantilever beam (DCB) and end notch flexure (ENF) tests should be done to characterize the interface fracture energy in mode I and II, respectively. Interlaminar shear strength (ILSS) and L-shape tests are used for evaluating the out-of-plane properties, allowing for a three dimensional representation of the laminate.

Table A.2: Tests for characterization of delamination and out-of-plane behaviour.

Type of test	Properties	Layup	Nr. of tests
DCB	G_I	$[0]_{16}$	5
ENF	G_{II}	$[0]_{16}$	5
ILSS	σ_{13}^R	$[0]_{16}$	5
L Shape	σ_{33}^R	$[0]_{22}$	5

A.1 Procedure

This section describes proposed procedures for the longitudinal, transverse and in-plane shear tensile tests, describing as well the equipment used for that purpose.

A.1.1 Testing Systems

Intra-ply and inter-ply tests are done with the aid of servo-hydraulic Instron universal testing machines - 5900R 5969 and 4200 4206 - with a load capacity of 50 and 100 kN, respectively, maximum stroke of 100 mm and frame stiffness of 595 kN/mm. Their actuator speed can vary between 1 μm/hr and 300 mm/min, providing a suitable range of velocities in which to perform the necessary quasi-static characterization of the composite.

Force and displacement data is measured by the machine and strains are obtained through a non-contacting video extensometer, Instron AVE 2 Non-Contacting Video Extensometer, with 490 Hz data rate which tracks four points in the surface of the specimen, outputting the longitudinal and transverse strains. Data treatment and analysis is then carried with the Bluehill 3 software.

A.1.2 Ply Characterization

The first stage of material characterization consists of obtaining the intralaminar properties through the tests highlighted in Table A.1.

A.1.2.1 Longitudinal Tensile

This test is performed along the fiber direction, allowing for the characterization of the properties of the composite across this dimension. These are the longitudinal tensile stiffness modulus E_{11}^t, the ultimate tensile strength X_T and strain ϵ_{11}^t, as well as the Poisson ratio ν_{12}.

In order to take into consideration external factors that may influence the tensile behaviour of the specimen and in agreement with the recommendations of the standard test method ASTM D3039 [89], the following characteristics should be measured at the time of testing.

1. Material preparation
2. Layup

3. Specimen preparation
4. Specimen conditioning
5. Testing environment
6. Specimen alignment and gripping
7. Testing speed
8. Temperature
9. Void content
10. Fiber volume

Test Procedure: A set of guidelines are proposed to ensure proper data gathering.

- Calibrate the AVE 2 video extensometer through the calibration bar. The distance between two neighboring horizontal or vertical points should be $6 \pm 0.005[mm]$.
- Measure the specimen's width and thickness.
- Paint four dots in the specimen, two aligned with the longitudinal axis and two with the transversal axis. Experience with a GFRP specimen suggests that a 5 mm white dot with a 3 mm black dot inside of it might be the best strategy. However, given that the color & light interaction properties of CFRP are vastly different, a single 3 to 5 mm white dot should be the best option, as designated by the manufacturer in the User's Manual. Note: the AVE2 uses polarized light.
- Verify the alignment of the specimen with the machine axis.
- Input the width, thickness of the specimen, longitudinal and transversal distance between the marked points, pre-stress, test velocity, maximum displacement, maximum F, maximum ΔF [%] between two consecutive measurements.
- Zero the machine – displacement.
- Register the ambient temperature.
- Begin the test.
- After failure / ending – save the data and export to an Excel data sheet for post-treatment.

A.1.2.2 Transverse Tensile

Performing a tensile test in a layup of $[90]_{16}$ is useful for determining the transverse behaviour and properties of the composite. The transverse tensile stiffness modulus E_{22}^t, ultimate transverse strength Y_T and strain ϵ_{22}^t can all be obtained through this procedure.

In a similar way to the longitudinal tensile test, ambient conditions and material characteristics should also registered at the time of the test.

A.1.2.3 In-plane Shear

This test allows for the characterization of the composite in the plane shear configuration, providing the shear modulus G_{12} and both the ultimate shear strength S_L and strain ϵ_{12}^s

The standard ASTM D3518/D3518M [61] suggests that data reporting should terminate at 0.05ϵ due to fiber scissoring effects hindering the reliability of the data gathered after those values of engineering strain. This value amounts to approximately 1.5 degrees, after which, the conditions sustained by the specimen differ significantly to those of pure shear. Hence, the shear modulus should be defined in the interval of 2000 to 6000$\mu\epsilon$ or, alternatively, 500$\mu\epsilon$ below the upper limit of the material's linear region.

The shear strain-stress response is obtained by converting the global tensile stress into the local shear stress, through the plane stress transformation relation where:

$$\tau_{12} = -\frac{\sigma_x - \sigma_y}{2} sin2\theta + \tau_{xy} cos2\theta \tag{A.1}$$

Given that the laminate is composed of a [±45] layup and that there is no applied stress in the transverse direction, the only non-null component is σ_x, which is equal to the average applied tensile stress. Hence:

$$\tau_{12} = \frac{\sigma_x}{2} \tag{A.2}$$

As for the shear strain, it is obtained from the axial and transverse strains measured by the strain gauges, through the following relation:

$$\gamma_{12} = \epsilon_x - \epsilon_y \tag{A.3}$$

Appendix B

Technical Drawings of the Test Plates

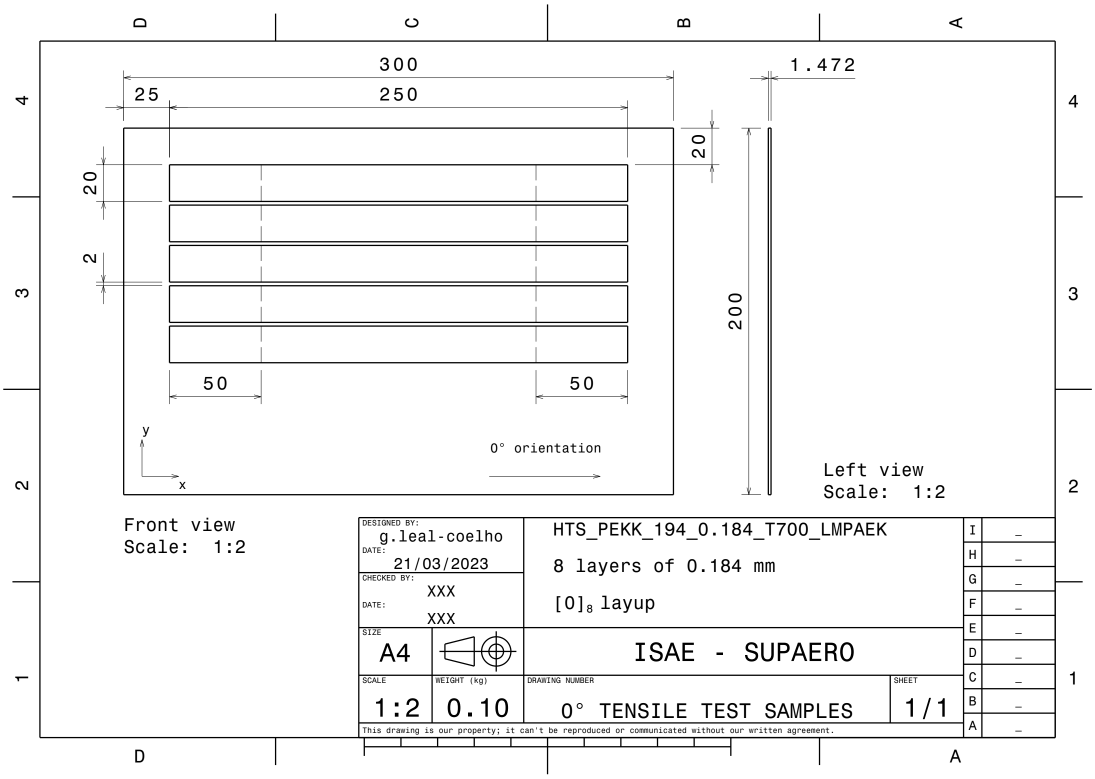

Figure B.1: Longitudinal tensile test plate.

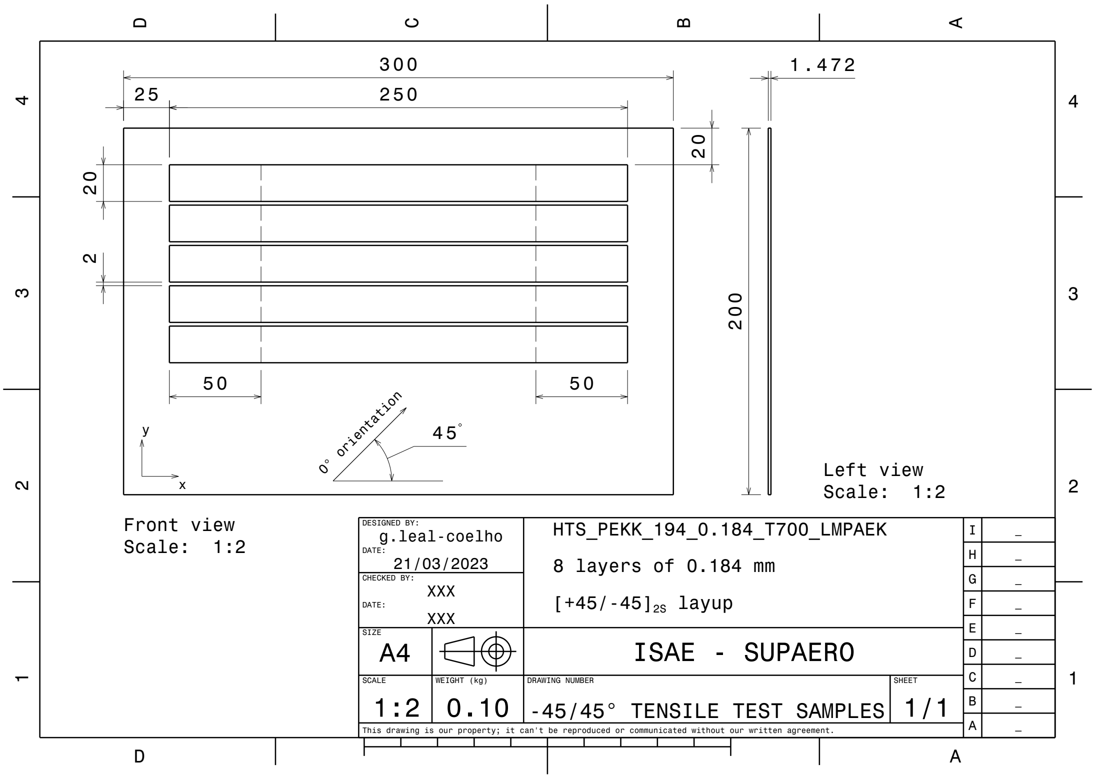

Figure B.2: In-plane shear tensile test plate.

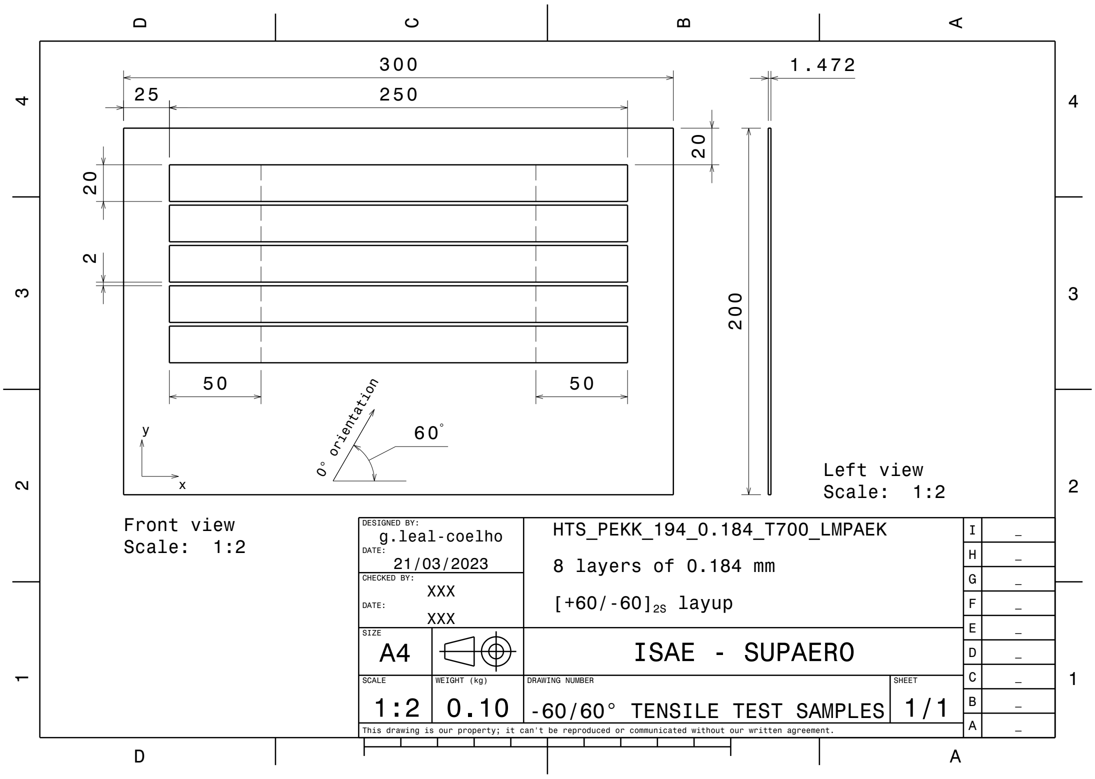

Figure B.3: Coupled tensile test plate.

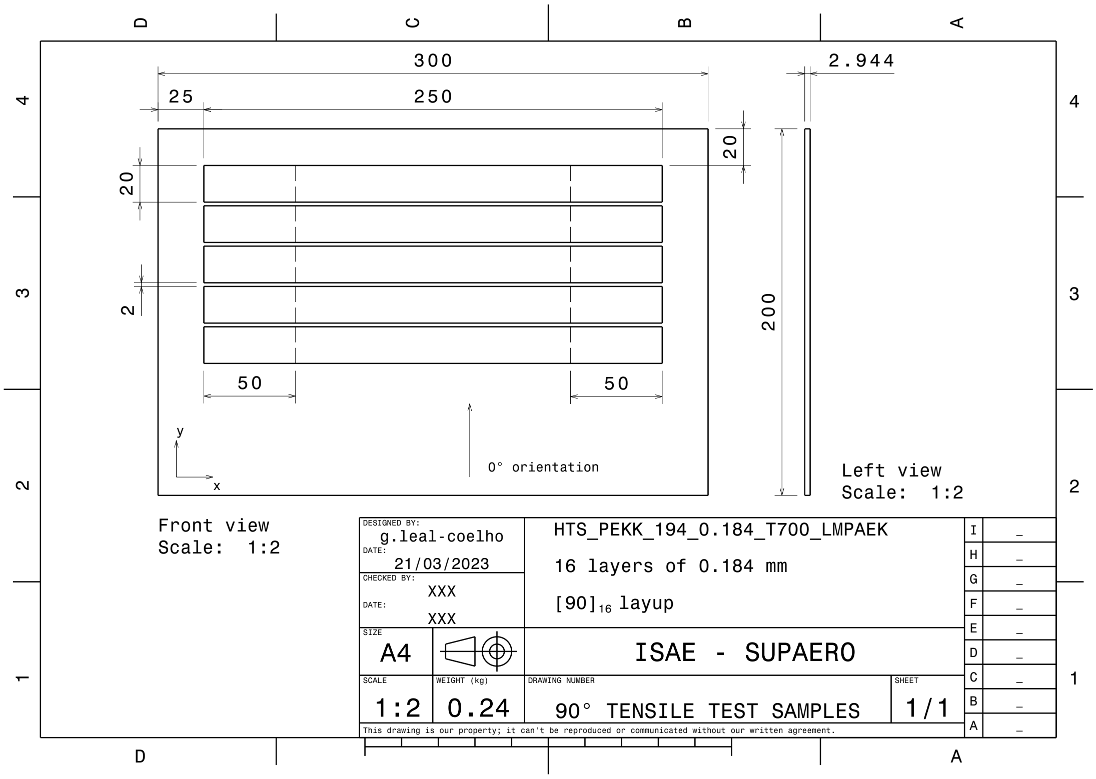

Figure B.4: Transverse tensile test plate.

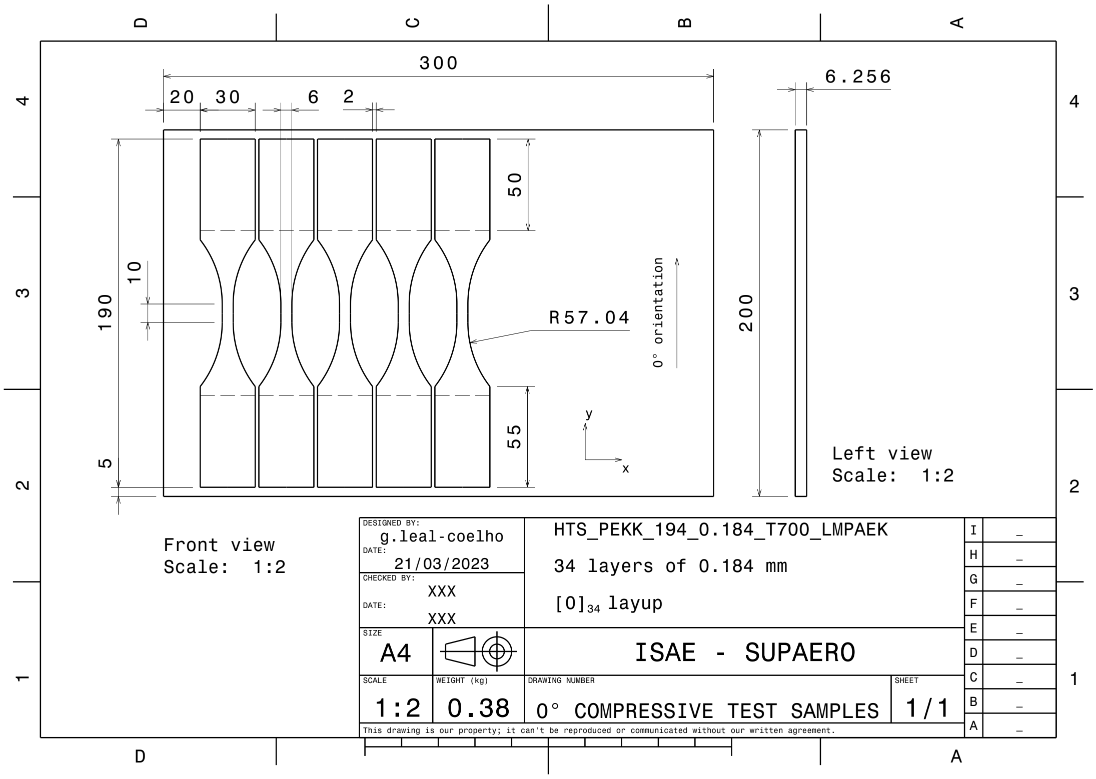

Figure B.5: Longitudinal compressive test plate.

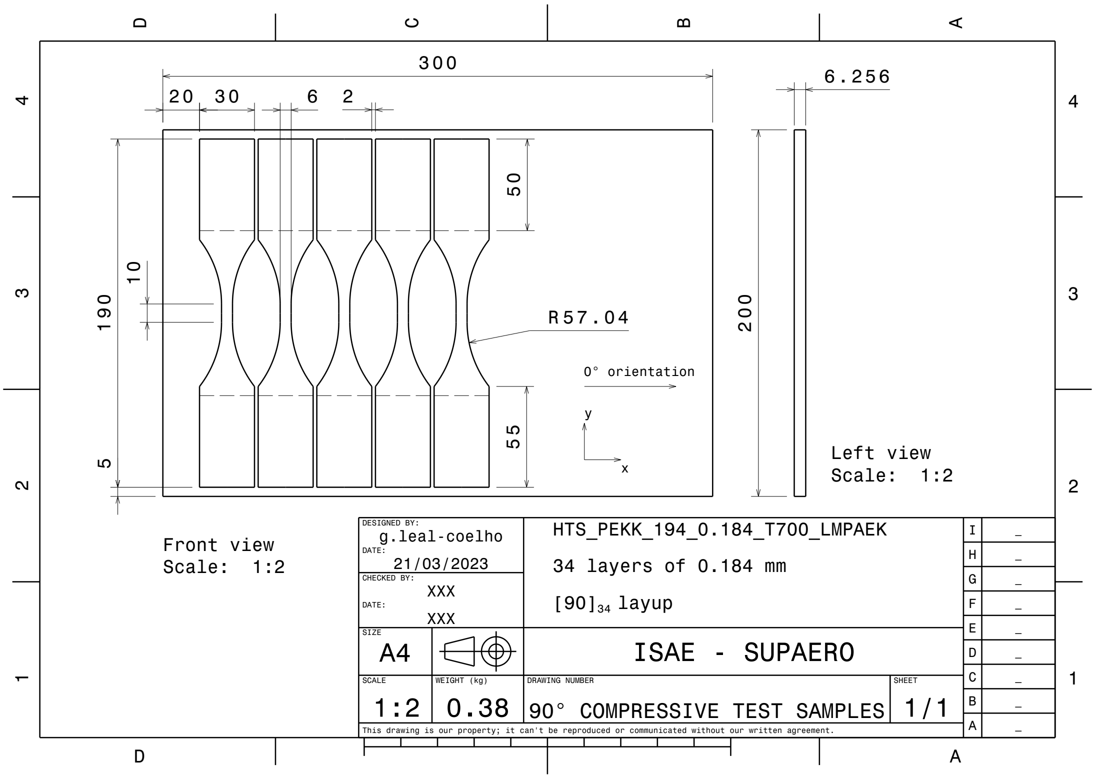

Figure B.6: Transverse compressive test plate.

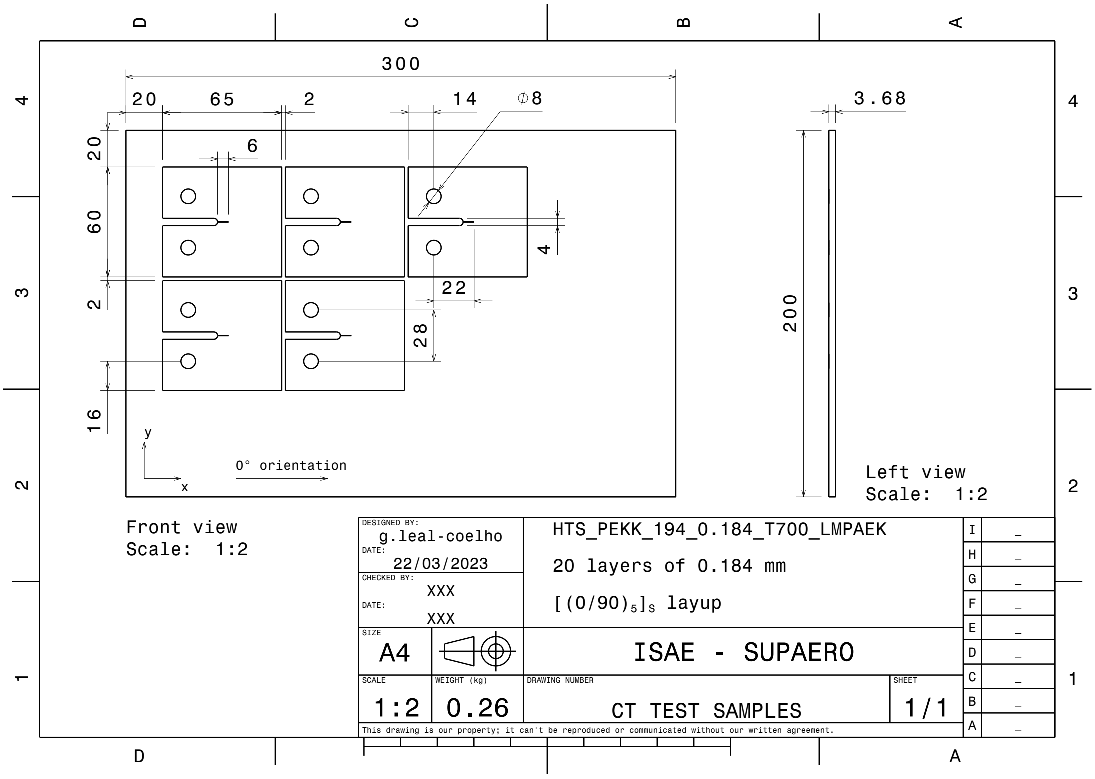

Figure B.7: Compact tension test plate.

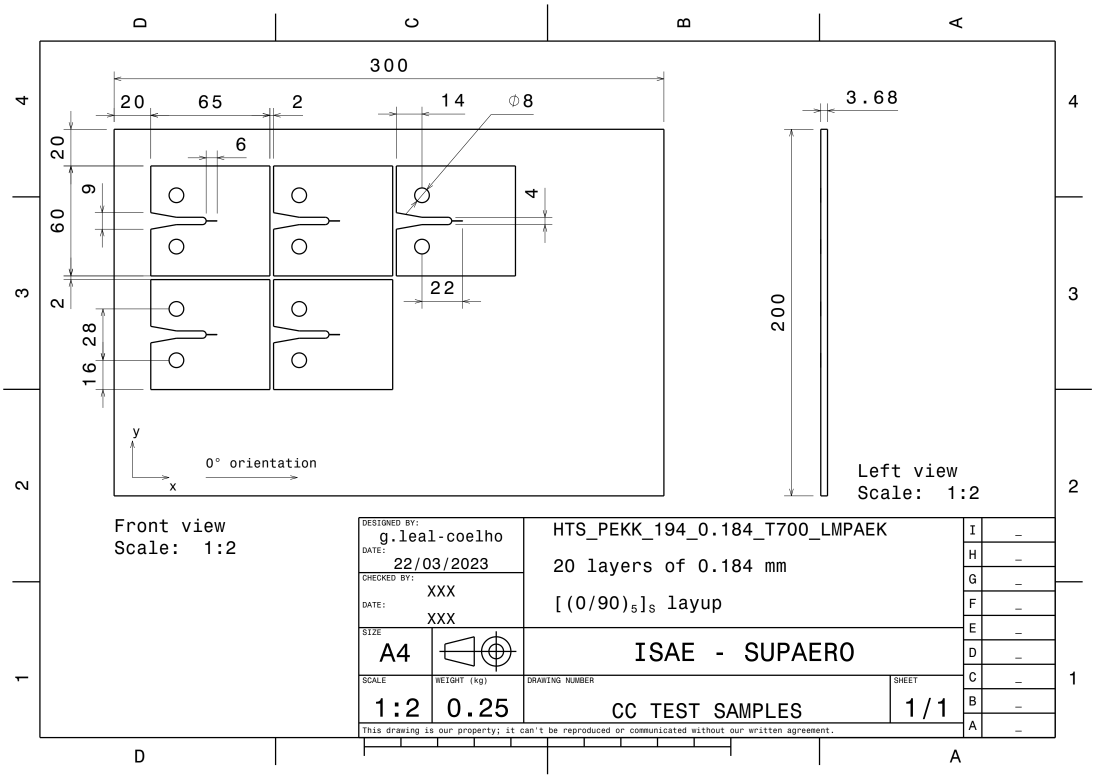

Figure B.8: Compact compression test plate.

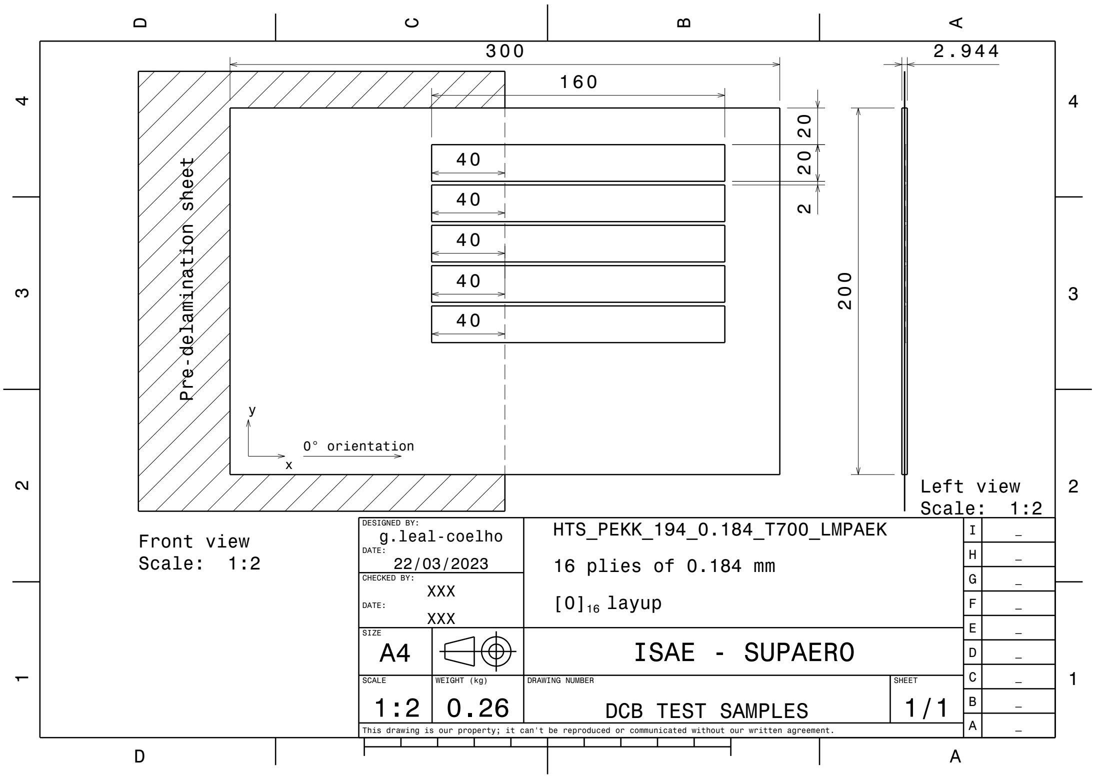

Figure B.9: Double cantilever beam test plate.

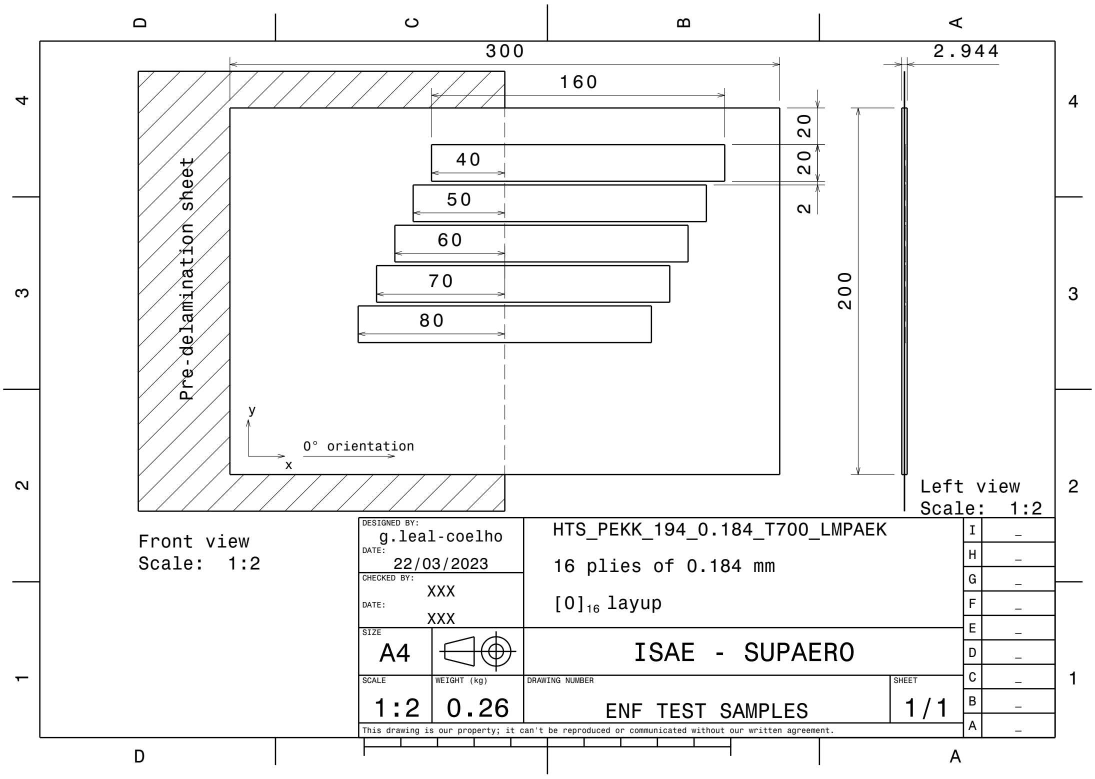

Figure B.10: End notch flexure test plate.

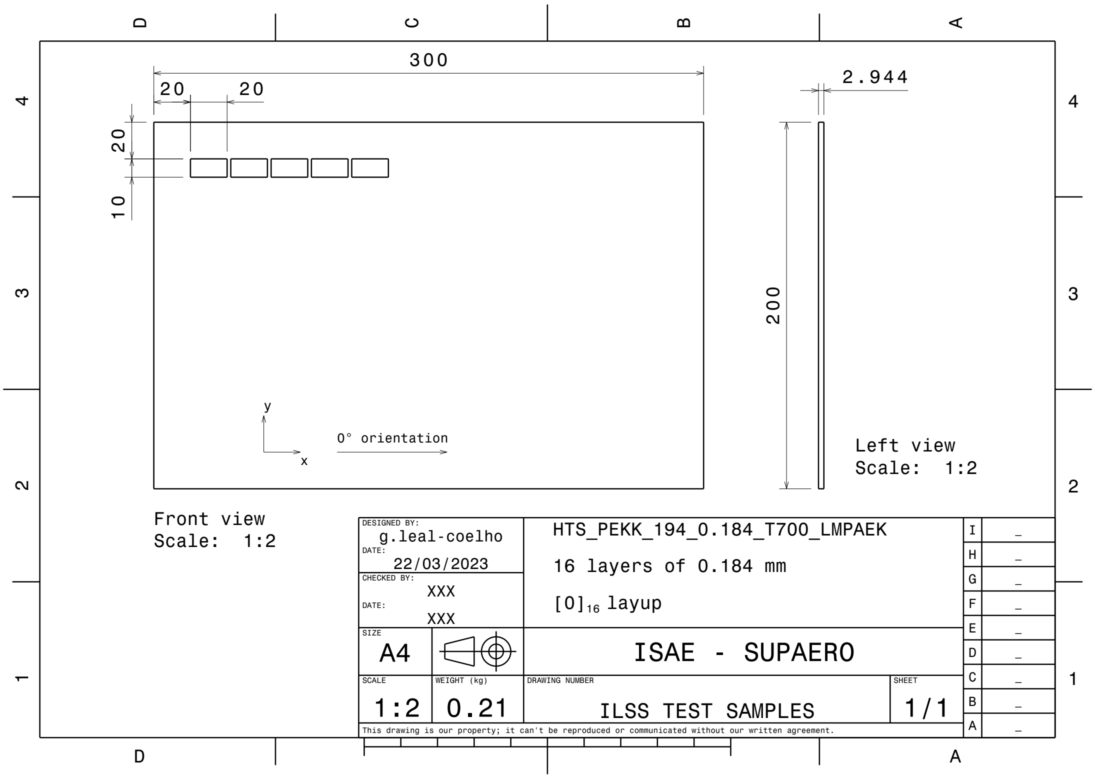

Figure B.11: Interlaminar shear strength test plate.

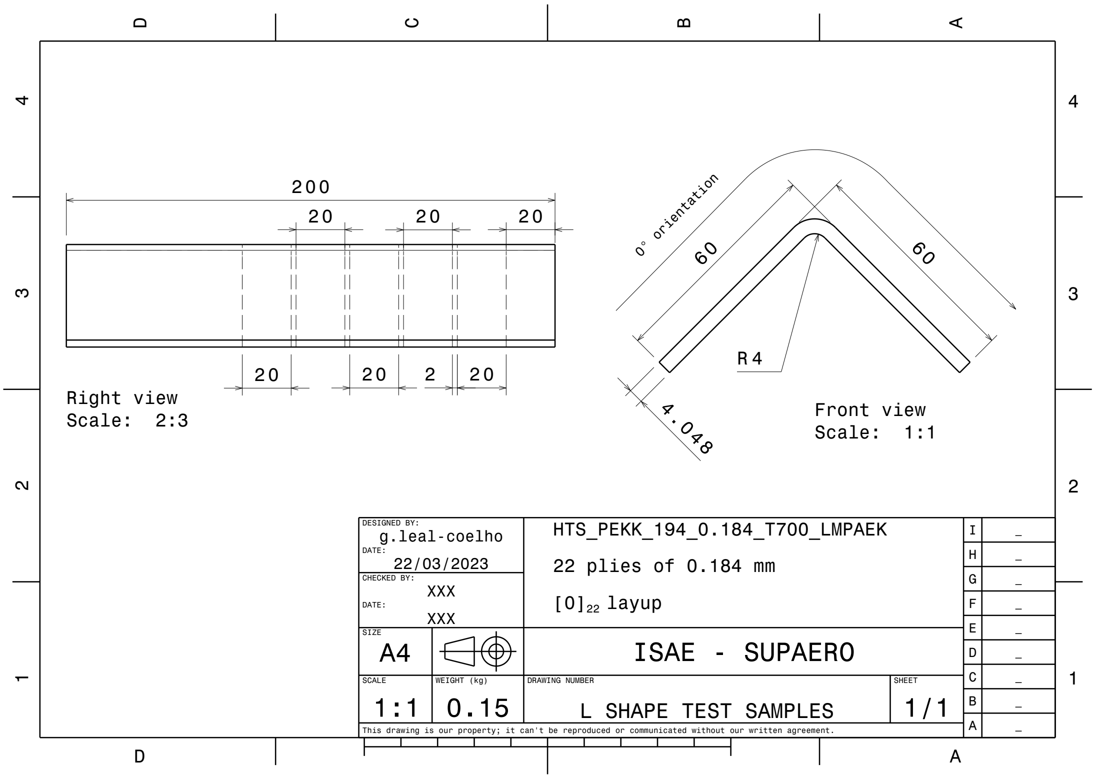

Figure B.12: L-shape tensile test plate.

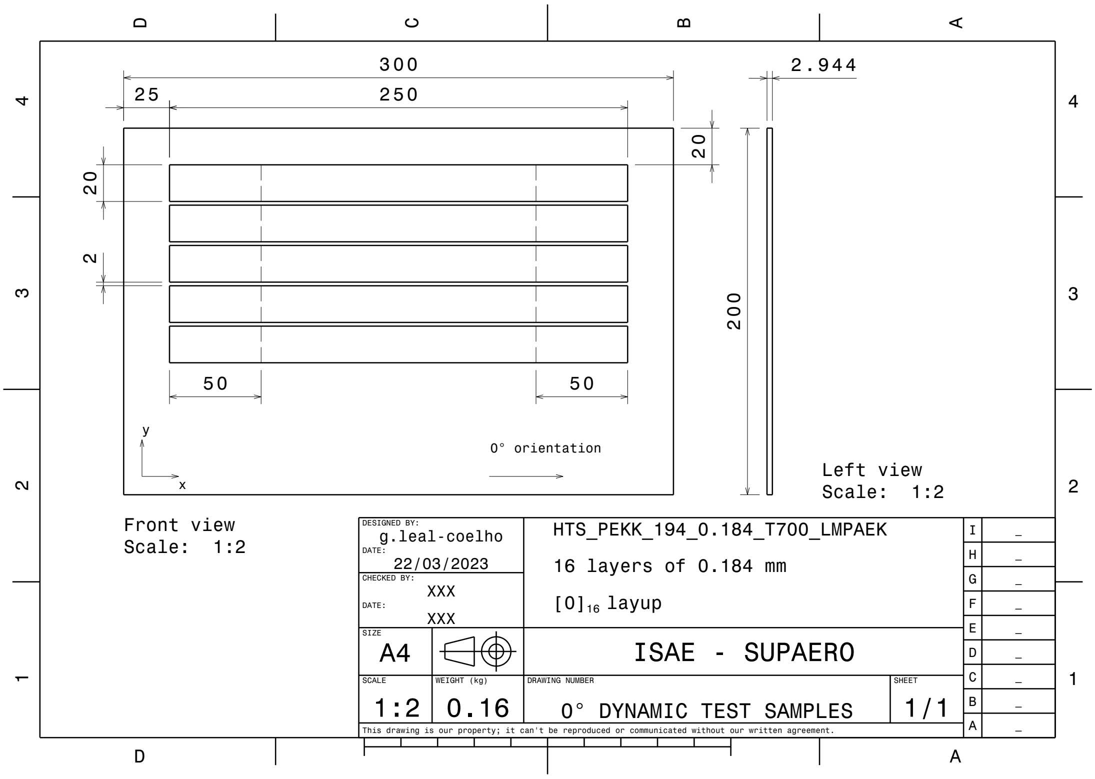

Figure B.13: Dynamic longitudinal tensile test plate.

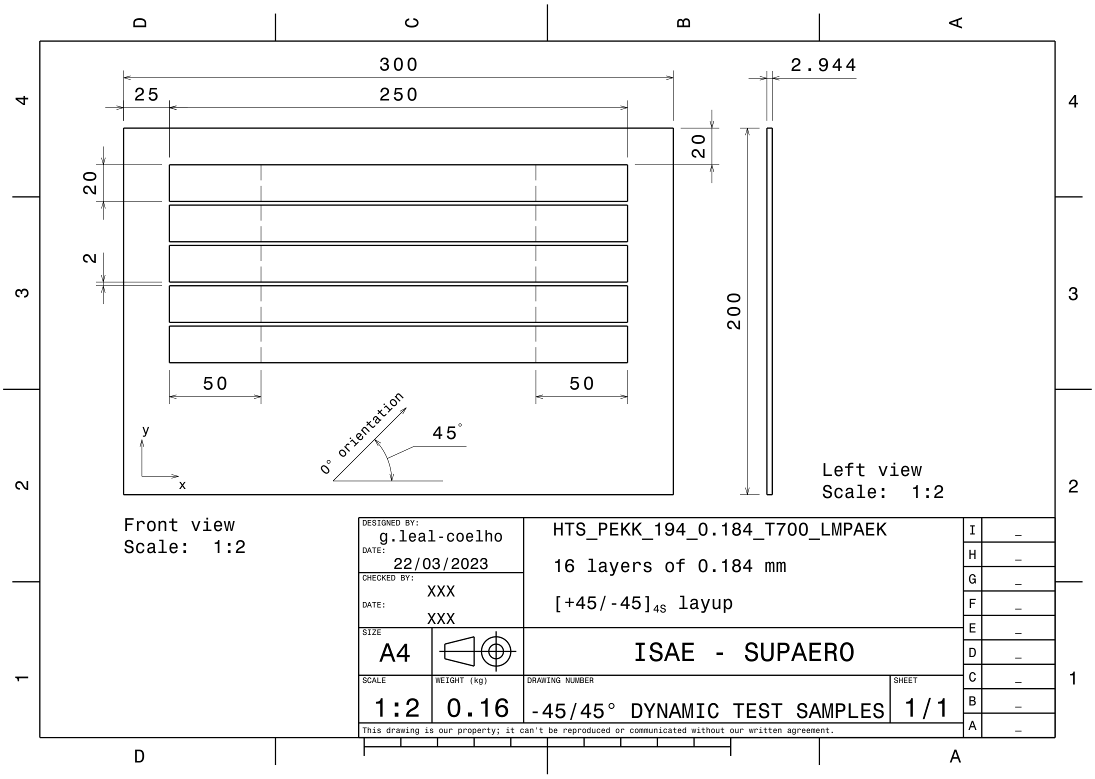

Figure B.14: Dynamic in-plane shear tensile test plate.

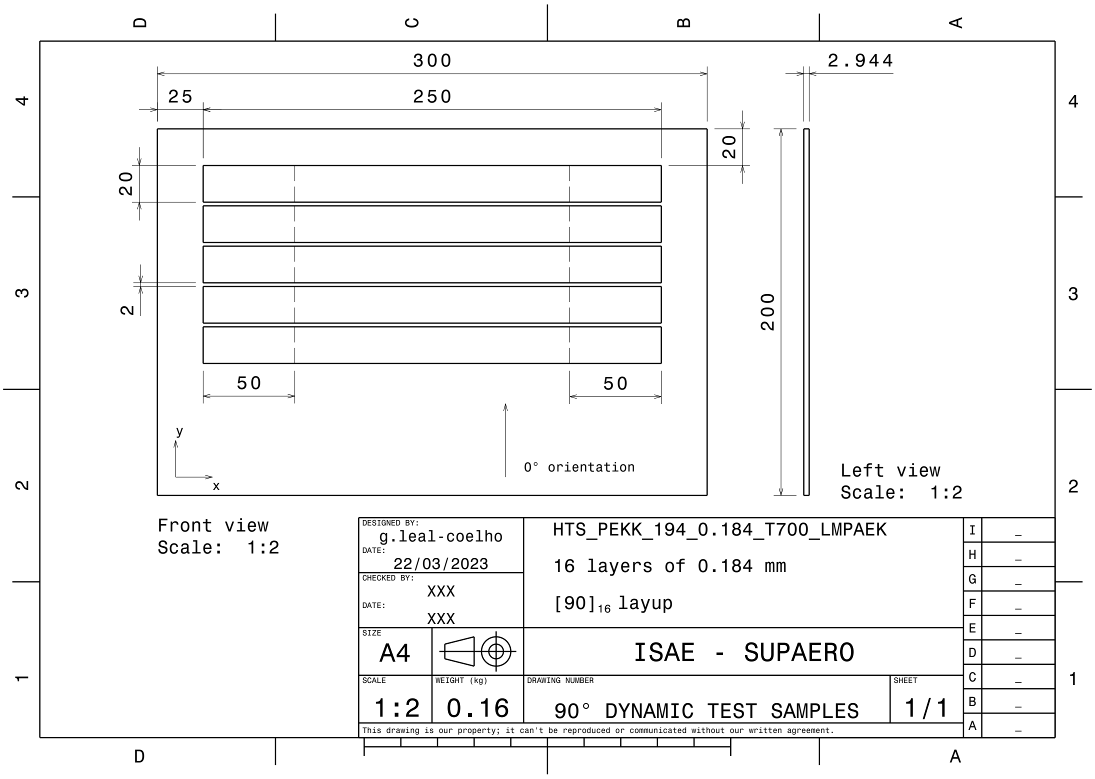

Figure B.15: Dynamic transverse tensile test plate.